QUANTITATIVE OPTICAL IMAGING OF SINGLE-WALLED CARBON NANOTUBES

A Dissertation

Presented to the Faculty of the Graduate School

of Cornell University

in Partial Fulfillment of the Requirements for the Degree of

Doctor of Philosophy

by

Lihong H. Herman

May 2013

QUANTITATIVE OPTICAL IMAGING OF SINGLE-WALLED CARBON NANOTUBES

Lihong H. Herman, Ph.D.

Cornell University 2013

The development and application of optical imaging tools and probing techniques have been the subject of exciting research. These tools and techniques allow for non-invasive, simple sample preparation and relatively fast measurement of electronic and optical properties. They also provided crucial information on optoelectronic device application and development. As the field of nanostructure research emerged, they were modified and employed to understand various properties of these structures at the diffraction limit of light. Carbon nanotubes, up to hundreds of micrometers long and several nanometers thin, are perfect for testing and demonstrating newly-developed optical measurement platforms for individual nanostructures, due to their heterogeneous nature.

By employing two quantitative imaging techniques, wide-field on-chip Rayleigh scattering spectroscopy and spatial modulation confocal absorption microscopy, we investigate the optical properties of single-walled carbon nanotubes. These techniques allow us to obtain the Rayleigh scattering intensity, absolute absorption cross section, spatial resolution, and spectral information of single-walled carbon nanotubes. By probing the optical resonance of hundreds of single-walled carbon nanotubes in a single measurement, the first technique utilizes Rayleigh scattering mechanism to obtain the chirality of carbon nanotubes. The second technique, by using high numerical aperture oil immersion

objective lenses, we measure the absolute absorption cross section of a single-walled carbon nanotube. Combining all the quantitative values obtained from these techniques, we observe various interesting and recently discovered physical behaviors, such as long range optical coupling and universal optical conductivity on resonance, and demonstrate the possibility of accurate quantitative absorption measurement for individual structures at nanometer scale.

BIOGRAPHICAL SKETCH

Lihong Herman was born in Guangdong, a southern province of mainland China. Both parents, the "lost generation", were not able to finish middle school, due to the Down-to-the-Countryside Movement directed by Mao in the late 1960s. Growing up as the only child in the family, Lihong expressed great curiosity towards everything he encountered. His parents could only satisfy Lihong's thirst for knowledge by bringing him to the local library to browse the encyclopedias. In his hometown, he witnessed the economic reform of China and the transformation of farmlands into metropolitan buildings. In a middle school where many students became involved in gang activity, Lihong was fortunate to have a teacher mentor him in science and nature studies. This sparked his interest in a lifelong pursuit of understanding science. After high school, he followed his mother to immigrate to United States. After immigration, he worked in various places to get on his feet. He was hired for entry level positions at several restaurants, a motel, an appliance repair store, and finally at a local high school as a math and science tutor. During these years, he learned English, realized the importance of higher education, and started planning to pursue a degree. Thanks to California's community college system, at age 22, Lihong attended the University of California, Berkeley to obtain his bachelor degree in mathematics and physics, and became the first member in his family to graduate from college. In 2006, he arrived in Ithaca, NY to pursue a Ph.D. in applied physics at Cornell University. While in Ithaca, he learned community farming, practiced mindfulness meditation, and volunteered as a canine walker at the local SPCA.

To my parents for giving me a childhood without any pressure to be an overachiever.

To all of my friends for trusting, teaching, and helping me.

To my wife for endlessly consulting, supporting, and challenging me (and correcting my grammar).

To my families for believing in me.

ACKNOWLEDGEMENTS

First, I would like to thank my adviser Jiwoong Park for supporting and guiding me over the years at Cornell. Without him, this thesis would not exist. I also want to express my gratitude to him for the advanced and fancy instruments that he worked hard to obtain, so I could perform experiments without worrying about where to find instruments.

Second, I would like to thank the current and formal Park group members. It was wonderful to know all of you over the years. Sang-Yong, thank you for teaching me and giving me guidance; Dan, thank you for being there for the ups and downs; Mike, thank you for sharing the pain of fabrication; Wei, Mark, Carlos, Robin, Lola, Matt, Cheol-Joo, Fai, Zenghui, Chibeom, Professor Miyata, and Professor Choi, thank you for the inspiring discussion over carbon materials, sample fabrication, experimental measurement and science; also Michal, Samuel, Shivank, Nate and Yoon Ji, thank you for assisting me.

Third, I would like to thank my friends and family. My wife, Alexis, thank you for reading this thesis and correcting my grammar; Shriram, thank you for giving me the chance to collaborate with you and get to know you; Jesse, thank you for your time in discussing nanotubes; Praveen, Sam, Sami, Xiao, Eugen, Josh, Simon and Yang, thank you for being my friends and being there for me.

Lastly, I would like to thank all of the people whom I met and known. Without you, I would not be able to become who I am now.

TABLE OF CONTENTS

LIST OF FIGURES

CHAPTER 1

INTRODUCTION

1.1 Background and Motivation

For the past several decades, low-dimensional carbon materials (nanostructures) have been explored in depth, because their properties can be tailored by controlling their size and shape on the nanometer scale. The size of these structures determines their crystal boundary conditions [1], which leads to distinguishable electron density of states of 2-D, 1-D, and even 0-D point-like low-dimensional structures, corresponding to unusual observable physical features of electronic, optical, mechanical, and thermal properties. From a fundamental point of view, the discovery and study of these structures provide new frontiers to stimulate scientific studies which yield exciting discoveries, such as the integer and fractional quantum hall effect for electron systems in 2-D thin films [2–7], Luttinger liquid model for confined electrons in 1-D linear structure [8, 9], and point-like material fullerene in 0-D [10]. From an application point of view, the properties of these structures not only provide the means to pushing the limit of Moore's law to improve the speed and performance of various microelectronic and optoelectronic devices, but also make probing and interrogating mechanisms possible for biological and chemical studies ranging from cells to individual molecules [11].

Since their discovery in 1991 [12], carbon nanotubes have transformed ubiquitous carbon atoms into an irreplaceable and prototypical 1-D low-dimensional material which is used in diverse research fields ranging from biomedical to mechanical engineering. With its aspect ratio exceeding 10^7, a single-walled

carbon nanotube (SWNT) displays molecular-like behavior along its circumference direction, and bulk-like behavior along its tube axial direction [13]. Its fluorescence not only lacks intensity and spectral fluctuations at room temperature, but also has narrow line width, providing a more desirable single-photon source for the exciting possibility of applications in quantum optics and biophotonics [14]. Because of its strong covalent carbon-carbon sp^2 bonds, its tensile strength is at least ten times stronger than that of steel and its thermal conductivity is larger than that of a diamond [15–18]. Also, due to its ballistic transport properties, SWNT is considered to be a promising candidate for replacing silicon in the semiconductor industry for transistor manufacturors [19], as silicon is approaching fundamental size limitation [20]. In addition, the optical absorption of SWNTs peaks sharply at infrared regime, thereby allowing deeper tissue penetration [21, 22], and its polymer-like nature creates better interactions with molecules or cell membranes. For these reasons, it provides a biocompatible fluorescent probe in photo-thermal therapy and in vivo biological imaging [23, 24]. Furthermore, besides quantum dots [25], a recent discovery of the multiple electron-hole pair generation in SWNTs makes them one of the most promising materials for the next generation of photovoltaic cell development [26].

Application of developed spectroscopy and microscopy imaging methods [27–31] has allowed the scientific research of carbon nanotubes to grow rapidly, despite their heterogeneous nature that makes characterization difficult. In early carbon nanotube research, scanning tunneling microscopy (STM), transmission electron microscopy (TEM), and SWNT-based field effect transistor (SWNTFET) transport measurement were used to confirm the atomic and electronic structures predicted by theory [32–38]. As the properties of carbon nan-

otubes became clear, the identification of chirality emerged as a focus. In order to understand the chirality of SWNTs, much work was done to understand their optical properties [39–50], because photophysics has offered a highly accurate, massless and chargeless probe for single-nanotube studies. By identifying the resonance energies of SWNTs, it is possible to determine the electrical property of an individual SWNT (metallic (M) or semiconducting (S)), and the chiral index, (n, m).

However, although optical characterizations allow for relatively fast and nondestructive probing, as compared to STM, TEM and transport measurements, these optical methods usually provide limited quantitative information for SWNT characterization. This information includes the number of photons participating in the optical transition per carbon nanotube, and spatial resolution, and location of individual nanotubes. In this thesis, we discuss the development of quantitative optical imaging techniques, such as wide-field Rayleigh imaging and confocal absorption imaging techniques, for characterizing single-walled carbon nanotubes. By obtaining intensity, spatial resolution, spectrum, and numerous quantitative values simultaneously, we address questions such as, "how many photons does a SWNT scatter or absorb on resonance?" And "where are the heterojunctions in the SWNT, if there are any?" And, "what happens when two SWNTs are very close to each other?"

1.2 Organization of Thesis

This thesis is organized as follows: Chapter two reviews a description of SWNTs. We first desribe the physical and electronic properties of SWNTs. We

then outline some of the synthesis methods to produce carbon nanotubes for quantative measurement.

Chapter three gives a brief background for optical transition of SWNTs. We first discuss the absorption nature of carbon nanotube using the tight-binding method, and then describe the strong excitonic effect in carbon nanotubes for optical measurement.

Chapter four provides the device fabrication details and discusses the on-chip wide-field Rayleigh imaging technique.

Chapter five describes the excitonic optical wire behavior of SWNTs. We describe the Rayleigh scattering pattern, uniform conductivity and optical coupling of SWNTs.

Chapter six describes the high numerical aperture depolarization effect on confocal absorption imaging, and the absorption cross-section measurement beyond diffraction limit for an individual SWNT.

CHAPTER 2

SINGLE-WALLED CARBON NANOTUBES

In this chapter, we first describe some of the necessary background on the physical and electronic structures of single-walled carbon nanotubes. This includes sp^2 hybridization, graphene band structure, and electronic structures. In the second part of this chapter, we discuss some synthesis methods to produce large quantities of carbon nanotubes, which allows for quantitative measurements of SWNTs. Lastly, we describe optical characterization methods of SWNTs.

2.1 Electronic Structure of Single-Walled Carbon Nanotubes

In this section, following Dresselhaus' book, Carbon Nanotubes[51], we describe the electronic and crystalline structure of SWNTs. First, we discuss the sp hybridization of carbon atoms in crystalline structures. Second, we derive graphene's band structure from the tight-binding method. Lastly, we describe the band structure of SWNTs.

2.1.1 sp hybridization

The ground state configuration of a single carbon atom is $1s^2 2s^2 2p_x^1 2p_y^1$. Its core electrons are in $1s^2$ and the valence electrons are in $2s^2 2p_x^1 2p_y^1$. In the crystalline phase, the valence electrons give rise to $2s, 2p_x, 2p_y$, and $2p_z$. There are three possible hybridization, namely sp, sp^2, and sp^3 for carbon [52]. For example, acetylene is sp, a linear combination of $2s$ and $2p_x$ orbitals; polyacetylene is sp^2,

a linear combination of $2s, 2p_x$, and $2p_y$ orbitals, as the x and y axis span the plane of polyacetylene; methane is sp^3, a linear combination of $2s, 2p_x, 2p_y$ and $2p_z$ orbitals.

2.1.2 Graphene

With atoms arranged in regular hexagonal two dimensional patterns, graphene is understood to be a single atom thick sheet (figure 2.1). Its carbon-carbon bond length is $a_{c-c} = 1.44$ Å with sp^2 hybridization. It was first discovered isolated onto a substrate in 2004, through the scotch tape method [53]. Most recently, graphene has been produced by the chemical vapor deposition (CVD) method [54].

The $2s, 2p_x$, and $2p_y$ combine linearly to form σ bonds in the plane of the graphene, while other $2p_z$ orbitals, perpendicular to the graphene plane, form π bonds. The electronic properties of graphene result primarily from its π bonds. The π bonds give rise to the transfer integral between a carbon atom and its nearest neighboring bonded carbon atoms. By considering the three nearest neighboring atoms for each carbon atom, using the tight-binding method, the transfer integral leads to the off-diagonal Hamiltonian matrix element. The dispersion relation (figure 2.2) for graphene is expressed as

$$E_{g2D}^{\pm}(k) = \frac{\epsilon_{2p} \pm \gamma_0 \omega(k)}{1 \mp s\omega(k)}, \tag{2.1}$$

where

$$\omega(k) = \sqrt{1 + 4\cos\frac{\sqrt{3}k_x a}{2}\cos\frac{k_y a}{2} + 4\cos^2\frac{k_y a}{2}},$$

and $\gamma_0 = 3.013$ eV as the electrons transfer energy for the π bond, $s = 0.219$, and $\epsilon_{2p} = 0$.

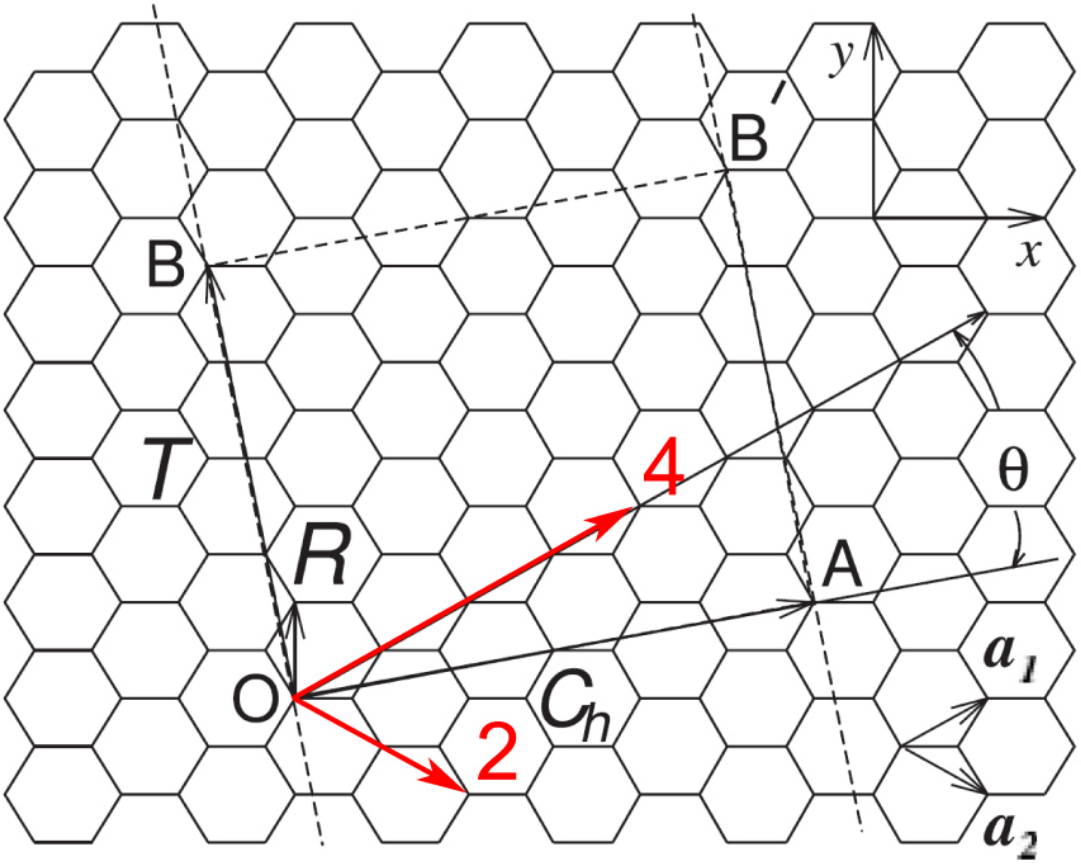

Figure 2.1: **Structure of Carbon Nanotube** - $(n, m) = (4, 2)$ nanotube on a sheet of graphene.

The upper half of graphene's energy dispersion relation reflects the anti-bonding band, and the lower half reflects the bonding band. With two π electrons per unit cell, the Fermi level reaches the lower band at the k point. These bands will be discussed further in next chapter. At the k point, the dispersion relations are approximated to be linear.

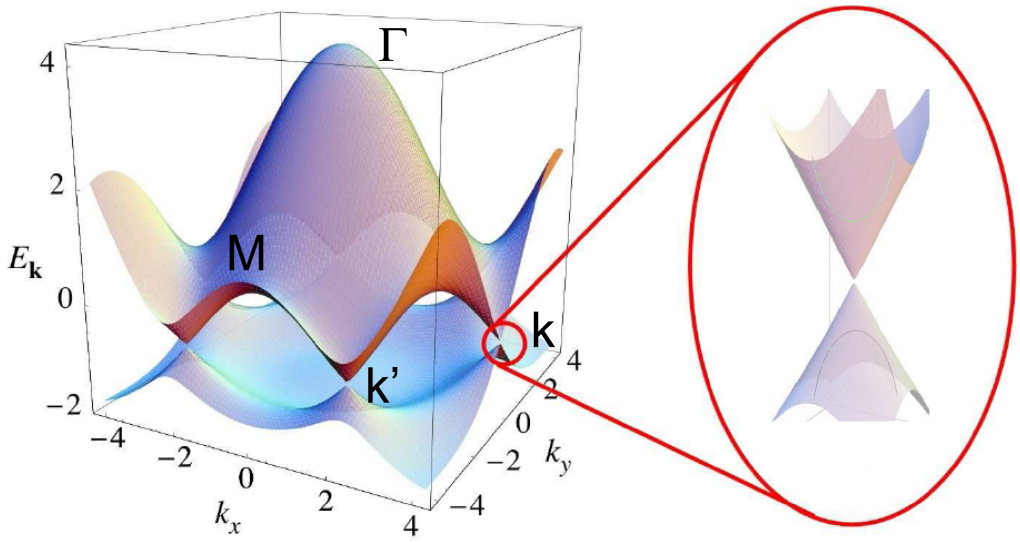

Figure 2.2: **Dispersion Relation of Graphene** - 3D plot of the electronic bands of graphene

2.1.3 Nanotube

Carbon nanotubes were discovered in 1991 by Iijima using transmission electron microscopy (TEM) [12]. Each tube is constructed from a sheet of graphene rolled into a cylindrical tube by joining two sides of the sheet. Depending on how the SWNTs are constructed, various types (chirality) of SWNTs can be created. For example, a (n, m)=$(4, 2)$ SWNT has the chiral vector $\vec{OA}$=C_h, which is expressed as $4a_1 + 2a_2$, as shown in figure 2.1, where a_1 and a_2 are two unit vectors. The angle θ is defined as the chiral angle of the SWNT and $\vec{OB}$ is denoted as the translational vector T. Here, T and C_h define a unit cell of the SWNT.

By associating with the chiral vector C_h, the wave vector is quantized along the circumference, due to the imposed periodic boundary condition; however, the wave vector along the tube axis, by associating with the translation vector T, remains continuous. This quantization, which corresponds to the cross-

sectional cuts of the graphene dispersion relation, defines the energy dispersion relations of the SWNTs. The cuts in figures 2.3 and 2.4 are parabolic in shape and the precise dispersion relations are:

$$E_\mu(k) = E_{g2D}(k\frac{K_2}{|K_2|} + \mu K_1), \tag{2.2}$$

$$\mu = 0, ..., N-1, and -\frac{\pi}{T} < k < \frac{\pi}{T}.$$

Each μ defines a pair of subbands. The location of the cuts in the momentum space relative to the k points determines whether the carbon nanotube is metallic or semiconducting. For metallic SWNTs, there is a cut going through one of the k points, where the conduction band meets the valence band without a band gap. For semiconducting SWNTs, there are no cut lines going through either k point. Here, T is the magnitude of the translation vector

$$T = \frac{\sqrt{3}C_h}{d_R}, \tag{2.3}$$

N is the number of hexagons that lie within the unit cell

$$N = \frac{2(n^2 + m^2 + nm)}{d_R}, \tag{2.4}$$

where d_R is the greatest common divisor of $(2n+m)$ and $(2m+n)$ for (n, m) SWNT, the vectors

$$K_1 = ((2n + m)b_1 + (2m + n)b_2)/Nd_R \tag{2.5}$$

and

$$K_2 = (mb_1 - nb_2)/N, \tag{2.6}$$

define the cuts in momentum space on the cones.

$$b_1 = (\frac{1}{\sqrt{3}}, 1)\frac{2\pi}{a_{c-c}} \tag{2.7}$$

and

$$b_2 = (\frac{1}{\sqrt{3}}, -1)\frac{2\pi}{a_{c-c}} \tag{2.8}$$

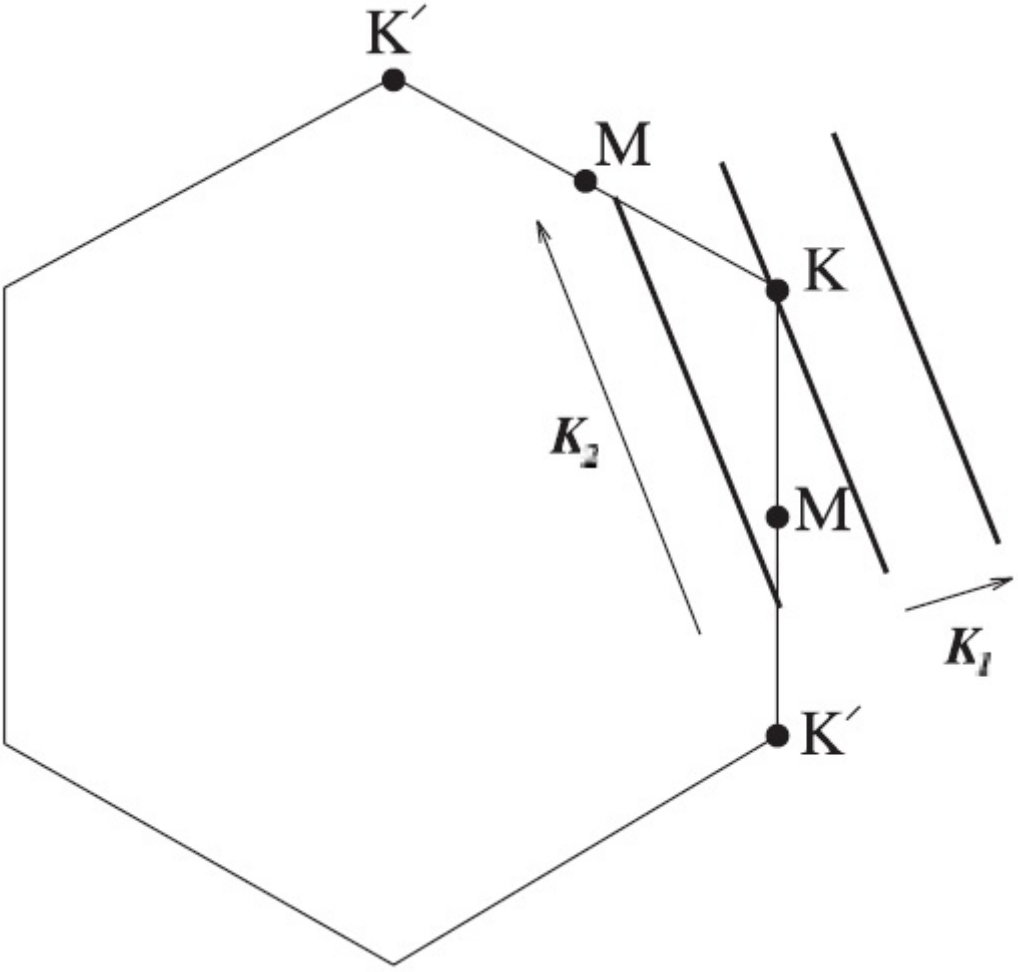

Figure 2.3: **Metallic SWNT Cutting** - K_2 is continuous while K_1 is quantized. For metallic SWNTs, there is a cut at the k point, and the Fermi level reaches the lower band

are the reciprocal lattice vectors.

As mentioned above, since the dispersion relations of SWNTs are parabolic in shape, there are one-dimensional van Hove singularities (vHs) in the density of states, which are at the extremum of the parabolic curves.

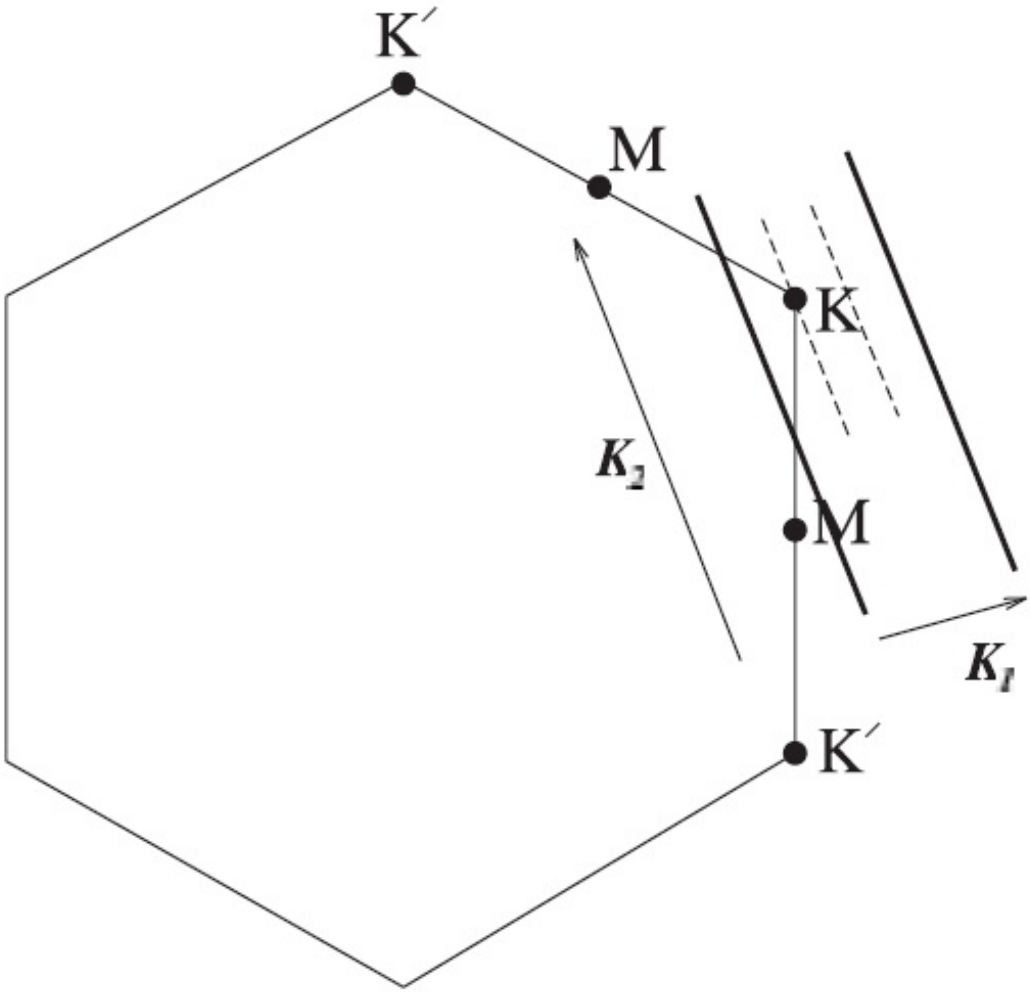

Figure 2.4: **Semiconducting SWNT Cutting** - For semiconducting SWNTs, there are no cuts at the *k* point

2.2 Synthesis of Single-walled Carbon Nanotube

The study of carbon nanotubes can be traced back to bamboo filaments that were used for incandescent light bulbs by Edison [55]. Although tungsten filaments replaced bamboo filaments, the research of carbon fibers and filaments grew over time with efforts mostly toward to the study of their vapor growth [56, 57]. As the growth of carbon fibers using vapor grown methods proceeded

to the micrometer scale, occasionally exceptionally small diameter filaments were observed and reported [58, 59], although systematic studies were not carried out. Due to the momentum of fullerene research, scientists started to pay more attention to carbon filaments of very small diameters. Several conjectures and speculations about carbon nanotubes with dimensions comparable to C_{60} were proposed. Since the pioneering work of Iijima from experimental observation of multi-walled carbon nanotubes using TEM [12], synthesis of carbon nanotubes has progressed rapidly. In 1993, the experimental discovery of single-walled carbon nanotubes further stimulated work in the field [60], although only small quantities of SWNTs were available. Not until 1996, after the discovery of a more robust method to synthesise SWNTs using laser vaporization of graphite [61], quantitative experimental studies were rapidly expanded. Detailed mechanisms responsible for the growth of nanotubes are not yet well understood. However, the discovery that catalyst species are necessary for the growth of the single-walled carbon nanotubes did help scientists understand a large part of this mechanism.

2.2.1 Laser Vaporization Method

Laser vaporization method uses graphite target [61]. 1.2 atom % Co-Ni alloy with equal amounts of Co and Ni added to the target. While the target is resting inside a quartz tube heated to $1200^{\circ}C$ with argon gas flowing, a neodymium-yttrium-aluminum-garnet pulsed laser is used to evaporate the graphite. While the argon gas carries the nanotubes, the nanotubes are collected by a water-cooled copper collector at the downstream. Ropes of carbon nanotube, with 10-20 nm in diameter and up to 100 μm or more in length, can be produced by

this method. The diameters of the single-walled nanotubes, which are forming the ropes, have a strongly peaked distribution at 1.38 nm.

2.2.2 Carbon Arc Method

Another method of producing single-walled carbon nanotubes is the carbon arc method. This technique produces multi-wall carbon nanotubes and ropes of single-walled nanotubes, in addition to isolated single-walled carbon nanotubes [62]. With both carbon rod electrodes of 5-20 mm diameter separated by around 1 mm with a voltage of 20-25 V across the electrodes, and a dc current of 50-120 A flowing between the electrodes, a plasma can be created in between the electrodes. Carbon nanotubes are form on the negative side of the electrodes, while the length of positive electrodes decreases. In order to produce isolated single-walled carbon nanotubes, catalysts are used. These catalysts include transition metals such as Co, Ni, Fe and rare earths such as Y and Gd.

2.2.3 Chemical Vapor Deposition Method

A more robust and controllable method, used by many current researchers, is chemical vapor deposition method. A variety of hydrocarbon gases is used to react with Fe, Co, or Ni particles in a reaction tube with a temperature between 900 and 1100 °C [63]. With optimum controlled conditions, the carbon nanotubes can be made continuously, providing a means of producing large quantities of nanotubes for quantitaive measurements.

2.3 Optical Characterization Methods

In tandem with developing more robust methods to produce carbon nanotubes, characterization of physical properties of SWNTs became one of the main foci in low-dimensional structure studies. Optics has become a powerful practical tool for identifying the distribution of nanotube chiralities in a sample. Experimentally, the techniques are readily available, relatively simple to perform, quick, and can be performed at room temperature and under ambient pressure. In addition, the optical techniques are nondestructive and noninvasive because they use the photon, a massless and chargeless particle, as a probe. The (n,m) identification of nanotubes can be performed by using photoluminescence, resonant Raman scattering and Rayleigh scattering.

2.3.1 Photoluminescence

The term photoluminescence (PL) describes any process through which light is absorbed by a medium, generating an excited state, and then light of lower frequencies is re-emitted upon relaxation to a ground state. In nanotube optics the term fluorescence is used synonymously and is actually more precisely correct as it describes allowed PL processes for which the timescale between absorption and emission is a few nanoseconds or less. In the currently accepted picture of SWNT PL, when a SWNT is photoexcited, electron-hole pairs are created in the form of excitons, which are subsequently recombined with the emission of photons [11].

The breakthrough that began the era of PL studies on SWNTs was at first

one of purification, with isolated SWNTs being separated from bundled ones and dispersed in solution[45]. The absorption spectra of the separated SWNTs showed a series of sharp peaks ($\approx$ 25 meV), rather than broad peaks seen in bundles. In contrast to bundled samples, these separated SWNTs in suspension also showed sharp PL peaks in the near-infrared when excited with laser illumination in the visible regime. The emission spectrum has virtually identical energies and similar linewidths ($\approx$ 25 meV) as the absorption spectrum. This led to the conclusion that the same states are responsible for both processes and that the luminescence involves transitions between band extrema in semiconductors (i.e., from E_{11}^S). Since this original work, many other recipes using a variety of surfactants have been tested by several groups. One advantage of PL is allowing the mapping of (E_{22},E_{11}) [44, 45], comparing to Raman scattering and Rayleigh scattering. However, PL signals from SWNTs can only be measured on isolated semiconducting SWNTs.

2.3.2 Resnant Raman Scattering

Raman spectroscopy is commonly used for characterizing SWNTs because it is one of the most sensitive characterization tools for these nanostructures and requires very little work (or no work) on sample preparation [40, 64]. The Raman spectra from carbon nanotubes is rich and can be used to characterize several aspects of isolated, bundled and processed samples. Generally speaking, the Raman spectra depend strongly on the excitation laser energy (E_{laser}) because only nanotubes in resonance with E_{laser} exhibit a strongly enhanced Raman signal. For this reason, resonant Raman spectroscopy (RRS) is a dominant optical characterization technique. Usually, a main disadvantage of Raman spectroscopy

is the low-signal intensity as compared to PL, although RRS can also measure metallic SWNTs.

There are two important Raman modes for characterizing SWNTs, namely, radial bradthing mode (RBM) and tangential G band mode. The RBM is unique to carbon nanotubes and is not observed in other carbon materials. The RBM mode frequency is proportional to the inverse tube diameter. The RBM frequencies typically range from $500 - 50cm^{-1}$. There are many different ω_{RBM} vs. d_{NT} relations in the literature, probably due to the different environmental conditions of each particular measurement.

While the G band in graphite has a single peak at 1582 cm^1, the G band in SWNTs is composed primarily of two stronger peaks G- and G+, which have been attributed to the circumferential (TO) and axial (LO) atomic vibrations, respectively [51]. The splitting of these two peaks depends on the tube-wall curvature, so that the G peak structure has a small frequency dependence on d_{NT} that can be used to corroborate the diameter information obtained from the RBM. The most important characteristic is the strong lineshape dependence of the G- peak on the tube type and doping. While in semiconducting tubes the circumferential TO mode has a lower frequency when compared to the axial LO mode, the opposite happens in metallic tubes. The LO mode in metallic tubes shows up at a much lower frequency than the G- peak (TO) from semiconducting tubes, and it exhibits a broad and asymmetric Fano lineshape, due to the interference of the discrete phonon state with continuum electronic state [65]. This broad feature has been largely used to distinguish between metallic and semiconducting tubes.

2.3.3 Rayleigh Scattering

Single-walled carbon nanotubes can be probed optically by elastic light scattering [43]. Due to the elastic scattering mechanism, the Rayleigh scattering signal is much stronger than that of RRS. Since the nanotube (its diameter) is an object much smaller than the wavelength of light, this method has been termed Rayleigh scattering spectroscopy. The advantages of this method include its applicability to both semiconducting and metallic nanotubes, the simple interpretation of the information that the method yields, and the high data collection rate that it can provide at the individual nanotube level. However, since nanotube is a small object, the influence of background scattering limits this method. We discuss Rayleigh scattering further in Chapter 4.

CHAPTER 3

OPTICAL TRANSITION OF SWNT

3.1 Theory of Optical Transition

3.1.1 Absorption Cross Section

Optical transition between atomic states can be understood from perturbation theory, as the off diagonal terms of the Hamiltonian connect the states. Roughly following the derivation of Sakurai [66], optical transition of atoms can be derived from Fermi's Golden Rule, where the rate of transition is proportional to the absorption cross section:

$$\sigma_{abs} = \frac{4\pi^2\hbar}{m_e^2\omega}(\frac{e^2}{\hbar c})|\langle n|\, e^{i(\omega/c)(\widehat{n}\cdot x)}\widehat{\epsilon}\cdot p\,|i\rangle|^2\delta(E_n - E_i - \hbar\omega), \tag{3.1}$$

where we assume the atom is in the initial state $|i\rangle$ and excited to state $|n\rangle$ by a monochromatic plane wave,

$$\mathbf{A} = 2A_0\widehat{\epsilon}\cos(\frac{\omega}{c}\widehat{n}\cdot\mathbf{x} - \omega t),$$

with $\widehat{\epsilon}$ and $\widehat{n}$ being the polarization and propagation directions, respectively. From the dipole approximation, this expression is written as:

$$\sigma_{abs} = 4\pi^2\frac{e^2}{\hbar c}\omega_{ni}|\langle n|\, x\,|i\rangle|^2\delta(\omega - \omega_{ni}). \tag{3.2}$$

The transition follows the selection rules, due to the parity of the operator and the atomic states. The idea of selection rules is used to guide us to understand whether an optical transition is allowed. The allowed interband transition for $E_{i,i\pm1}$ of SWNTs with perpendicular polarization to the tube axis, and utilization

of two photon spectroscopy to conclusively confirm the large effect of excitons in SWNTs, are two examples of parity argument between states and operator in selection rules. The absorption cross section has a unit [(energy/unit time) absorbed by the atom ($|i\rangle \rightarrow |n\rangle$)]/(energy flux of the radiation field), which reduces to m^2. Furthermore, conservation of energy and momentum can be derived from equation 3.1.

For solid-state crystals, electronic states of a crystal will be linear combinations of the atomic orbitals (Bloch's Theorem)[67]. Experimentally, absorption cross section is measured by following the Beer's Law. With initial intensity, I_o, a light beam of a specific wavelength travels through a crystal with x unit of length, and we measure the intensity, I_1, coming out of the crystal. Beer's Law is expressed as:

$$I_1 = I_o exp(-\alpha x) = I_o exp(-\sigma_{abs} n x), \tag{3.3}$$

where n is the number of particles per unit volume of the crystal, and α is the absorption coefficient with unit 1/m. Traditionally, σ_{abs} is an important value, as it gives rise to the maximum intensity of a typical laser from Einstein A and B coefficients [68].

In the case of graphene, for low energy excitation, the interband optical absorption transition is between the bonding and anti-bonding bands, which are the linear combination of p_z orbitals. Experimentally, this transition results in an absorption value around 2.3% per layer of graphene[69].

3.1.2 Absorption in Conventional 3D Semiconductors and 1D SWNTs

Optical absorption of SWNTs can be understood in a similar way as in conventional 3D semiconductors. In both cases, the optical absorption is associated with light-induced excitations of electrons from the valence band to the conduction band. Therefore, the light absorption generally increases with increasing joint density of states and its peaks can be used to determine the energy gap of a semiconductor. However, because the transitions are subject to certain selection rules as mentioned in the previous section, in addition to conservation of crystal momentum, estimating the energy gap from the "absorption edg" is not a straightforward process [70]. One well-known example of this is the optical properties of silicon, an indirect bandgap semiconductor.

Because the momentum of a photon, h/λ (λ, is the wavelength of light, on the order of hundreds of nanometers in the visible regime), is several orders of magnitude smaller than the crystal momentum h/a (a is the lattice constant, a few tenths of a nanometer), the photon-absorption process should conserve the momentum of the electron (figure 3.1).

Assuming $0°K$, we consider absorption transitions between two direct valleys, where all momentum-conserving transitions are allowed. Every initial state at E_i is associated with a final state at E_f such that:

$$E_f = \hbar\omega - |E_i|. \tag{3.4}$$

In parabolic bands,$E_f - E_g = \frac{\hbar^2 k^2}{2m_e^*}$ and $|E_i| = \frac{\hbar^2 k^2}{2m_h^*}$, where m_e^* and m_h^* are the

effective mass of the electron and hole, respectively, and E_g is the band gap of the semiconductor. We have: $\hbar\omega - E_g = \frac{\hbar^2 k^2}{2}(\frac{1}{m_e^*} + \frac{1}{m_h^*})$. In *bulk* semiconductors, the density of state is expressed as:

$$N(\hbar\omega)d(\hbar\omega) = \frac{8\pi^2 k^2 dk}{(2\pi)^3} = \frac{(2m_r)^{3/2}}{2\pi^2\hbar^3}(\hbar\omega - E_g)^{1/2}d(\hbar\omega), \tag{3.5}$$

where m_r ($m_r = 1/m_e^* + 1/m_h^*$) is the reduced mass. Therefore the absorption coefficient is expressed as:

$$\alpha = A^*(\hbar\omega - E_g)^{1/2}, \tag{3.6}$$

where

$$A^* \approx \frac{q^2(2\frac{m_e^* m_h^*}{m_e^* + m_h^*})^{1/2}}{nch^2 m_e^*}$$

and n is the index of refraction of the bulk semiconductors.

This absorption coefficient, derived for 3D semiconductors in equation 3.6, is significantly different for interband optical absorption in SWNTs. It is well known that the density of states for 1D structures near its band edge is given by $N \propto 1/\frac{dE}{dk} \propto (\hbar\omega - E_g)^{-1/2}$, which produces the van Hove singularities (vHs) [71]. Within a noninteracting single-particle picture, the optical absorption coefficient is given by $\alpha \propto (\hbar\omega - E_g)^{-1/2}$, which gives rise to sharp peaks in optical absorption under the resonance conditions ($\hbar\omega = E_g$).

3.1.3 Single Particle Picture for Interband Optical Transition

Apart from the conservation of momentum ($\delta k \approx 0$), the optical transition of SWNTs follows a set of selection rules due to the symmetry of carbon nanotube. It has been shown that every nanotube with particular chirality (m, n) belongs to the corresponding specific symmetric group [72–75]. From Bloch theorem,

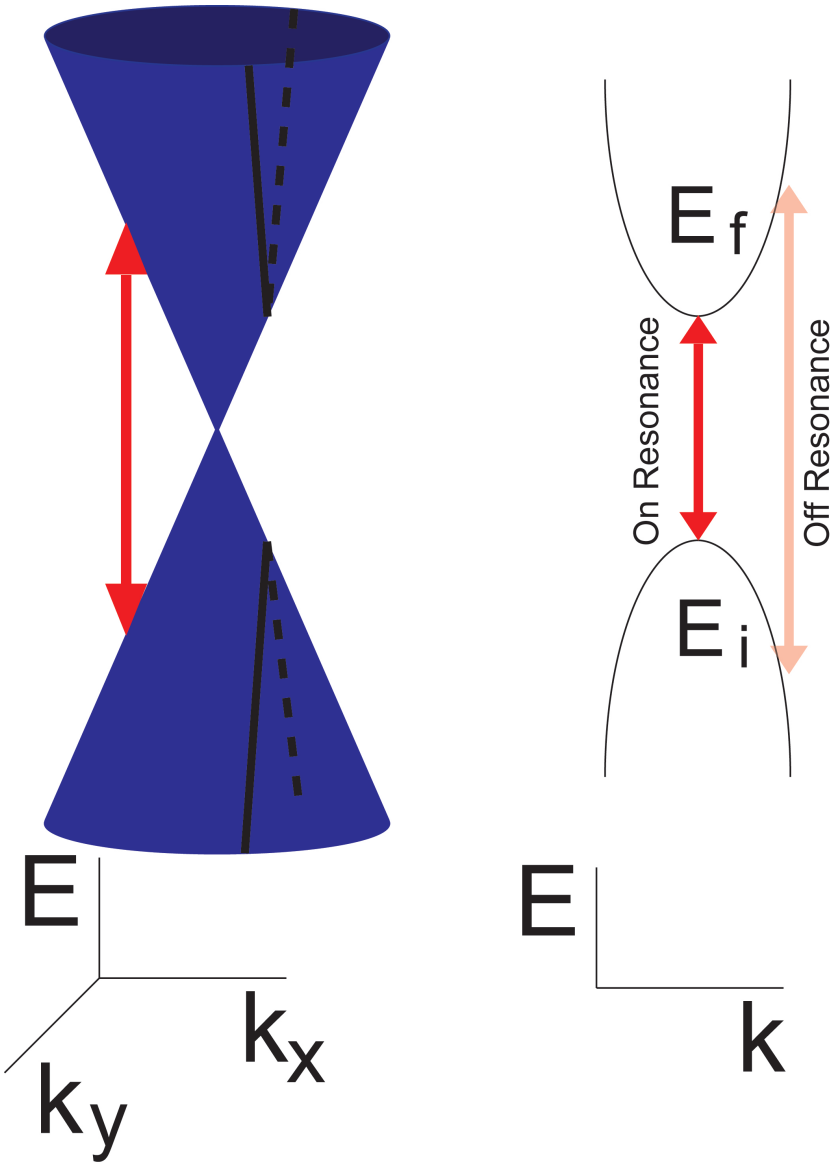

Figure 3.1: **Interband Optical Absorption for Graphene and SWNTs** - Double arrows indicate the optical absorption transition. The left image represents that of graphene. The right-side image shows the E_{11} transition for a SWNT, along the cut shown on the left-side image.

the electronic states of SWNTs are the manifestation of the symmetric group, corresponding to different (m, n) [1]. This gives rises to the selection rules for the dipole matrix elements of SWNTs [76]. Transition can occur either between a pair of subbands with the same μ in equation 2.2 or between neighboring pairs with different μ. These selection rules are expressed as follow.

- $\delta\mu = 0$ for $\widehat{\epsilon}$ along the tube axis, within a pair of subbands
- $\delta\mu = \pm 1$ for $\widehat{\epsilon}$ perpendicular to the tube axis, between neighboring pairs

The interband optical transitions for polarization perpendicular to the tube axis are observed in SWNT bundles and solution [77, 78], and they correspond to the $E_{\mu=i,\mu=i\pm1}$ transitions. That is because the dipole matrix has non-zero elements, which are connecting states having μ to states having $\mu \pm 1$ in equation 2.2, for perpendicular polarization, $\widehat{\epsilon}$. This can be considered as the perpendicular light introducing a step increment to the K_1 vector, which is associated with the chiral vector (C_h in figure 2.1) of the carbon nanotube. Furthermore, The absorption cross section for light polarized along the nanotube axis is about 5 times larger than when the polarization is perpendicular to the axis [78].

In this thesis, we only investigate SWNTs with relatively small diameters. As small diameter resulting larger K_1 step in equation 2.5, the changing of δk in momentum requires photon assist processes. As a result, for the rest of this thesis, we only consider E_{ii} transition, for polarization along the tube axis.

For polarization parallel to the tube axis, according to model from equation 2.2, the direct optical transition between bands in a semiconducting nanotube makes two predictions for experiments:

[1] This is a consequence of eigenfunctions' properties due to the commuting relations between the Hamiltonian and symmetry operators.

- E_{ii} should scale linearly with $1/d_R$.
- The ratio E_{22}/E_{11} should be 2.

However, these predictions do not match with experimental optical data [44, 45, 79–88]. This is further discussed in the next section.

3.2 Excitonic Effect in Optical Measurement of SWNTs

3.2.1 Many Body Effects

In previous section, we discussed two simple predictions from the model calculated by tight binding method for parallel polarization. However, the experimental data disagree with both of these predictions [44, 45, 79–88]. First, E_{ii} scales nonlinearly with $1/d_R$, and is always larger than this model predicts. There are corrections that scale like $1/{d_R}^2$ from trigonal warping and curvature [11, 89], but even if these are included, this model cannot explain the data. Second, the ratio of E_{22}/E_{11} is always smaller than 2, and approaches 1.85 in the limit of larger d_R (the so-called ratio problem) [45]. Lastly, the simple tight-binding calculation can not address the family patterns in experimental Kataura plot observed in 2D PL plots for tube diameter less than 1 nm [44]. These problems arise from trying to interpret the data with a noninteracting electron picture as shown in figure 3.1.

If electron-electron interactions are taken into account, all of these problems can be resolved. Due to strong electron-electron interactions, a significant increase in the energies of continuum-states, and the formation of a strongly

bound excitonic state, are predicted [90]. The nature of the optical excitation in SWNTs is determined by the structure of the excitonic states. Experimentally, this is conclusively confirmed by measuring the binding energy of exciton using nonlinear two-photon absorption measurements, from which much of the present knowledge of the exciton binding energy has been extracted [41, 91]. In those experiments, researchers measured the energy difference between the ground state and the lowest-energy exciton of the E_{11}^S levels, and used the results to calibrate the dielectric constant of the environment based on a first-principles theory. The result from these authors is consistant with each other, and the binding energy is roughly $E_b = 0.3/d_R[nm]$ in electron volts.

Due to dipole selection rules, single-photon and two-photon processes probe states with different symmetries or selection rules [92, 93]. The absorption of a single photon creats a particle-hole pair with a dipole moment, a state that has odd parity. Absorption of two photons creates a state that is even and has no dipole moment [2]. In the absence of electron interactions, the even and odd states are degenerate. As a result, the absorption of two photons of frequency ω_a should be followed by emission of a single photon of frequency $\omega_e = 2\omega_a$. Phonons modify this picture by allowing a high energy state to relax to the band edge. However, the onset of absorption and emission for both one- and two-photon processes should occur at the same energy even when phonon interactions are included. This is not observed in two-photon photoluminescence experiments: the single-photon emission energy is always lower than the two-photon absorption energy by a couple hundred meV [41, 80, 91, 94]. This indicates that the excitonic effect in the optical processes of SWNTs can not be

[2] Intuitively, this can be understood roughly as follow: for single photon absorption, we have $\langle n| x |i\rangle$, while for two photon absorption, we have $\langle n| x \cdot x |i\rangle$, refering to equation 3.2. Therefore, the absorption of two photons requires the initial and final electronic states to have the same parity.

ignored.

3.2.2 Coulomb Interactions in SWNT

In order to understand the excitonic effect, we need to look into the Coulomb interaction of charged particles. The three effects of the Coulomb interaction that are most relevant to the optical properties of carbon nanotubes are screening, self energy, and excitons. If an electron is added to a crystal, the electrons in the system will be repelled and the ionic cores will be attracted. This will lead to variations in what used to be a uniform charge distribution. The collection of positive charge around the electron reduces its charge as seen by distant particles. This is referred to as screening. In low-dimensional materials like carbon nanotubes and graphene, screening is not as effective. The electric field of a charged particle extends into three dimensions, but the screening cloud is confined to a plane in the case of graphene, or to a line in the case of a nanotube. The result is that a charged particle is unscreened at short and long distances, and interactions between charged particles are much stronger.

When an electron moves through a crystal, its dispersion relation will be different than if it were moving through a vacuum. The Coulomb interaction leads to correlations in the motion of an electron and the screening charges around it. The net effect is to increase the effective mass of a charged particle. The additional energy acquired by a particle due to its interactions with surrounding particles is called a self energy.

The Coulomb attraction between a positively charged hole and a negatively charged particle allows them to form a bound state called an exciton. The bind-

ing energy of the exciton makes it lower in energy than a free particle-hole pair. Excitons are usually divided into two classes depending on their size: Frenkel excitons and Wannier excitons. Frenkel excitons are tightly bound and highly localized. The separation of the particle and the hole is on the order of the atomic spacing, so the exciton does not interact with the lattice potential. It may be described in terms of excited states of one or two atoms. Wannier excitons are delocalized and less tightly bound. The particle and hole are spread out over many lattice sites and interact with the lattice potential. As a result, they can be described by envelope functions multiplied with Bloch waves. There is no fundamental difference between the two types: they both describe a highly-correlated particle-hole pair moving through the lattice. The excitons in carbon nanotubes are best described in the language of Wannier excitons [52]. The particle and hole are delocalized around the circumference of the nanotube, and the spread of the exciton wave function along the axis is on the order of the tube radius [80, 95].

Numerical calculations of exciton wave functions and energies can follow from Ando's outline [90]. By considering the screened Coulomb interaction from random phase approximation, and electron and hole self energies, the Bethe Salpeter equation results the exciton wave functions and energies.

3.2.3 Exciton Relaxation Pathways in SWNT

The ratio problem in the PL measurements presents one of the challenges for single particle model [44]. From single particle picture, the ratio of the excitaion energy of the second peak in the PL measurement to the fluorescence

emission energy is predicted to be two [79, 86–88]. As mentioned in previous sections, experimentally this ratio asymptotically approach to 1.85. This discrepancy is mainly due to the lack of electron-electron interaction in the single particle model. However, as Kane and Mele point out, the solutions of the ratio problems are not only requiring to indentify the effects of the electron-electron interactions in the optically excited states, but also consider several unique intrinsic relaxation mechanisms that derive from one dimensionality and geometry of SWNTs [81]. Kane and Mele summarize the possible intrinsic relaxation mechanisms as follow (figure 3.2).

- An exciton created at the second subband edge can relax by decaying into an unbound electron-hole pair in the first subband with **nonzero** kinetic energy.
- An exciton created at the second subband edge can relax by decaying to a two electron-two hole state with **zero** kinetic energy [3].

The Coulomb interaction, which associates with finite momentum relaxation processes, has the scaling behavior approximately as $1/d_{NT}$. This is similar to the scaling of band gaps in SWNTs. The scalling behavior of Coulomb interaction leads to uniform peak optical conductivity in SWNTs. This is discussed in Chapter 5.

[3] Interestingly, multiple electron-hole pair generation starts with a creation of an exciton within a SWNT [26].

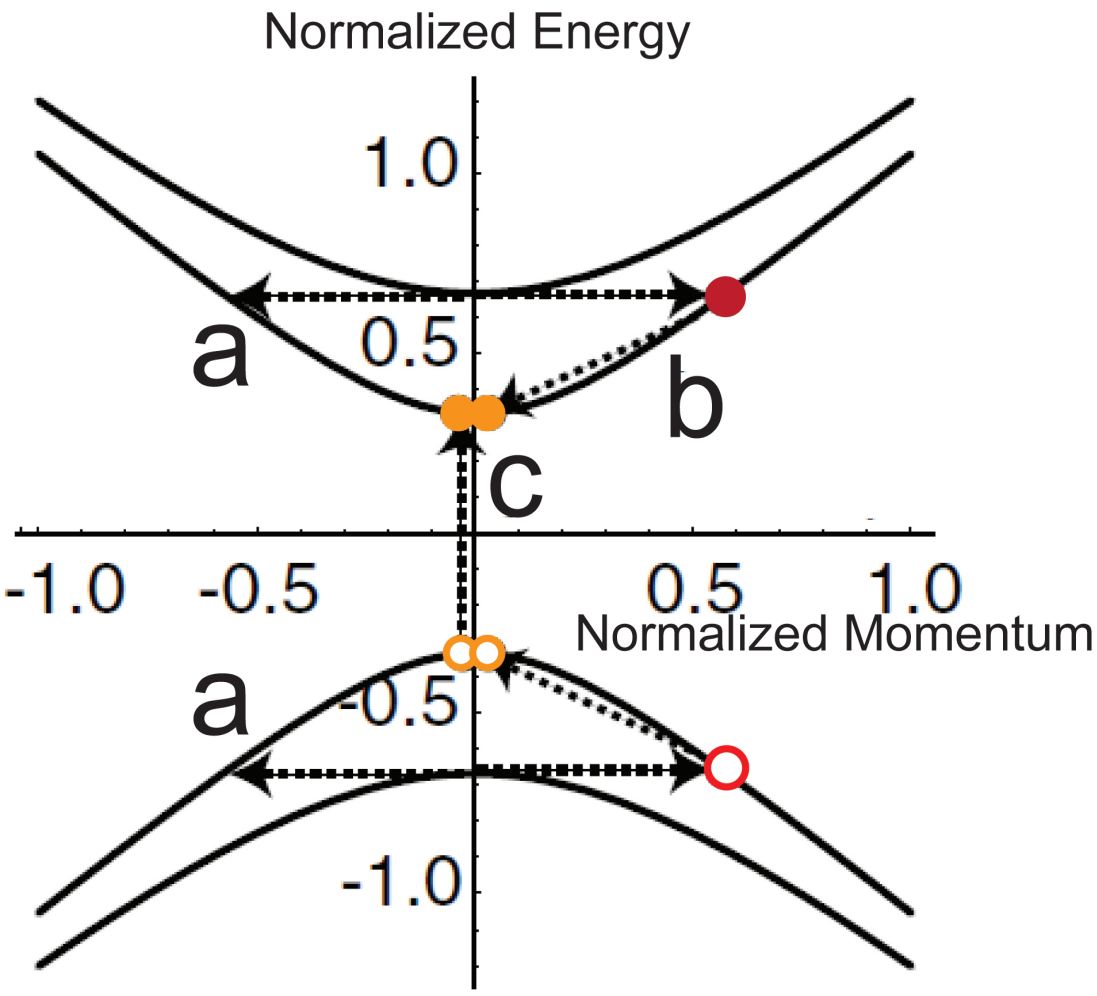

Figure 3.2: **Relaxation Pathways For the Electron Hole Pair in the Seccond Suband** - (a) The electron hole pair in the second subband can decay into a single electron hole pair (red solid and hollow circles) in the first subband, or to a two electron-two hole state (orange solid and hollow circles)(b), (c)

CHAPTER 4

SAMPLE FABRICATION AND RAYLEIGH IMAGING AND SPECTROSCOPY

This chapter is split into two sections. The first section is about the sample growth and fabrication of parallel SWNTs on a quartz substrate, which needs to be very clean for optical experiments. On the second section, we describe the experimental setup of on-chip wide-field Rayleigh imaging and spectroscopy developed by us. We mention some of the experimental finding at the end of this section.

4.1 Sample Fabrication

This thesis investigatates aligned SWNT samples. Due to experimental challenges (discussed in later sections), the samples are required to be extremely clean. We detail how to obtain such samples for optical measurements in this chapter. Before going into specific details, we outline the steps involved in making clean SWNT samples on quartz. The following are principle steps of sample fabrication:

1 We start with double-sided and polished transparent ST-cut quartz wafers. In the first step, we define the alignment markers for later lithography steps and sample characterization.

2 In the second step, we define catalyst strips using photolithography.

3 After catalyst deposition, we grow SWNTs by CVD in a furnance.

4 We then anneal the samples before optical measurements.

All of the tools used for the above steps are available in the Cornell Nanotechnology Facility (CNF). The following details provide guidance for successful sample fabrication.

4.1.1 ST-cut Quartz

There are several quartz wafer vendors, however only Hoffman Materials provides wafers of quality high enough for the subsequent steps. All wafers are double-side polished, and have a major cut to define the crystal orientation. Each wafer is entirely coated with primer and then photoresist. During photoresist soft baking, the quartz wafers warp and heat distribution is not uniform.

It is difficult to make photolithographic tools focus on the substrate, because it is transparent. We typically use Autostepper in the cleanroom to define alignment markers. After developing the photoresist, 15 minutes of etching time for SiO_2 setting in dry etching chamber (Oxford 82) is required to define the etched alignment markers on the wafer. Prior to stripping the photoresist, 1 minute of oxygen plasma cleaning in Oxford 82 is required to clean off the hardened photoresist layer. If the wafer is not protected by the photoresist and treated in oxygen plasma environment or a MOS cleaning environment, the wafer's surface will be destroyed, and the SWNTs will not grow straight. Prior to wafer dicing (10 by 15 mm), the wafers should again be protected by photoresist to prevent dust deposition.

After dicing, the substrates are cleaned in acetone and isopropyl alcohol (IPA), and then annealed at $900^{\circ}C$ for 12 hours in the air. Cleaning in this environment rids the surface of defects.

An important word of caution should be mentioned here. Since the surface crystal orientation is the main reason for aligned SWNTs growth [96], any harsh chemistry processes could damage the surface.

4.1.2 Catalyst Depositions

There are two ways to deposit SWNT catalysts. All SWNT catalysts we use in our experiments are iron based. The first method allows us to create a higher-density of aligned SWNTs. The second method yields a lower density of aligned SWNTs. In the first method, we start by mixing ferric nitrate into photoresist. After coating the substrate with modified photoresist, we expose a large area and leave narrow strips ($2 \sim 5\,\mu$ m) of photoresist unexposed. After developing the resist, the unexposed strips are the only area containing the catalysts. Prior to the SWNTs' growth, the edges of the substrate are wiped clean with acetone. To create iron based particles and burn off the photoresist, we put the substrate into the furnance for 30 minutes at $700^{\circ}C$ in air. The substrate is then ready for SWNTs growth.

The second method is similar to the approach used to deposit metallic electrodes. After coating the substrate with normal photoresist, we expose the resist to form narrow lines of trenches. After 1 minute of oxygen plasma cleaning, pure iron particles are evaporated onto the substrate by physical vapor deposition (e-beam). After removing the photoresist with acetone and IPA, the substrate is ready for growth.

4.1.3 Aligned Growth of SWNTs

Once we have catalysts deposited on the substrate, we follow a growth method which is modified from the growth method described by John Rogers' group [97]:

1. Place the substrate in the center of the furnance, then raise the temperature of the furnance to $700^{\circ}C$ in air environment.
2. With Ar gas flowing at 3000 sccm flow rate, connect the gas lines to the furnance in the same direction as the gas flow. Let the gas flow for 5 minutes. This will flush oxygen out of the furnance.
3. Set the temperatue to $800^{\circ}C$, while flowing 500 sccm Ar. This should last for 5 minutes.
4. Switch Ar to H_2, with 750 sccm flow rate. Allow this to sit for 15 minutes.
5. Set the temperature to $900^{\circ}C$, while H_2 and Ar flow at a rate of 400 sccm and 150 sccm, respectively.
6. Once the temperature reaches $900^{\circ}C$, switch the Ar line so that it flows through the ethanol bubbler. At this point, the growth starts. Allow it to sit for 15 minutes.
7. Set the temperature to room temperature, switch the Ar back to the normal line, and then set Ar and H_2 flow rates to 200 sccm.

After growth, the sample can be characterized by SEM (figure 4.1).

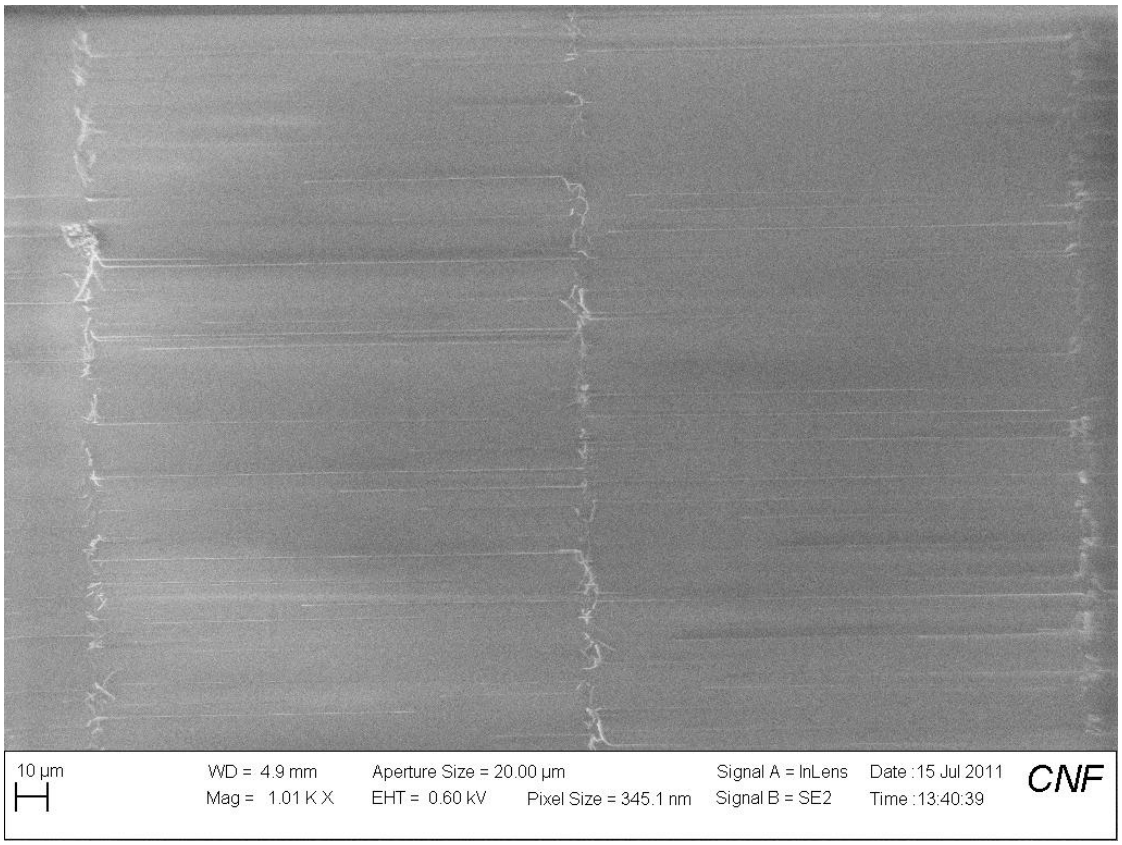

Figure 4.1: **SEM Image of SWNTs on Quartz** - SEM imaging was conducted in the CNF.

4.1.4 Special Sample for Rayleigh Spectroscopy

In Rayleigh imaging and spectroscopy (see next section), the sample requires special preparation. First, we anneal the sample (SWNTs on quartz substrate) at 550°C in a H_2 and Ar environment for 30 minutes. Second, we use a piranha solution (3:1 ratio of $H_2SO_4 : H_2O_2$) to clean coverslips ($\approx 150\,\mu$m thick, Corning No. 1) for 30 minutes. The coverslips are then soaked in clean water, rinsed in IPA, and then blown dry by N_2 gas. We then apply two small strips of Scotch Tape to mount the sample to the coverslip, with one drop of glycerol (Fisher Scientific) being applied in between (figure 4.3).

4.2 Rayleigh Imaging and Spectroscopy

Rayleigh scattering is the elastic scattering of light by particles, the size of which is significantly smaller than the wavelength of the light. It was named after the British physicist Lord Rayleigh [98]. One well known consequence of Rayleigh scattering is the blue color of sky. The sunlight is scattered by small particles in the atmosphere, and because the scattering intensity for spherical particles (having diameter, d) is related to the wavelength of the light, by $I \propto \lambda^{-4} d^{6}$, the sky is greatly illuminated by scattered blue light [99].

Rayleigh spectroscopy for characterizing SWNTs has been proven to be a useful tool. Due to the elastic Rayleigh scattering mechanism, the scattering intensity provides a stronger signal than that of Resonant Raman spectroscopy (RSS). We first describe previous Rayleigh experiments and explain the reason for developing on-chip wide-field Rayleigh spectroscopy and imaging. Second, we discuss the expected behaviors of SWNTs, which are observed by on-chip Rayleigh scattering measurements. Lastly, several newly discovered properties of SWNTs are presented at the end of this chapter.

4.2.1 Rayleigh Scattering Measurement of Suspended SWNTs

Rayleigh spectra of SWNTs were first measured at Columbia University using suspended geometry [43]. They grew nanotubes across a trench that was etched through. A supercontinuum (white light) laser source was focused onto the SWNT, and a lens placed away from the laser pathway was used at the back of the substrate to collect the scattered light from the SWNT. Rayleigh spectra of

the SWNTs were obtained based on which their chiral indices were determined. Furthermore, this assignment was compared with TEM measurements. This method is proven to be noninvasive and to allow for faster data acquisition, compared with other optical characterizations, such as PL and RRS [39, 40, 44–48, 50]. However, the fabrication process for suspended geometry is complicated and tedious. After etching through the trench, only nanotubes with a diameter of 1.5 nm or larger can be grown across the trench. In the next section, we discuss how to avoid suspended geometry and obtain the Rayleigh spectra of SWNTs.

4.2.2 Experimental Setup of On-chip Rayleigh Scattering for SWNTs

If the substrate is perfectly flat with only nanotubes on it, we can easily obtain the Rayleigh scattering spectra of these nanotubes by shining light onto the substrate. However, obtaining perfect flatness is not possible in the real world (figure 4.2). That is one of the reasons why suspended geometry was used previously to obtain Rayleigh scattering for nanotubes. On the other hand, it is possible to create a virtually invisible substrate for SWNTs by selecting the correct medium to match the refractive index. By combining refractive index-matching and total internal reflection, we are able to obtain the Rayleigh spectra of carbon nanotubes directly without suspension.

To overcome these problems, a broadband laser-based darkfield microscope was developed to minimize the background scattering without suspending the SWNTs [100]. As explained earlier, the substrate with SWNTs was coated with

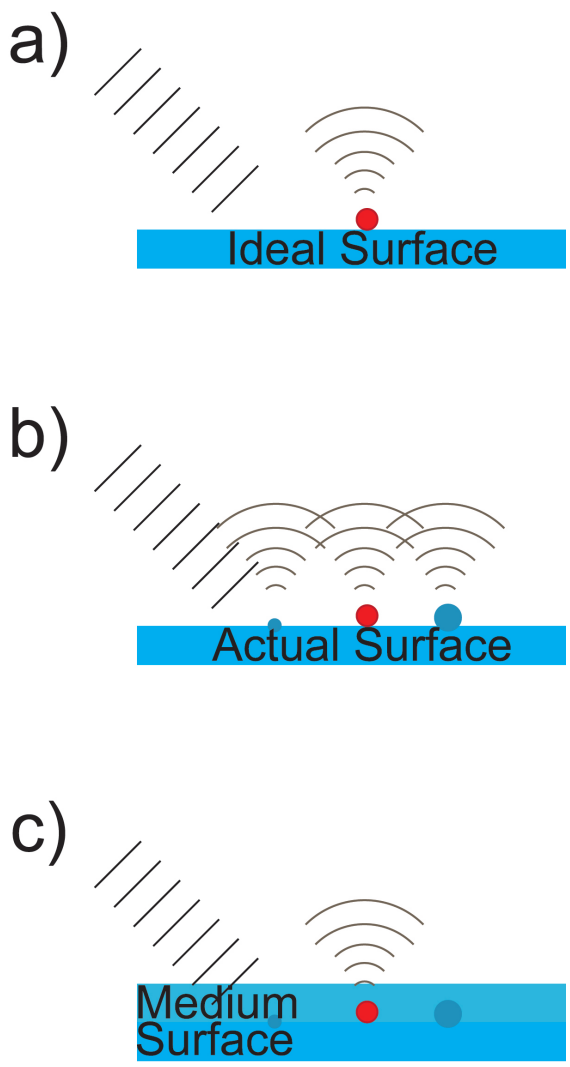

Figure 4.2: **Ideal Surface vs. Actual Surface** - Light (indicated by wavefront) is scattered by a SWNT and defects on various surface conditions. a) An ideal surface with perfect flatness. b) Actual surface with roughness. c) Actual surface with refractive index matched medium. The red dot represents the SWNT and dark blue dots represent the surface roughness and defects.

an index-matching medium of glycerol, which has a refractive index 1.47 (Fisher Scientific), similar to that of quartz (refractive index 1.54, Corning No. 1) (figure 4.3). This matching between the glycerol and quartz creates an optically invisible substrate. Due to total internal reflection, at the uppermost interface of air and coverslip, the excitation laser is completely reflected, which prevents it from entering the detection optics. A charge-coupled device (CCD) camera (Sesicam QE, Cooke Imaging) and a high numerical aperture (N.A.) objective lens (Olympus 40 ×) were used to detect the scattered photons from individual SWNTs, which are resting on the substrate. The substrate is illuminated under wide-field geometry (collimated light beam with large beam width). By using a double monochromator (Princeton Instruments) and a supercontinuum laser (Fianium), the excitation wavelength λ of the laser was scanned from 450 to 850 nm with a spectral bandwidth of 20 nm, while the laser's polarization was parallel to the SWNTs [100].

4.2.3 Rayleigh Spectra and Chirality Identification

Since the illumination is wide-field, we obtain the Rayleigh spectra for each pixel of the illumination area ($\approx 70 \times 80 \mu m^2$) from a single measurement run. First, by comparing darkfield images with and without a matching bandpass filter (bandwidth <10 nm) in the detection pathway, we reject photons from Raman scattering and PL and confirm that the vast majority of the detected photons are due to Rayleigh scattering. Second, a spatial map of resonance parameters for each SWNT, including the resonance wavelength (λ_{peak}), intensity, and peak width are recorded to generate Rayleigh spectra for different SWNTs (figure 4.5). A typical data set contains 200 frames (15 s integration time per

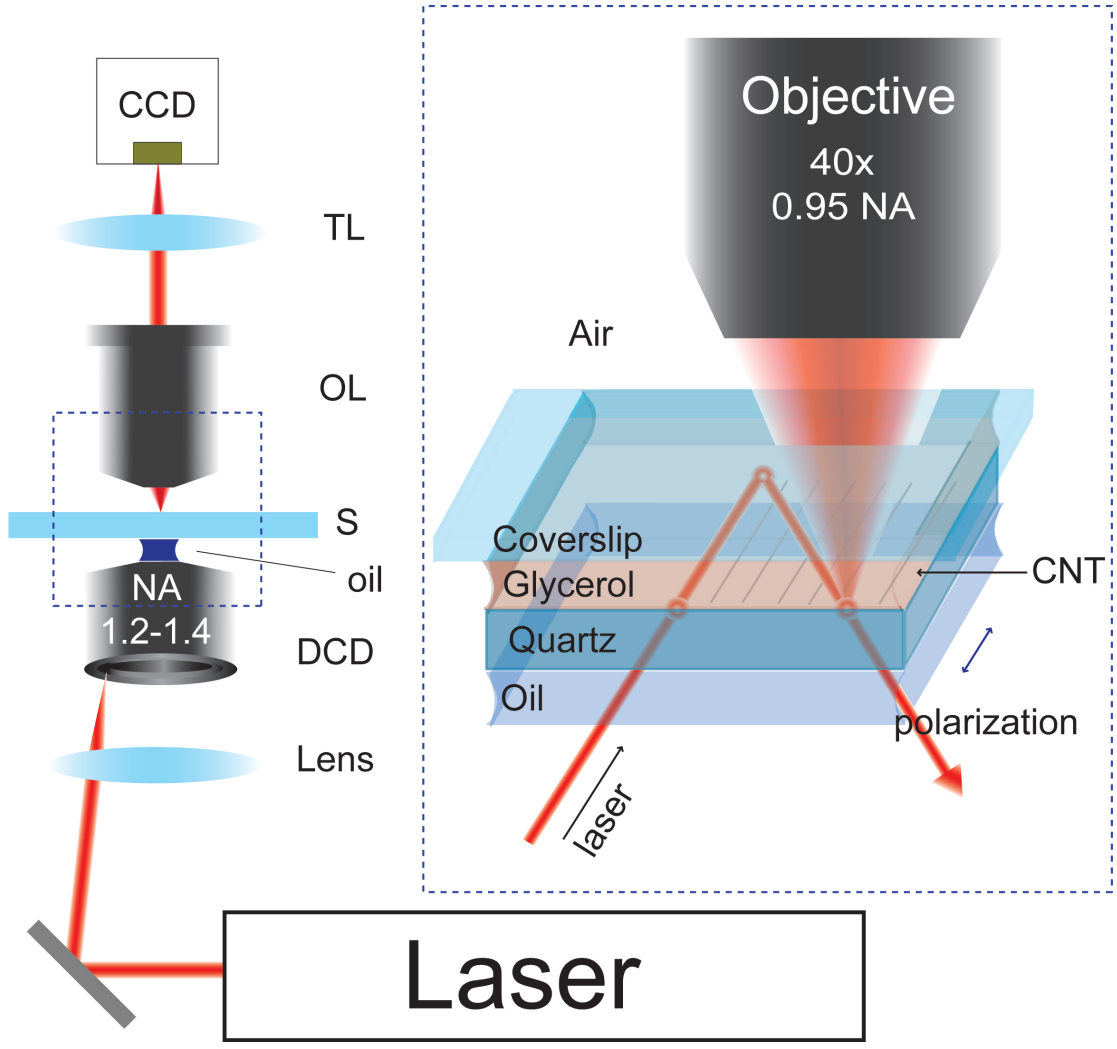

Figure 4.3: **On-Chip Rayleigh Experimental Setup** - Schematic of the optical setup. The incident laser light is introduced at an angle, travels through a set of index-matched media, and is reflected completely at the uppermost interface with a lower refractive index medium (air)

frame for CCD camera) measured at different λ in the same illuminated area. Due to the resonances, different SWNTs will "blink" in different frames, allowing us to assign distinct colors (resonant wavelengths) to different SWNTs in a wide-field image, and to obtain diffraction-limited spatial resolution to locate the SWNTs (figure 4.4).

Recording the Rayleigh spectra is followed by chirality identification (figure

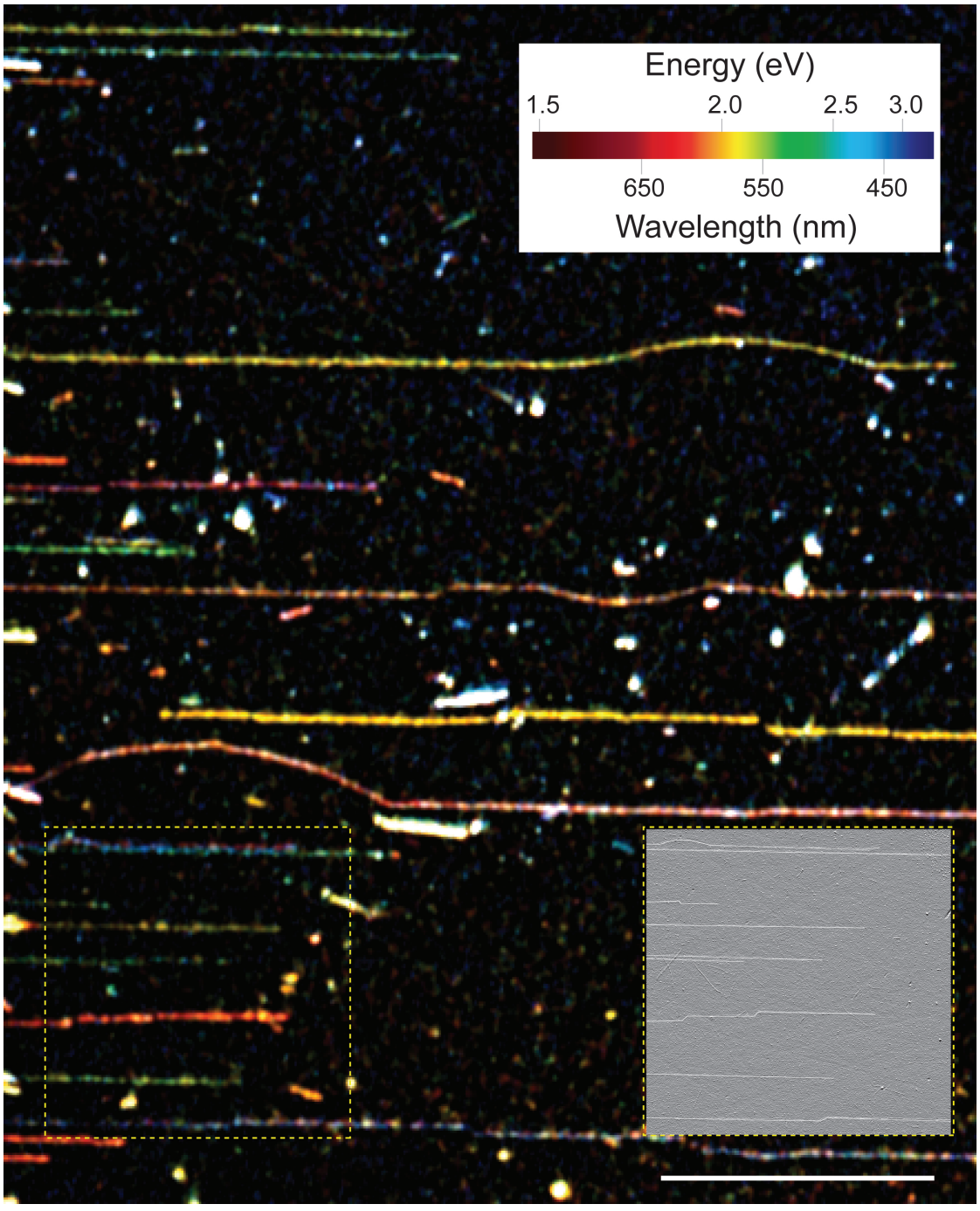

Figure 4.4: **Position of SWNTs** - Representative spatial Rayleigh image shows more than 20 SWNTs (in false color corresponding to λ_{peak}). Scale bar, 20 μm. Inset: SEM image of a typical sample in a dense area. Scale bar, 10 μm.

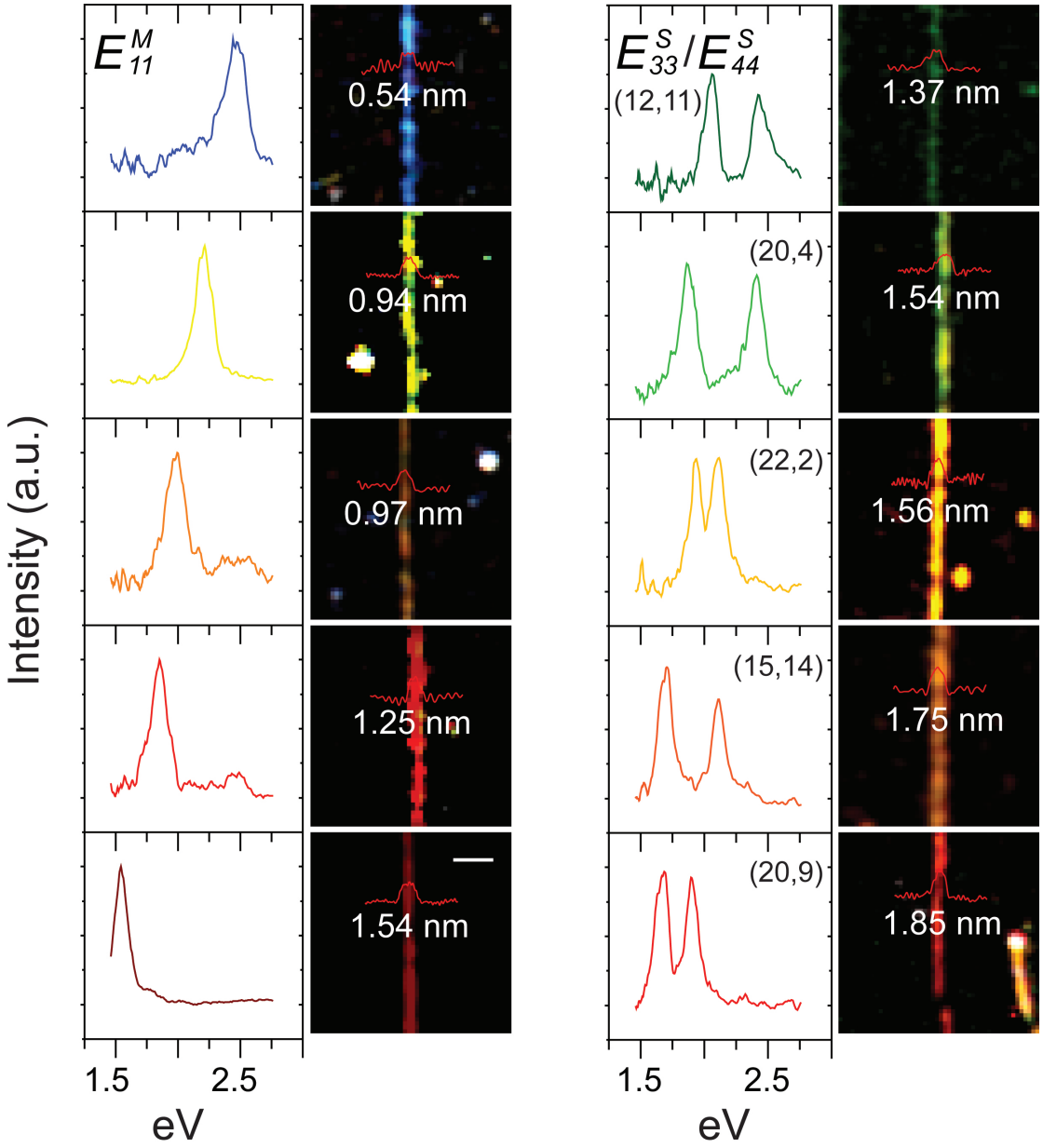

Figure 4.5: **Representative Chirality Resolved SWNTs** - Color Rayleigh images of metallic (left) and semiconducting (right) SWNTs, along with their corresponding optical spectra and AFM height traces (shown in red).

4.5 right panel). To clean the sample, we immerse it in hexane for 12 hours, and then methanol for 12 hours. Next, annealing the sample at $500^{\circ}C$ in H_2 and Ar gas for half hour is followed by AFM measurement for each SWNTs. This allows us to confirm that all of the SWNTs are visible in our Rayleigh image. Comparing the diameters to the resonances allows us to deduce the chiral indices (n, m). First, we measured interband optical transition energies (E_{ii}^{exp}) and AFM measured diameters (d_{AFM}) for 10 different SWNTs having double peaks in their Rayleigh spectra (table 4.1).

(n, m)	d_{AFM}	$\theta(^{\circ})$	d_{NT}	transition	E_{ii}^{exp} (eV)	E_{ii}^{calc} (eV)
(12, 11)	1.37	28.6	1.58	E_{33}^{S}	2.44	2.06
				E_{44}^{S}	2.50	2.56
(20, 4)	1.54	8.9	1.77	E_{33}^{S}	1.87	1.78
				E_{44}^{S}	2.41	2.47
(22, 2)	1.56	4.3	1.83	E_{33}^{S}	1.93	1.91
				E_{44}^{S}	2.10	2.12
(15, 14)	1.75	28.9	1.99	E_{33}^{S}	1.70	1.65
				E_{44}^{S}	2.11	2.06
(20, 9)	1.85	17.7	2.04	E_{33}^{S}	1.67	1.66
				E_{44}^{S}	1.91	1.94
(16, 15)	1.89	28.9	2.13	E_{33}^{S}	1.52	1.54
				E_{44}^{S}	1.92	1.93
(13, 1)	0.84	3.7	1.07	$E_{11}^{M}(-)$	2.08	2.16
				$E_{11}^{M}(+)$	2.39	2.46
(15, 0)	0.94	0	1.19	$E_{11}^{M}(-)$	1.90	1.96
				$E_{11}^{M}(+)$	2.15	2.22
(23, 5)	1.83	9.6	2.05	$E_{11}^{M}(-)$	2.23	2.26
				$E_{11}^{M}(+)$	2.52	2.55
(25, 10)	2.27	16.1	2.48	$E_{11}^{M}(-)$	1.88	1.92
				$E_{11}^{M}(+)$	1.99	2.06

Table 4.1: Physical and Spectroscopic Data for Several SWNTs from AFM and Rayleigh Scattering Measurements. The calculated optical transitions E_{ii}^{calc}, diameters d_{NT}, and chiral angle θ are also provided.

With the measured interband optical transition energies and AFM measurements, we compare our values to the reported chiral resolve PL data [101], which already contains excitonic effect. We then calculate the interband tran-

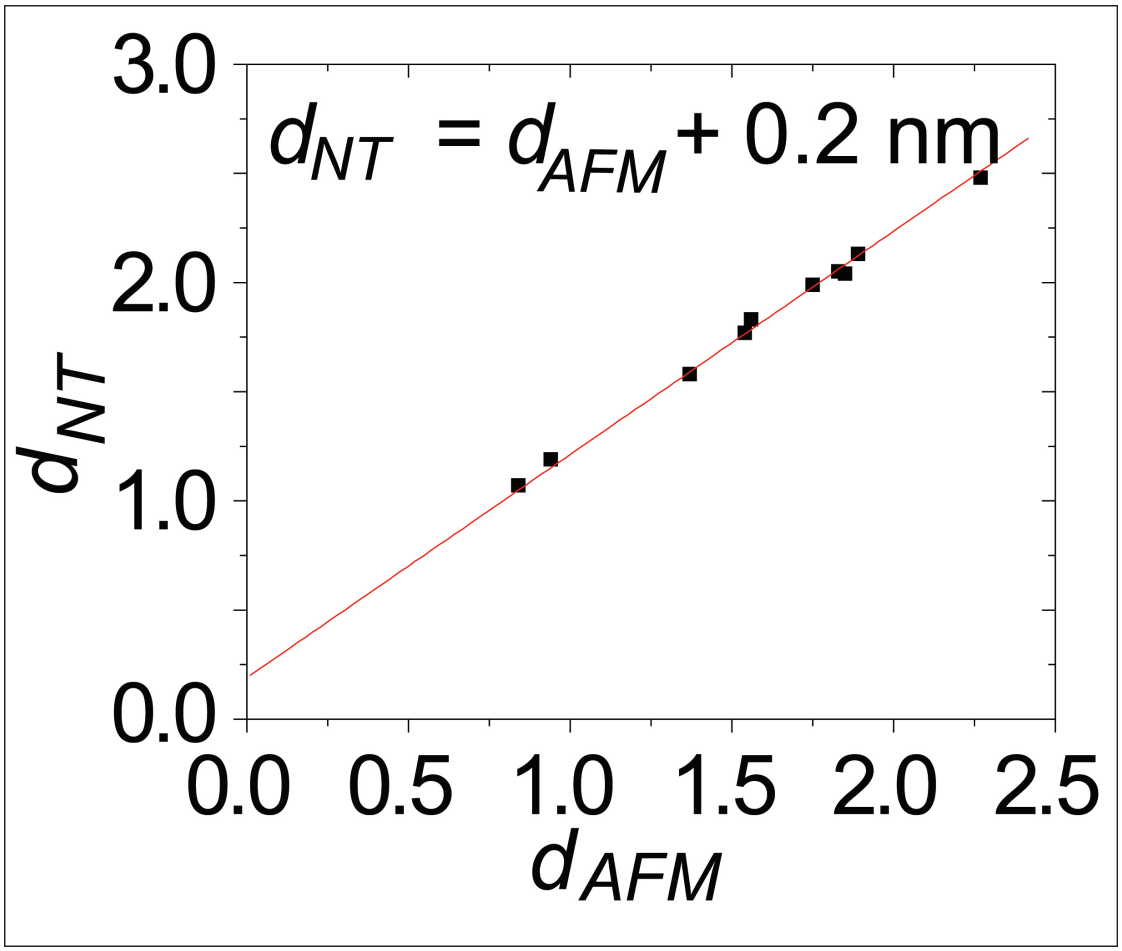

Figure 4.6: **AFM Height Calibration** - Calibration using the calculated diameters and AFM measured diameters of 10 SWNTs

sitioin energies (E_{ii}^{calc}) and the true tube diameter (d_{NT}) for SWNTs having values that are closest to the our experimental values. We obtain an offset of 0.2 nm (best fit), $d_{NT} = d_{AFM} + 0.2nm$, which effectively accounts for the assorted van der Waals interactions during AFM measurement (figure 4.6). The spectra and calibrated AFM heights allow us to construct an experimental Kataura plot from individual tube measurements as shown in figure 4.7. Eighty pristine SWNTs' interband transitions were assigned. E_{ii}^{S} is denoted for semiconducting and E_{ii}^{M} is denoted for metallic SWNTs. The electronic-type assignments for SWNTs are confirmed using resonant micro-Raman spectroscopy (figure 4.8, ex-

citation wavelength 633 nm), which show that the metallic SWNTs assigned by our method indeed have Fano lineshape, and the semiconducting SWNTs have Lorentzian lineshape [40]. Also we use RRS to measure an individual SWNT's radial breathing mode to further confirm our AFM calibration. This SWNT's Rayleigh spectrum has two peaks centered at 1.87 and 2.56 eV with its AFM height measured to be $d_{AFM} = 1.51nm (d_{exp} = 1.71nm)$. The structural assignment, (17, 7), is made to this nanotube with $d_{NT} = 1.72nm$, which makes it a semiconducting nanotube (figure 4.7). The Lorentzian line shape of its Raman G-band (figure 4.8 upper right) confirms its semiconducting behavior, and the frequency of its radial breathing mode $\omega_{RBM} = 144cm^{-1}$ corresponds to a SWNT diameter $d_{RBM} = 1.72nm$ (estimated from $d_{RBM} = 248cm^{-1}/\omega_{RBM}$) [40].

4.2.4 Observation of Heterojunctions for SWNTs

An immediate application of wide-field on-chip Rayleigh microscopy is identifying and locating sudden changes in the optical spectra along the length of individual SWNTs. While most SWNTs exhibit uniform Rayleigh spectra throughout their entire length, we also observe some nanotubes that exhibit abrupt changes in their spectra. The Rayleigh image in figure 4.9a contains a nanotube that exhibits a noticeable color change along its length in the region outlined in red. We show the Rayleigh spectrum of the junction along the SWNT axis in figure 4.9b together with its matching color image in figure 4.9c. The spectral change occurs abruptly, and the corresponding AFM data (figure 4.9d) shows that d_{AFM} is slightly different before and after the junction. Optical and AFM measurements imply that this tube forms a metal-metal junction from (23, 5) and (25, 10) nanotubes, with the optical resonances corresponding to E_{22}^{M} transi-

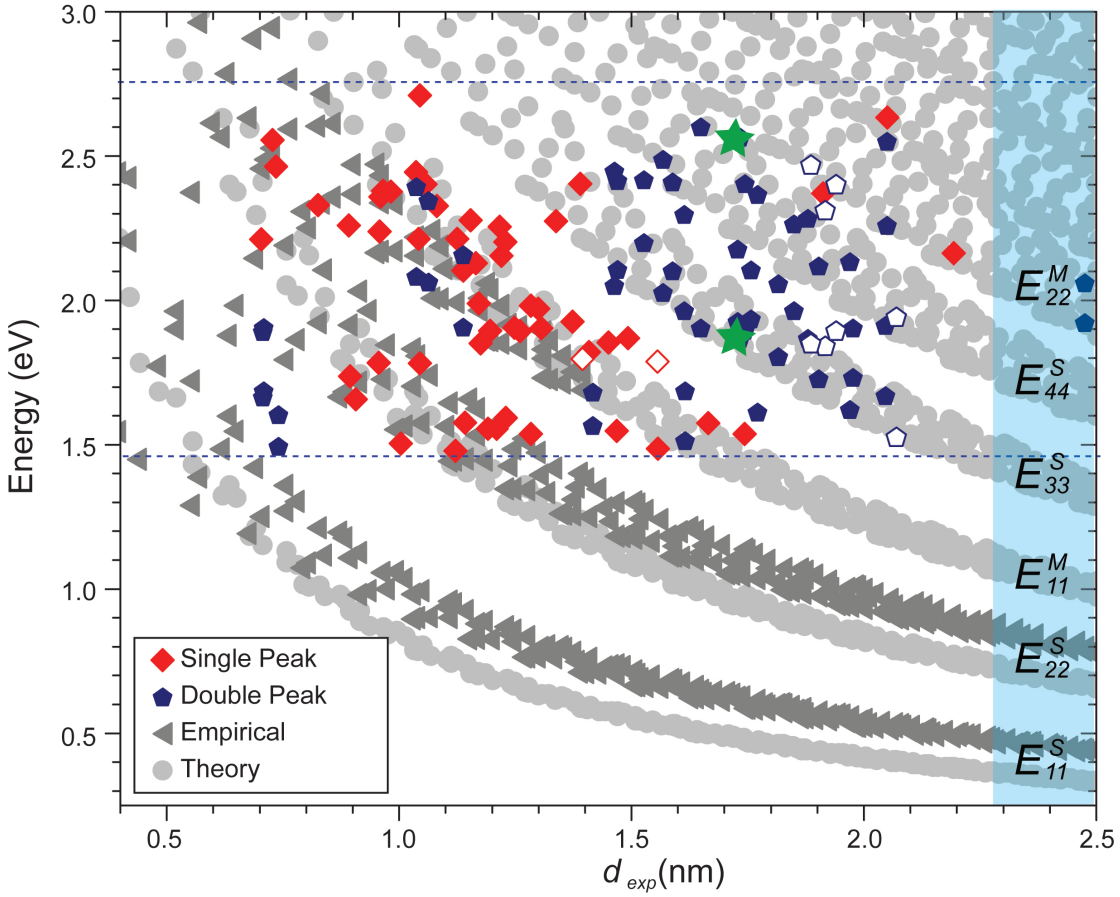

Figure 4.7: **Experimental Kataura Plot** - SWNTs exhibiting either one peak (red) or two peaks (blue) from their Rayleigh spectra within our excitation energy range (blue dashed lines) are plotted using d_{exp} for the diameter axis ($d_{NT} = d_{AFM} + 0.2nm$). Theoretical tight-binding (light gray circles with γ_o = 2.9 eV) and published empirical data (dark gray triangles) are provided for comparison. Resonant Raman spectroscopy was performed on several individual SWNTs which is indicated by hollow data points

tions. (The observed splitting in their Rayleigh spectra is attributed to trigonal warping.) We observed S-M and S-S heterojunctions (figure 4.9e and 4.9f) as well. Although Rayleigh measurements were used to identify similar chirality changing events previously [102], the current technique enables us to determine the precise position of these events along with the AFM heights before and after the transition. We find that all chirality-changing events are spatially abrupt, and the transition of the Rayleigh spectra occurs within the length of one pixel

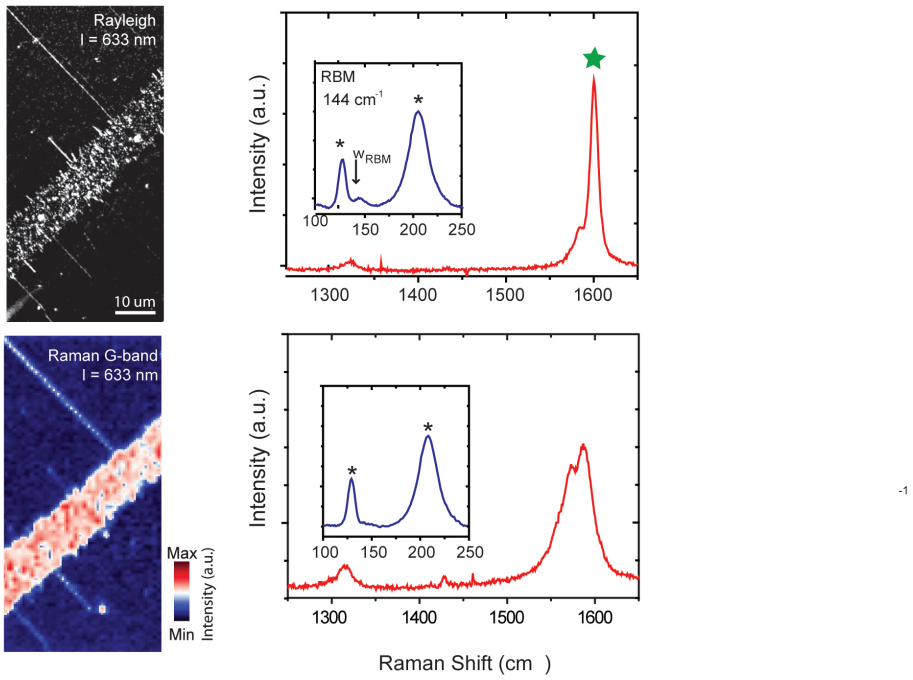

Figure 4.8: **Micro Raman and Rayleigh Comparison** - On-chip Rayleigh imaging of SWNTs at 633 nm (upper left) and micro Raman imaging at 633 nm (lower left). Upper right panel: Representative Raman spectrum (excitation wavelength 633 nm) for the semiconducting (17,7) SWNT is labeled as green stars on the experimental Kataura plot (figure 4.7). Quartz Raman peaks are indicated by black asterisks. Lower right: Representative Raman spectrum for a metallic SWNT.

of our CCD camera, which corresponds to approximately 150 nm (figure 4.9b and 4.9c). We can identify almost all events that occur among the many SWNTs that we analyzed on our sample. Based on our measurements of more than 200 SWNTs, we conclude that the frequency of chirality-changing events for this particular growth procedure is approximately 3%. This technique should be useful for correlating the density of chirality-changing defects in SWNTs, produced using different growth conditions.

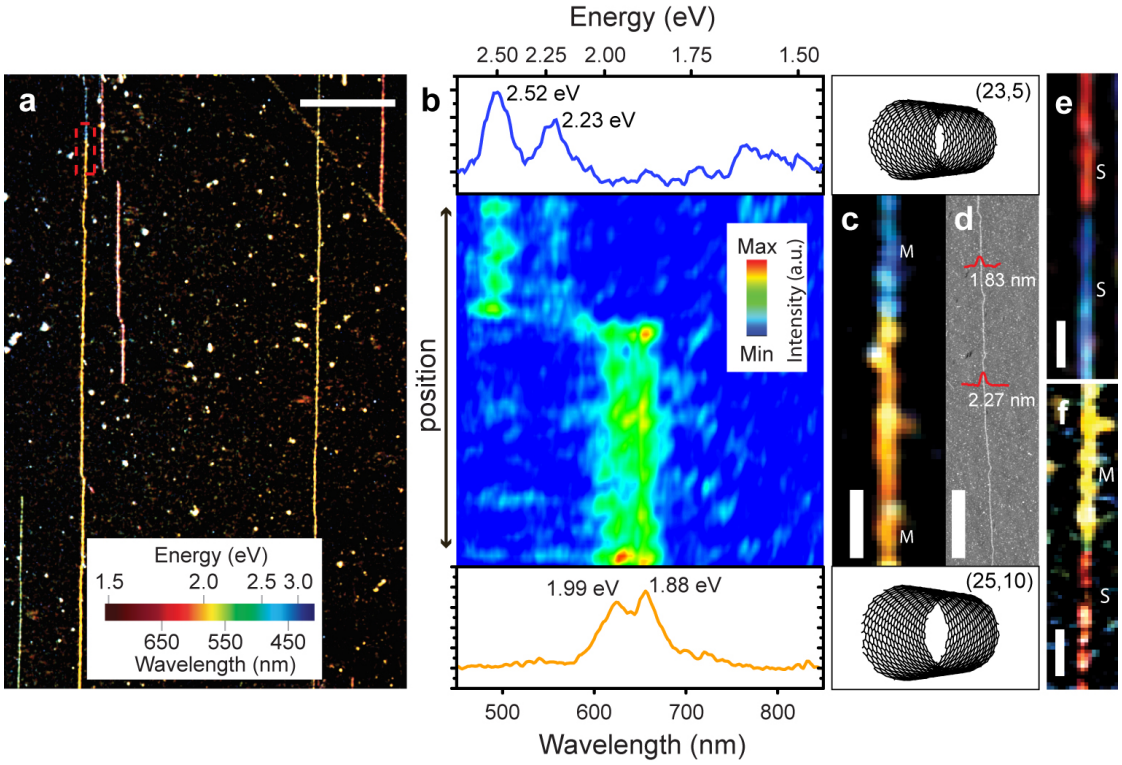

Figure 4.9: **SWNT Heterojunctions** - (a) Large spatial map of SWNT resonances in false color corresponding to λ_{peak}. In the region outlined in red, a SWNT exhibits a distinct color change. Scale bar, 20 μm. (b) Rayleigh spectrum along the SWNT axis for the region is outlined in red in (a). The observed resonances correspond to E_{22}^{M} transitions for (23, 5) and (25, 10) SWNTs. (c,d) Close-up color image (c) of the outlined region in (a) and the corresponding AFM image (d). Scale bars, 2 μm. (e,f) Examples of semiconductor-semiconductor (e) and metal-semiconductor (f) heterojunctions. Scale bars, 2 μm.

CHAPTER 5

EXCITONIC OPTICAL WIRES

In this chapter, first we discuss the spatial distribution of the radiation scattered by SWNTs. We use modified Rayleigh platform to measure the spatial distribution and spectra of the radiation scattered by individual continuous SWNTs and patterend SWNTs. We observed the intrinsic scattering spectra of the SWNTs are determined by their chiral index, yet the scattering patterns are controlled by their shapes and geometric configuration. Second, we observe uniform optical conductivity on resonance as we quantitatively measured the scattering intensity and spectra of the SWNTs. The origin of the uniform optical conductivity is described. Lastly, a long-range optical coupling between SWNTs is discussed. A qualitative model of this long-range optical coupling is also given.

5.1 Rayleigh Scattering Direction in SWNTs

The light scatterd from SWNTs resembles the radiation pattern of long thin wires in classical radiation theory [103]. On the other hand, SWNTs display sharp optical resonances in which the resonant frequency scattering and absorption strength is controlled by the nanostructure, in particular the chiral index.

5.1.1 Fraunhofer Imaging

The Rayleigh imaging platform mentioned previously allows us to investigate the elastic scattering from nanotubes placed directly on a solid transparent sub-

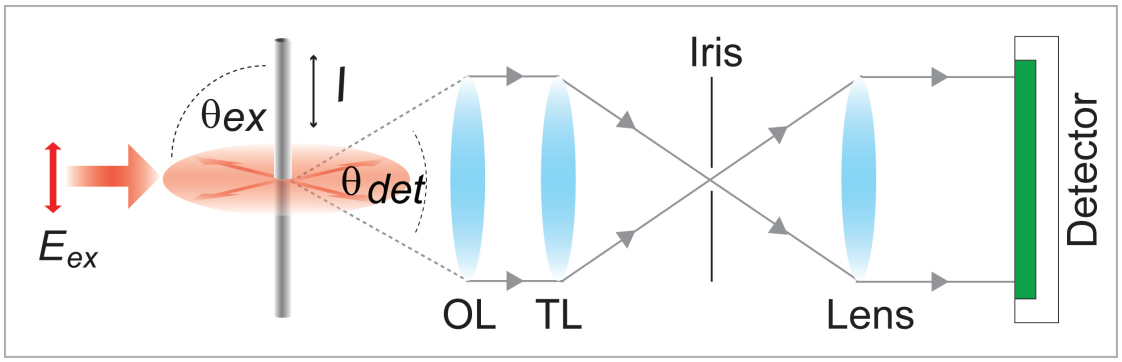

Figure 5.1: **Fraunhofer Imaging** - The scattered light is projected onto the objective lens (OL). An iris is placed at the image forming plane of the tube lens (TL) to observe only one SWNT at a time, and then an additional lens is used to collect the spatial distribution of scattered light from the same SWNT, which is imaged using a CCD camera

strate. Although several classical antenna-like optical properties of carbon nanotubes were described in earlier theoretical studies and experiments [103–110] , a direct measurement of the spatial pattern for optical fields scattered by individual nanotubes has not yet been reported. To measure the spatial distribution of scattered light, we utilize Fraunhofer imaging, as shown in figure 5.1. By using an iris, we can choose to detect the Rayleigh scattering signal from only one SWNT, which projects onto the object lens. All points on the focusing plane of the objective lens are in one-to-one relation with any points on the plane of the iris. The iris allows us to choose particular sets of points that are corresponding to the points on the focusing plane. Thus we can measure single SWNT's scattering signal using this scheme. The CCD camera captures the image corresponding to scattering signal projecting on the objective lens.

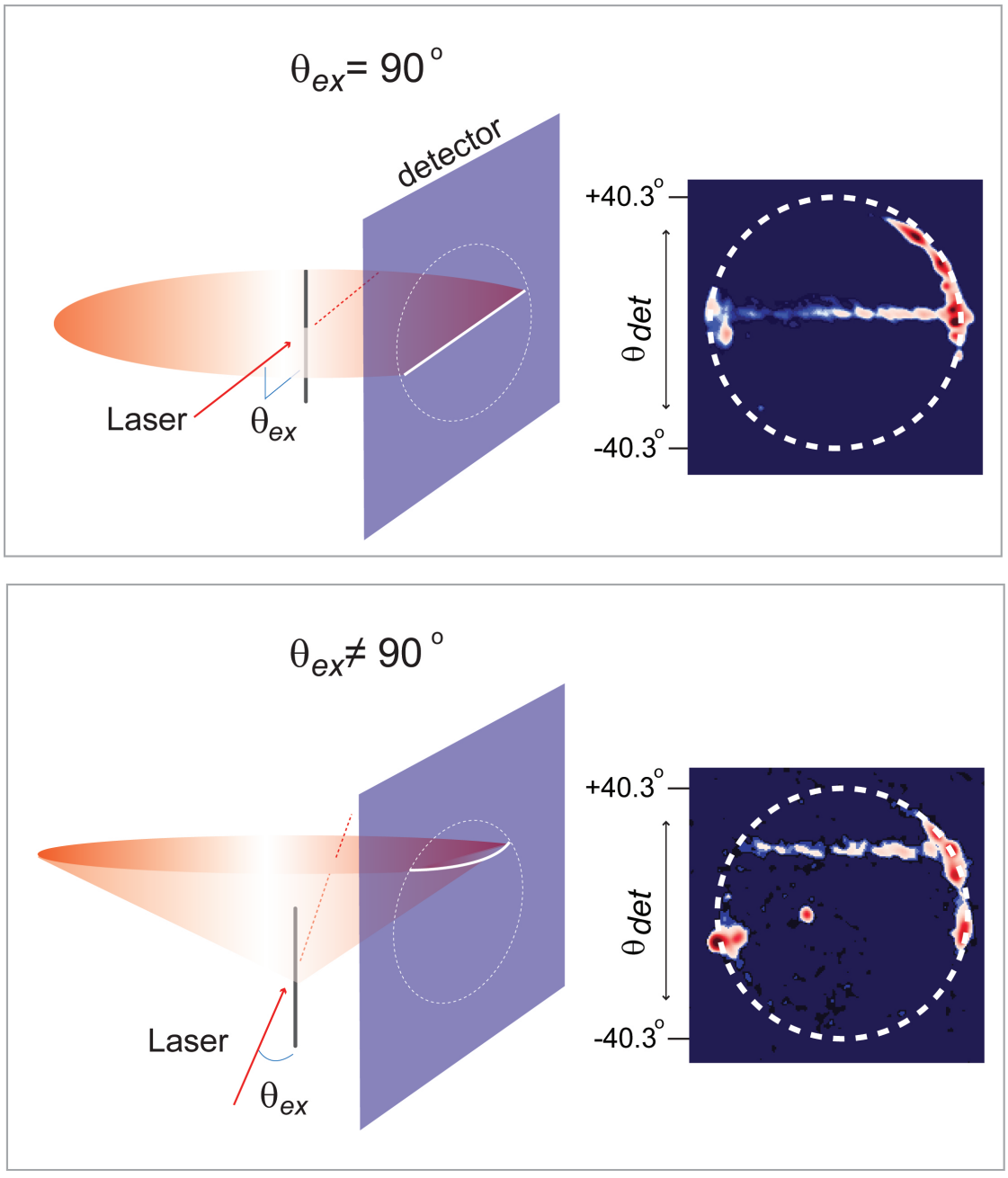

Figure 5.2: **Radiation Behavior for Nanotubes** - Radiation patterns from Fraunhofer imaging of individual nanotubes when $\theta_{ex} = 90°$ (upper panel) and when $\theta_{ex} \neq 90°$ (lower panel)

5.1.2 Scattering Direction

The observed propagation pattern of scattered light from individual SWNTs is described by classical scattering theory and radiation theory, which yield the same prediction, when $l_{NT} \gg \lambda \gg d_{NT}$, where l_{NT} is the nanotube length. In this regime, a nanotube behaves as a long radiating wire with a surface current

$$I(z, \omega) = \pi d_{NT} \sigma(\omega) E(z, \omega) \tag{5.1}$$

excited by a plane wave incident at angle θ_{ex} with respect the the nanotube axis, where $E(z, \omega)$ is the electric field of the plane wave along the nanotube axis. When $\theta_{ex} = 90°$, the scattered field is predicted by classical scattering theory to become focused onto a rotationally symmetric disk perpendicular to the tube axis. This is experimentally confirmed in our measurement (figure 5.2 upper panel). In contrast, if $\theta_{ex} \neq 90°$, the scattered radiation is focused onto a rotationally symmetric cone having the same direction as the excitation laser (figure 5.2 lower panel).

Polarization dependence in the scattered light internsity was also measrured by changing the polarization angles between a pair of polarizer installed before and after the sample. This is consistent with previous optical studies on SWNTs [43].

5.1.3 Spectral Profile and Scattering Pattern

It is possible to control the spectral profile and scattering pattern independently, as the scattered radiation is determined by the macroscopic shape, and scattering spectra and intensity are determined at the molecular level. We first pattern

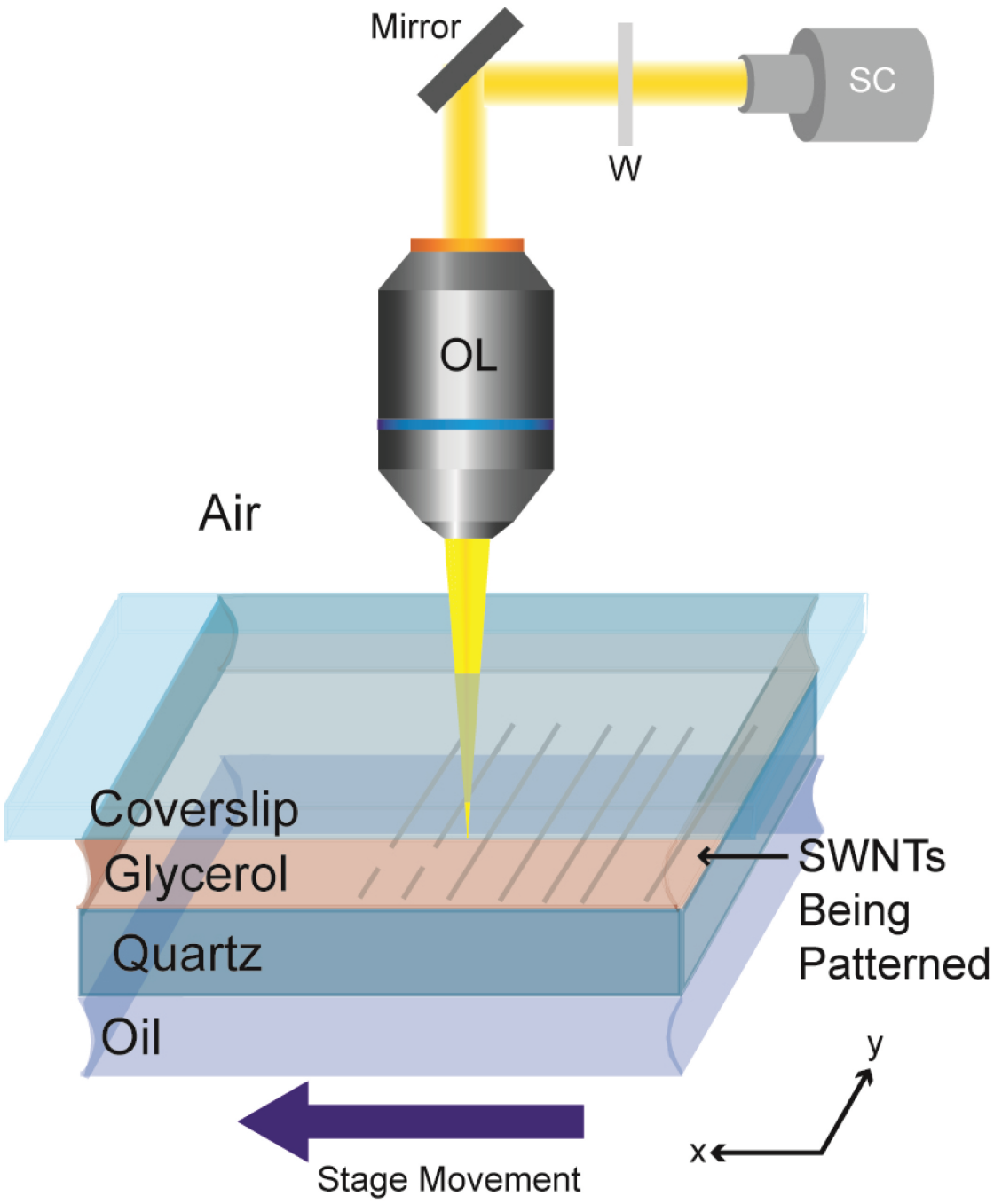

Figure 5.3: **Patterning the SWNTs into Segments** - High-intensity supercontuum light was focused on the sample plane. The stage was raster-scanned in the x-y plane to pattern the tubes into periodic segments

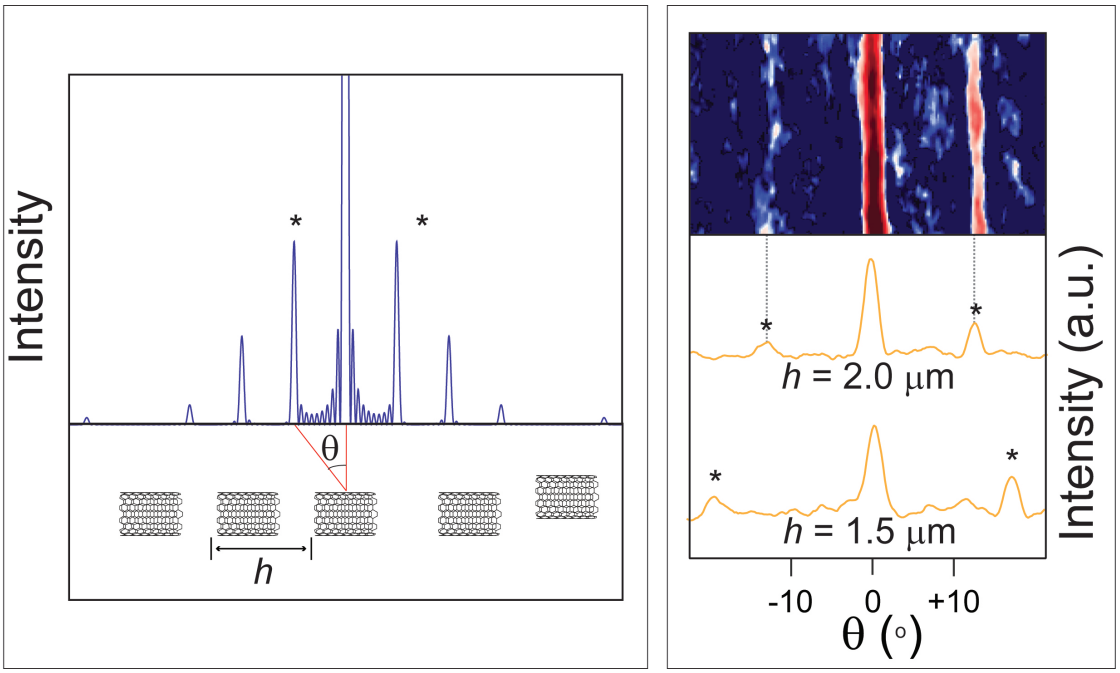

Figure 5.4: **Scattering Pattern for SWNT Segments** - Left panel: schematic illustrating the scattering pattern for periodically spaced (h = pitch distance) linear structures. Right upper panel: Fraunhofer image for a nanotube with h = 2.0 μm after cutting. Right lower panel: Measured scattering patterns for nanotubes with different pitch sizes after cutting. Asterisks denote side bands depicted in the left panel.

individual nanotubes into shorter periodic segments with well-defined separation distances (h) by cutting them using a high-intensity supercontinuum laser beam (NKT Photonics, Koheras SuperK Compact). After passing through a wideband hot mirror (W) to filter out the infrared wevelength, the laser beam is focused onto the sample plane (glycerol-quartz interface). The peak laser pulse power after the hot mirror is about 420 W. The sample is mounted on a stage equipped with mechanical motor. Lastly, by moving the stage, we obtain a rastering scanning scheme, so that the focused laser can cut the SWNTs into segments (figure 5.3)

Using the Fraunhofer imaging, the spatial distribution of the light scattered by these patterned nanotubes shows additional side peaks (cones denoted by

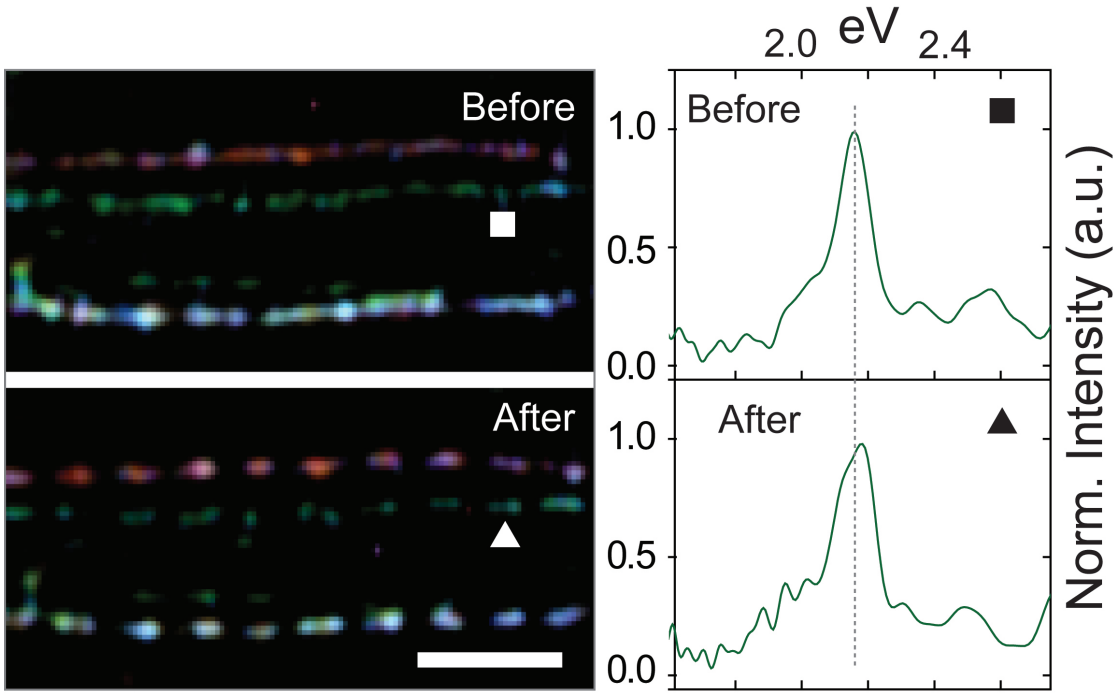

Figure 5.5: **Comparison Between Before and After Laser Cutting** - Left panel: color Rayleigh image before (upper panel) and after (lower panel) cutting. Scale bar, 5 μ m. Right panel: Rayleigh spectra (normalized to the peak) before and after patterning for the nanotube marked by the symbols in the left panel.

asterisks) in addition to the central peak (disk), resembling the interference patterns of classical diffraction gratings or multiple-slit apertures (figure 5.4).

We compare the Rayleigh spectra before and after laser patterning. The spectra show that the nanotubes maintain their spectral profiles even after being cut into small periodic segments (figure 5.5). To compare the spectra before and after cutting, we normalized the spectra to the maximum values. As shown on the right of figure 5.5, we see the peak of the spectra's resonant peak remain the same.

This gratings pattern scheme demonstrates that independly controlling the scattering direction and scattering spectra of SWNTs is possible.

5.2 Uniform Optical Conductivity on Resonance

The resonant frequency scattering and absorption strength of SWNTs are controlled by the chiral index (*m*,*n*). These properties are quantum-mechanical in nature and determined by the exciton dynamics through a single parameter, the complex optical conductivity $\sigma(\omega)$ (see Appendix about optical conducvitity). The imaginary part of the optical conductivity corresponding to the reflctivity of the material, whereas the real part of the optical conductivity determines the absorptance of light. In this section, by using wide-field on-chip Rayleigh measurement platform, we measure the absolute scattering intensity, resonance wavelength from spectra, and diameter of the SWNT, we determine the complex optical conductivity of SWNTs on resonance, which is explained by the exciton relaxation mechanisms in SWNTs.

5.2.1 Scattering Cross Section Width of SWNTs on Resonance

The scattering cross section width of an individual SWNT was measured by first identifying its resonance wavelength from its Rayleigh spectrum. In our setup, the light scattered by a SWNT is detected with a detection angle (θ_{det}) of 80.6^o out of 360^o. Thus, the total scattering detection efficiency in our setup is given by $(80.6/360) \times T_{OE}(\lambda) \times QE_{CCE}(\lambda)$, where T_{QE} is the combined transmission efficiency of all optical elements and QE_{CCD} the quantum efficiency of the CCD, both measured at the resonance wavelength, λ. This allows us to extract the number of photons, n_L, being scattered by the SWNT per unit length along the SWNT's axis per second($\frac{number of photon}{\mu m \cdot s}$). Second, by putting lens oil and a prism at the top of the coverslip to destroy the total internal reflection, we directly

measured the power of the illumination at the resonance wavelength. From the Rayleigh image at that resonance wavelength, we obtain the Gaussian profile of the illumination beam profile and extract the number of photons, n_A, illuminating per unit area per second ($\frac{number of photon}{\mu m^2 \cdot s}$) at the SWNT. The ratio, $\frac{n_A}{n_L}$, gives the scattering cross section width (δ_{scatt}) of an individual SWNT (see Appendix for Mathematic codes). The scattering cross section width, δ_{scatt}, has unit of m, which is different from that of in equation 3.2.

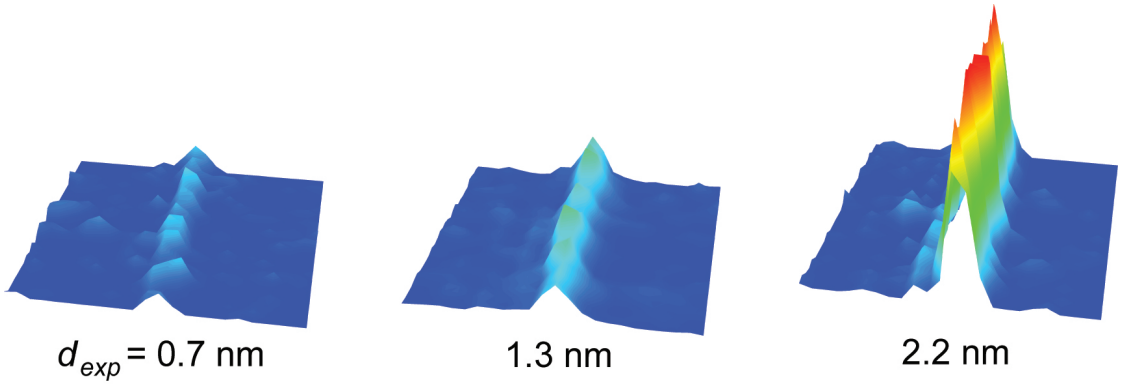

Figure 5.6: **Spatial Profile of Scattering Intensity vs. Different Tube Diameters** - On resonance, the scattering intensity for each tube is normalized corresponding to its maximum. The scattering intensity is calibrated to the instruments sensetivity and the diameter is experimentally measured by calibrated AFM measurement.

In general, we obsever that δ_{scatt} on resonance ranges from 0.2 pm to 2.3 pm. By comparing with the diameters measured by AFM, we see that the absolute scattering intensity, in other words, the scattering cross section width, increases nonlinearly with diameters, d_{NT}. In fact, measurements from 19 different nanotubes on resonance shows that all data points follow the scaling behavior of $\delta_{scatt} \propto d_{NT}^2/\lambda$ (figure 5.6).

5.2.2 Optical Conductivity on Resonance

From the scattering cross section width measurement, we obtain the optical conductivity of SWNTs. We first model an individual SWNT as an infinite straight pipe. For an infinite straight pipe, the total radiated power per unit length (P_{rad}) averaged over time is given by

$$P_{rad} = \frac{1}{8} Zk|I(\omega)|^2, \tag{5.2}$$

where $I(\omega)$ is the surface current in equation 5.1 ([111]) and Z is the impedance of the medium (380Ω for glycerol/quartz in our experiment). Furthermore, if the incident beam has an electric field $E(\omega) = |E_o|e^{-i\omega t}$, the total scattered light power is

$$P_{scatt} = \frac{1}{2} \delta_{scatt} |E_o|^2 Z^{-1}. \tag{5.3}$$

Equating the two expressions for the power yield

$$\delta_{scatt} = \frac{1}{2} \pi^3 Z^2 |\sigma(\omega)|^2 d_{NT}^2 \lambda^{-1}. \tag{5.4}$$

Equation 5.4 establishes the relation between δ_{scatt} and $|\sigma(\omega)|$. And it indeed shows the behavior we observe in figure 5.6. By comparing the diameters, scattering cross section, and resonant wavelength, we can obtain each SWNT's absolute value of optical conductivity. This is discussed in the next section.

5.2.3 Uniform Peak Optical Conductivity

As mention in the previous section, we could obtain the absolute value of optical conductivity for each SWNT. We first analyze 19 nanotube resonances of

various sub-band transitions measured from SWNTs shown in figure 4.4. Comparing $\sqrt{\delta_{scatt}\lambda}$ and diameters of the SWNTs measured in our experiment (d_{exp}), we observe the linear behavior as shown in equation 5.4 (figure 5.7).

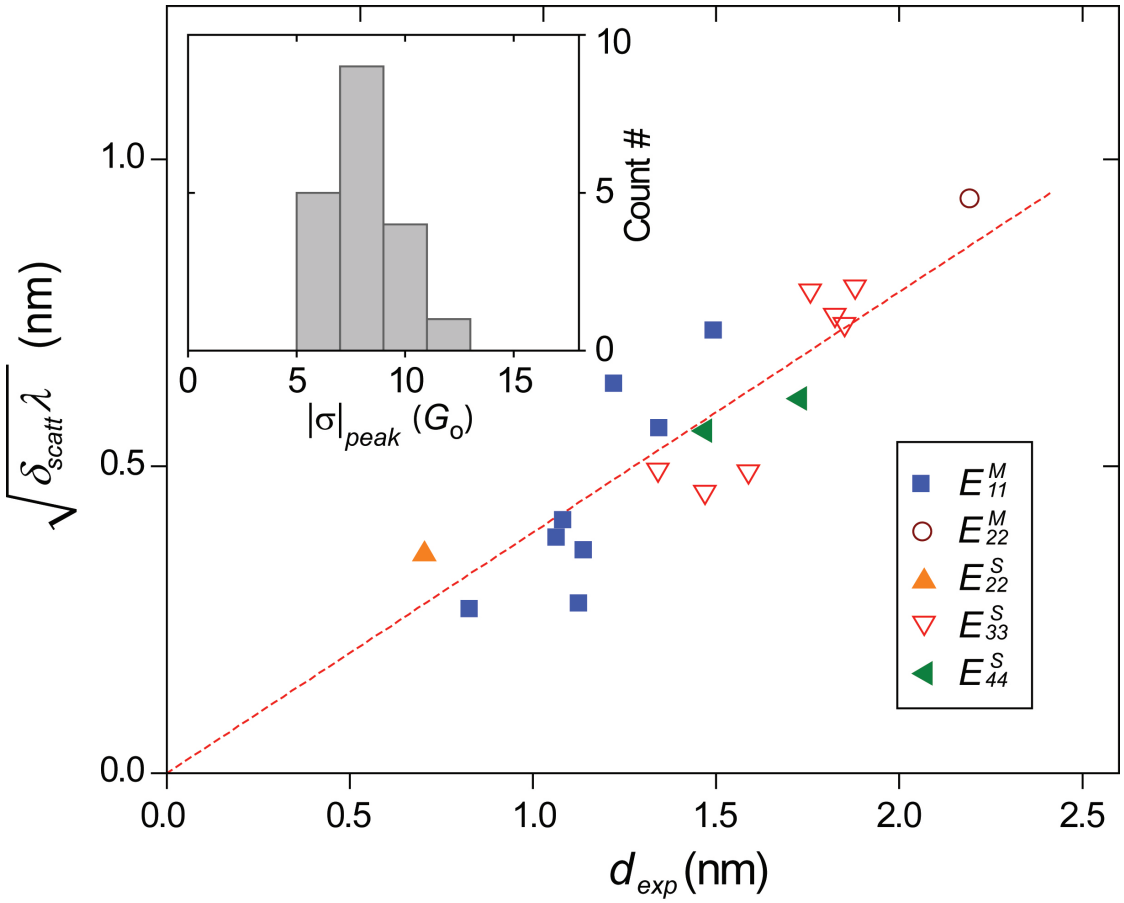

Figure 5.7: **Optical Conductivity of SWNTs and Scattering Cross Section Width** - $\sqrt{\delta_{scatt}\lambda}$ as a function of d_{exp} measured for 19 nanotube resonances of various sub-band transitions. Inset: Histogram of peak dynamic conductivity $|\sigma|_{peak}$ in units of $G_o(e^2/h)$.

The extracted $|\sigma|_{peak}$ for all 19 nanotube resonances in our sample shows a narrow distribution: $|\sigma|_{peak} = (8.3 \pm 1.5)G_o$, where $G_o = e^2/h$ is the natural unit for sheet conductivity and is also well-known as the d.c. conductance quantum of one-dimensional wires. This behavior is a suprising result, contrary to what one might expect due to the heterogenity of SWNTs. Although different SWNTs have different electronic structures, the behavior of the optical conductivity in

SWNTs points to a universal phenomenon.

5.2.4 Origin of Uniform Peak Optical Conductivity in SWNTs

The uniform optical conductivity indicates that this phenomenon is independent from the chirality, density of states, and diameters of the SWNTs. From Kubo formular, the linear response theory allows the conductivity to be expressed as:

$$\sigma(\omega) = \frac{\hbar}{i2\pi RL} \sum_{\alpha} \cdot \frac{|\langle\alpha|\,\mathbf{J}\,|\Omega\rangle|^2}{E_\alpha} \frac{2\hbar\omega}{E_\alpha^2 - (\hbar\omega + i\hbar\gamma_\alpha)^2}, \tag{5.5}$$

where $|\Omega\rangle$ and $|\alpha\rangle$ indicate the ground and excited states of the exciton, with respectively, E_α is the energy of the excitation, γ_α is the width of the excitation, R is the nanotube radius, L is the length of the tube, and ω is the frequency of the laser. Assuming that the excitation is concentrated in a single transition [90, 112, 113]. Equation 5.5 can be further simplified as

$$\sigma(\omega) = \frac{e^2}{h} \cdot \frac{1}{w\pi i} \cdot \frac{2\hbar\omega E_o}{E_\alpha^2 - (\hbar\omega + i\hbar\gamma_\alpha)^2}, \tag{5.6}$$

where E_o corresponds to the natural energy scale of the SWNT, defined as $E_o = \hbar v_F/R$, where v_F is the Fermi velocity [114]. On resonance, $E_\alpha = \hbar\omega$, the peak conductivity is approximated as

$$\sigma_p = \frac{e^2}{h} \cdot \frac{E_o}{2\pi\hbar\gamma_\alpha}. \tag{5.7}$$

The finding of uniform optical conductivity and equation 5.7 imply that the line-width, γ_α, of the exciton in SWNTs is inversely proportional to the nanotube diameter. As the Coulomb interaction largely determined the photophysics, the

interband scattering gives the exciton a finite lifetime. From Fermi's gold rule, the lifetime of the exciton can be expressed as

$$1/\tau_\alpha = \gamma_\alpha \propto \sum_{all_possible_states} |V|^2,$$

where V is the Coulomb potential for the scattering event. The lifetime is determined primarily by the rate of dissociation of the exciton into free carriers in lower bands. The rate of exciton relaxation (line-width) is found to be inversely proportion to the diameters of the SWNTs, as mentioned in Chapter 2 [82, 114]. In addition, the natural energy E_o of the SWNTs also shows the same scaling behavior. These two scaling behaviors cancel in equation 5.7. Therefore the peak optical conductivity in equation 5.7 is independent of the diameters of the SWNTs, as demonstrated experimentally.

On resonance, the imaginary optical conductivity is nearly zero and $Re(\sigma(\omega)) \approx |\sigma|_{peak}$. Consequently, the measured absolute conductivity $|\sigma|_{peak}$ yields a direct estimate of the peak absorption cross section width (δ_{abs}), given by $\delta_{abs}(\omega) = \pi d_{NT} Z Re(\sigma(\omega))$. This leads to a scaling relation for δ_{abs} at the peak: $\delta_{abs} \approx (0.3) d_{NT}$, consistent with recent time-resolved luminescence studies on individual (6 ,5) nanotubes[115].

5.3 Optical Coupling of Parallel Distant SWNTs

The Rayleigh scattering properties of nanotubes discussed thus far suggest that single-walled carbon nanotubes indeed behave as unique excitonic optical wires, and present an ideal optical element where the spectral response and scattered field can be determined accurately in both near and far field regimes. The integration of these nanoscale optical wires in an array geometry (where novel

properties often emerge) may lead to the development of novel metamaterials and optical devices. This requires an understanding of their coupling behavior. In fact, nanotubes are expected to couple strongly because the magnitude of the scattered (electric) field is expected to decrease as $1/\sqrt{R}$ near nanotubes (instead of $1/r$) due to the wire-like shape of nanotubes[116]. This may result in a radiative coupling between two parallel nanotube wires over a relatively long distance (much longer than the typical resonant energy transfer distance of several nanometers)[117]. Furthermore, since nanotubes are strongly absorptive on resonance and reflective otherwise, this rapid phase change of $\sigma(\omega)$ can generate a novel coupling behavior between neighboring nanotubes with strong wavelength dependence.

5.3.1 Parallel Geometry

We demonstrate such long-range coupling in figure 5.8. In figure 5.8a, we show an AFM image of a pair of nanotubes that has segments running parallel over 10 μm while maintaining a separation of about 300 nm. These nanotubes have Rayleigh peaks at 634 nm (nanotube L) and 664 nm (nanotube R) with significant spectral overlap. We assign chiral indices of (18, 7) for nanotube L and (14, 5) or (11, 8) for nanotube R based on our Rayleigh scattering and AFM measurements. A spatial map of the Rayleigh scattering spectrum reveals unusual behavior in the overlap region: the position of the scattering signal shifts abruptly from one nanotube to the other with a slight change in excitation wavelength, leaving the originally bright nanotube almost invisible (insets, figure 5.8b). This unusual coupling behavior is shown more clearly in the middle panel of figure 5.8c, where the Rayleigh intensity is plotted as a function of the wavelength

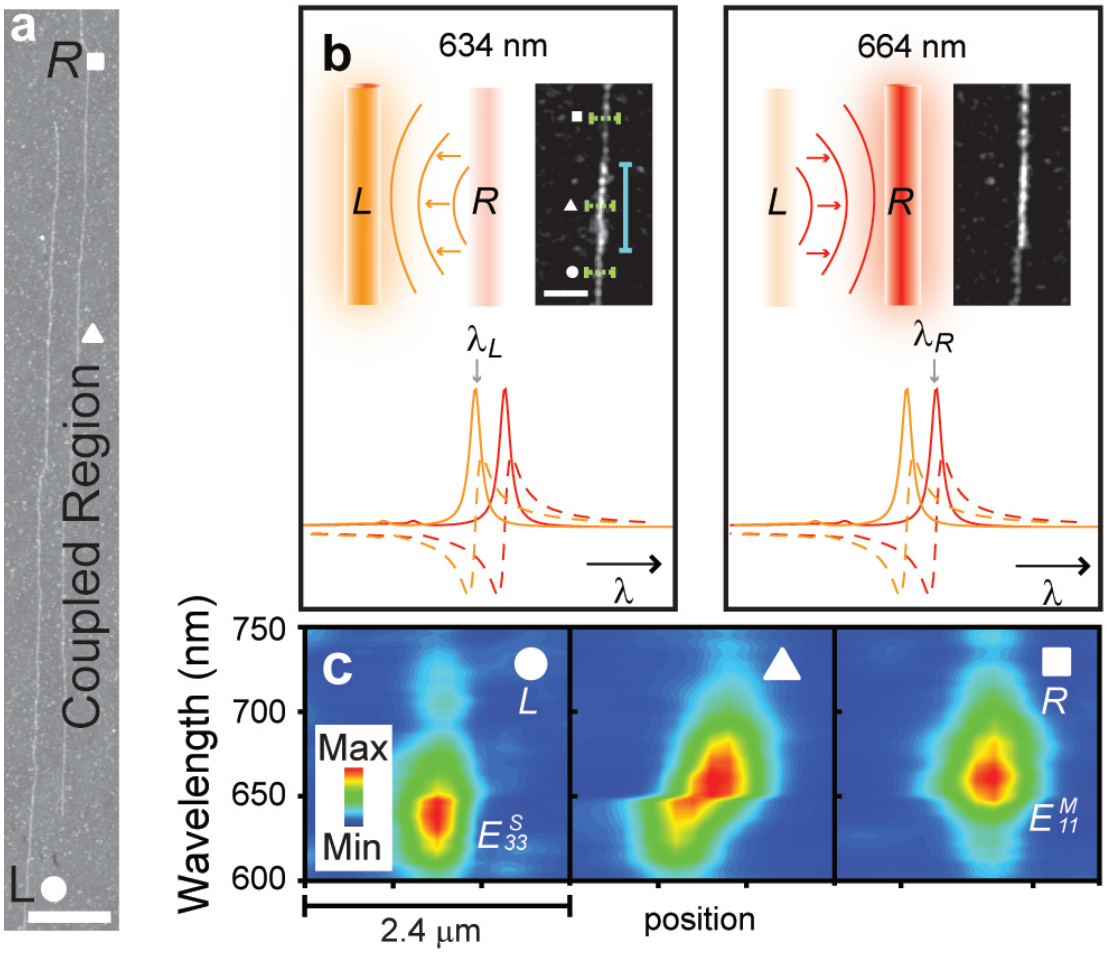

Figure 5.8: **Radiative Coupling Between Distant SWNTs.** - a) AFM image of two nanotubes with overlapping spectral resonances centered at 634 nm (l_L) and 664 nm (l_R) (for nanotubes L and R, respectively). The two nanotubes run parallel to each other over a distance of 10 μm. Corresponding height traces are shown in red. Scale bar, 1 μm. b) Main panels: optical coupling (insets show spatial Rayleigh images near the coupling region, denoted by blue lines) recorded at 634 and 664 nm. $Re[\sigma(\omega)]$ represented by solid lines and $Im[\sigma(\omega)]$ by dashed lines. Scale bar, 5 μm. c) Rayleigh scattering intensity contour of excitation wavelength versus position, for the green cross sections marked in the inset of b) for coupled (middle panel) and uncoupled (left and right panels) regions.

and the position for the interacting region. Outside of the coupled region, however, each nanotube has a typical Rayleigh scattering spectrum, as shown in the left and right panels (L and R, respectively) of figure 5.8c. Figure 5.9 compares the intensities from nanotubes L and R (after Gaussian deconvolution) in the coupled and uncoupled regions. A sharp transition (width, $<$10 nm) was again observed near 650 nm. Moreover, below the transition wavelength, the intensity from nanotube L is enhanced as much as twofold at the expense of nanotube R"s intensity; above the transition, the roles are reversed (figure 5.9). Although intertube coupling, and even exciton transfer between single-walled carbon nanotubes, have been reported in bundled nanotubes[118–120], the transfer of brightness between two distant tubes as shown in figure 5.8 has not been observed previously.

5.3.2 Absorptivity and Reflectivity from Optical Conductivity

A qualitative explanation for the observed long-range coupling behavior (schematic shown in figure 5.8b) can be introduced using classical electricmagnetism. The driving field of one nanotube is a superposition of the applied field and the scattered field of the other nanotube. When two distant nanotubes in our sample are driven in phase, the scattered field of a reflective nanotube (off resonance) can amplify the driving field of the other (on resonance), increasing its effective optical conductivity and the radiation intensity. The scattered field of an absorptive nanotube can reduce the driving field of the other, decreasing its conductivity. This can be understood from optical conductivity of SWNTs (figure 5.8b). When L tube is on resonant with wavelength, λ_L, its real part of optical conductivity is at maximum, thus highly absorptive; at excitation

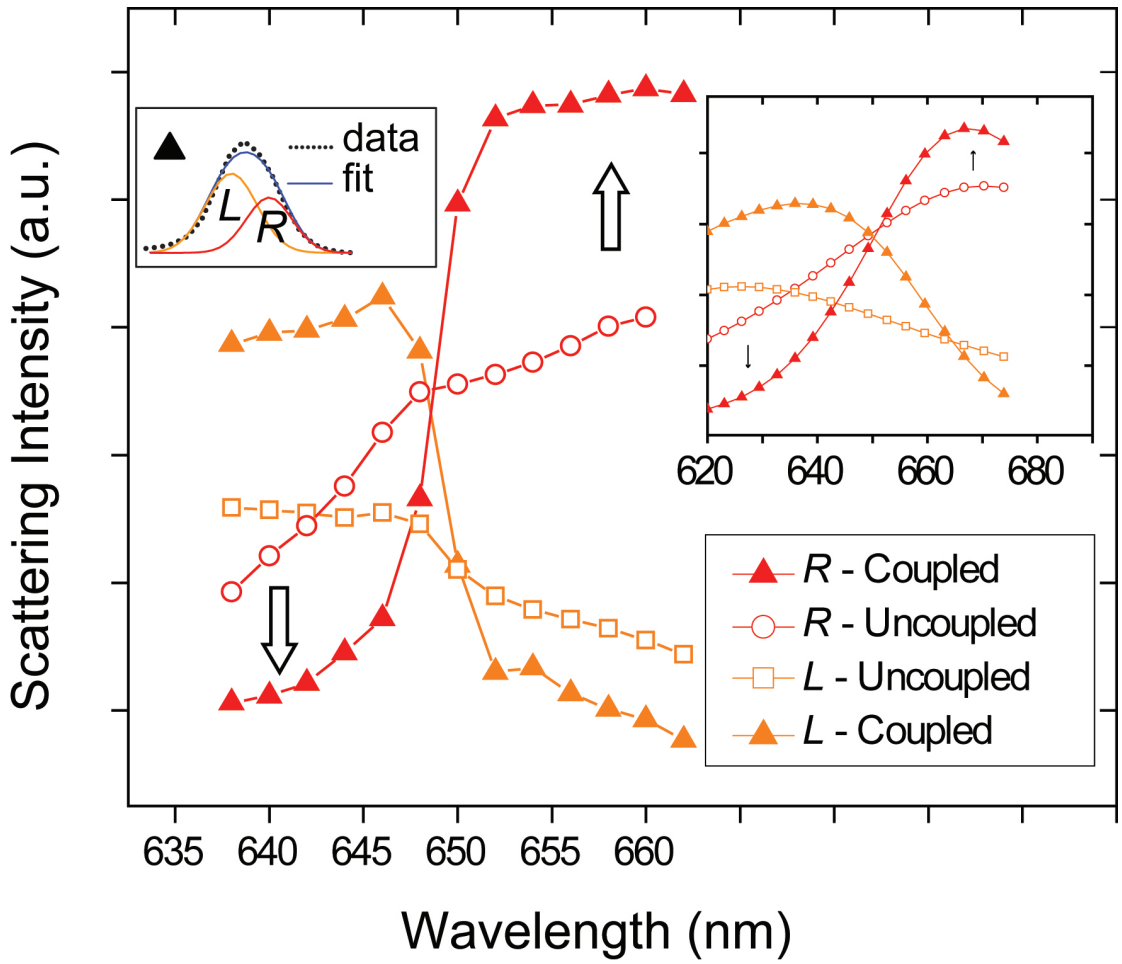

Figure 5.9: **Spectra Comparision between Coupled and Uncoupled Region** - Intensity contributions for SWNT *L* and *R* in the uncoupled and coupled regions obtained from Gaussian deconvolution. Arrows indicate the changes in the scattering intensity of tube *R* before and after intertube coupling. Inset: calculated values for the observed transition.

wavelength λ_L, the R tube is slightly off resonant, which leads to large value of imaginary party of conductivity, thus highly reflective. The superposition of these two fields leads to enhancement of brightness of L tube.

5.3.3 Quantitative Model

The superposition fields (initial excitation field E_o and scattered field E_s originating from other tube) mentioned above can be expressed as follow for these two SWNTs (L and R):

$$E_L(\omega) = \alpha_L(\omega)[E_o(\omega) + E_R(\omega)], \tag{5.8}$$

and

$$E_R(\omega) = \alpha_R(\omega)[E_o(\omega)e^{i\eta} + E_L(\omega)], \tag{5.9}$$

with the scattered field being expressed as $E_s(\omega) = \alpha(\omega)E_o(\omega)$, η accounts for the phase difference in the applied field between the two SWNTs, and E_o is the driving field from the laser. α imposes a relationship between the intensity of the driving field and scattered field at distance, D, away from the SWNTs. The scattered field corresponds to the surface current of the SWNTs being induced by the driving field, E_o.

The superposition fields at each SWNTs are

$$E_L(\omega) = \frac{1 + e^{i\eta}\alpha_R(\omega)}{1 - \alpha_L(\omega)\alpha_R(\omega)}\alpha_L(\omega)E_o(\omega), \tag{5.10}$$

and

$$E_R(\omega) = \frac{1 + e^{-i\eta}\alpha_L(\omega)}{1 - \alpha_L(\omega)\alpha_R(\omega)}\alpha_R(\omega)E_o(\omega). \tag{5.11}$$

In here, when $|\alpha| < 1$, the scattered fields are those of independent SWNTs; When $|\alpha| \approx 1$, the scattered field of a SWNT is strongly affected by that of the other SWNT. On resonant, the peak conductivity of the SWNTs ($\approx 10e^2/h$) gives the value of $\alpha \approx 10\frac{e^2}{\hbar\omega}\frac{R}{D^2} \approx 10^{-5}$, with the distance $D \approx 300nm$ in our experiment. However, the conductivity, calculated from the mean field description of light

scattering, is being too small to produce a qualitative feature of the data shown in figure 5.9. A qualitative model, with conductivity being the free parameter, shows this coupling behavior in the inset of figure 5.9, with the assumption of α enhanced by a factor of 1000. Theoretical model for this enhancement is currently not available. To incorporate such drastic enhancement, a new theory, that accounts for temporal and spatial fluctuations associated with the exciton dynamics, is required.

CHAPTER 6

CONFOCAL ABSORPTION MICROSCOPY

6.1 Depolarization Effect in Confocal Optical Absorption Measurement

Absorption cross section is a key parameter essential for characterizing the intrinsic efficiency of optical processes in semiconductors. The same is true for the performance of optical and optoelectronic devices, including photovoltaic cells, photo detectors, CCD arrays, and lasers [25, 26, 121–125]. Recently, building these devices from nanostructures has attracted wide attention, as it makes possible new functionalities as well as high sensitivity. Examples include plasmon enhanced light-emitting devices, optical power limiting devices, optical antennas, and optical wires[126–129]. Accurate measurements of optical absorption in nanostructures, usually quantified with an optical cross section, is critical for the design and optimization of nanostructure based optoelectronic devices. In this chapter, we describe how to directly measure the absolute absorption cross section of SWNTs on resonance using confocal absorption imaging techniques, but we first discuss the depolarization effect on the confocal measurement using high numerical aperture lenses.

6.1.1 Optical Absorption Measurement with Sub-Micron Spatial Resolution for Individual Nanostructures

For measuring the optical absorption of nanostructures, there are two experimental approaches: ensemble measurements and individual measurements. Individual measurements yield more accurate information by revealing the heterogeneity of nanostructures. In order to determine the optical properties of individual structures at sub-micron spatial resolution, localization of laser excitation at the diffraction limit is often required, which is typically achieved by using high numerical aperture objective lenses.

The spatial resolution of high numerical aperture objective lenses is fundamentally limited by the Abbe diffraction limit, which is written as

$$d = \frac{\lambda}{n \sin \theta}, \tag{6.1}$$

where n is the refractive index of the medium and θ is the semiaperture angle (SA) (see figure 6.1).

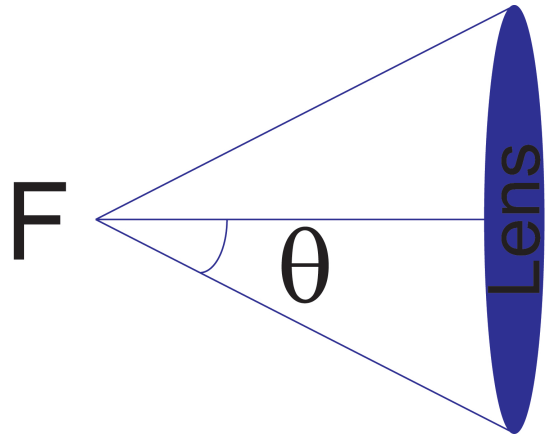

Figure 6.1: **Schematic of Light Ray Focusing** - Light beam travel through the lens and focus at point F with θ as the semiaperture angle (focusing angle).

6.1.2 Origin of Depolarization Effect

To measure the light absorption of individual nanostructures, for instance, the use of two focusing and collecting lenses with matching NA (figure 6.2a), in combination with laser scanning optics allows spatially resolved imaging of light transmission (thus local extinction or absorption) in the diffraction limit [130]. While the measurements between ensemble and individual measurement could yield, in principle, the same results as measurements done with collimated light on macroscopic samples, these two platforms produce different light fields at the sample location. In particular, the focusing optics modify the light polarization at the focal plane from that of the collimated beam with the degree of modification determined by the NA, or equivalently the SA.

This effect, generally referred to as the depolarization effect, is important especially for optical and optoelectronic characterization of nanostructures, because their optical properties are polarization sensitive. This sensitivity is due to geometric confinement associated with nanoscale dimensions.

This effect was first investigated theoretically in 1959 by Richards & Wolf [131]. It can also be understood phenomenologically from the vectorial nature of the electromagnetic field and ray optics[132]. Different rays of a light beam have the same polarization prior to reaching the focusing lens, but the polarization of each ray can be tilted differently with the outermost ray having the largest tilt (figure 6.2a) and the strongest depolarized field component. We perform numerical simulation in Matlab (see Appendix for code), and use the calculation based on conventional electromagnetic theory [131]. The calculation indicates that the $|E_z|^2$ component can be as large as 20% of $|E_x|^2$ along the original polarization direction for a semiaperture angle $\theta = 67°$. This clearly

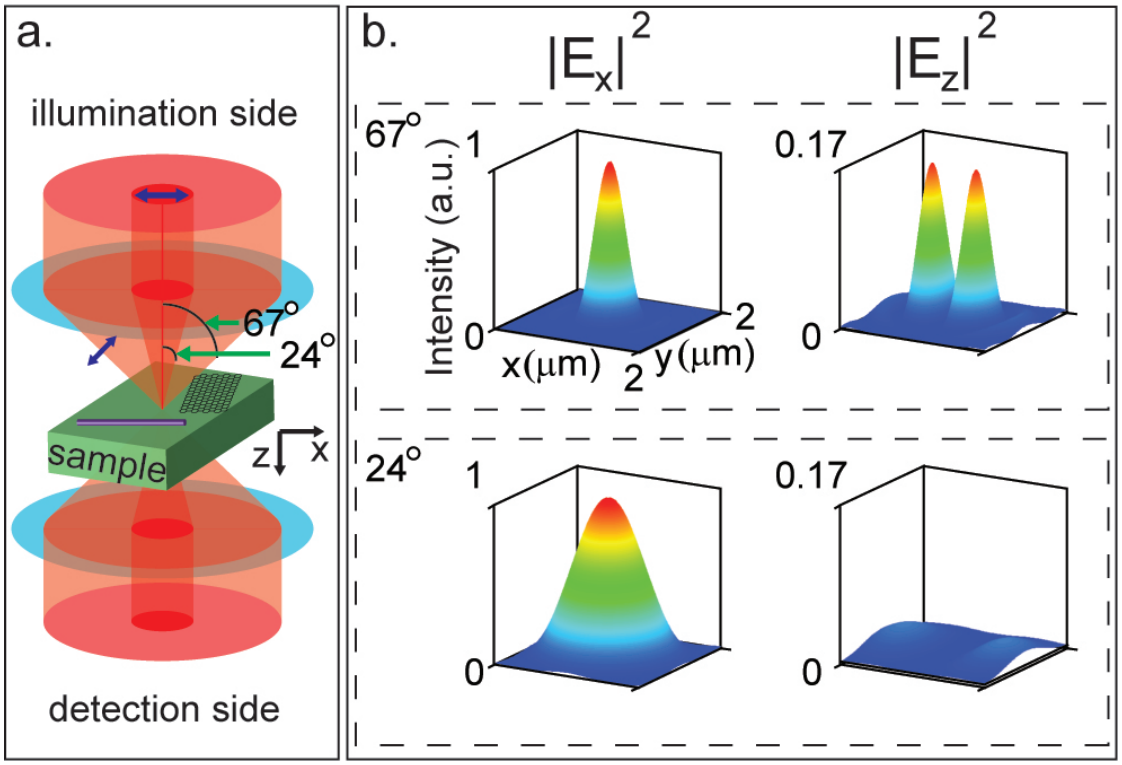

Figure 6.2: **Measurement Scheme and Calculated Depolarization Effect at the Focal Plane.** - (a) Linearly polarized light (785 nm) is introduced into an oil-immersion objective lens with an adjustable numerical aperture (upper blue disk), with the polarization direction shown as a blue arrow. The light transmitted through the substrate, which has various nanostructures resting on its surface, is collected by an oil-immersion lens (lower blue disk) with a fixed numerical aperture (NA=1.4). The initial polarization before the lens is along the x-direction, and the z-direction is defined as being normal to the sample. Two representative semiaperture angles are shown here. Focusing the light with the larger semiaperture angle tilts the polarization, introducing a measurable z-component. (b) Calculated intensities of the x and z components of the electric field incident upon the sample focal plane are shown for different SAs. All intensities at different SAs are normalized to the x-component.

shows that a linearly polarized laser beam will produce a polarization component perpendicular to the focal plane. This depolarization effect has also been seen experimentally[132, 133].

It is expected that the light absorption in 1D and 2D nanostructures would be sensitive to the illumination geometry in addition to their intrinsic optical properties. However, this effect is often unjustifiably ignored. The depolarization of focused light causes significant changes to the measured absorption values, the effect of which is larger for high NA optics. We investigate this effect by measuring absorption cross-sections of prototypical 1D (semiconducting NWs) and 2D (graphene) nanostructures using confocal transmission absorption measurements, while varying the SA of illumination.

6.1.3 Experimental Setup

Figure 6.2a shows our experimental scheme. A linearly-polarized, collimated, CW laser beam (785nm) was focused by an oil immersion objective lens with variable NA (between 0.6 - 1.35; Olympus 100x) to obtain different SAs from 24° to 67°. Both NW and graphene samples are deposited on transparent fused silica substrates, which have prepatterned alignment marks for locating samples for further characterization, e.g. AFM. Our graphene is grown using CVD methods on copper foils and then transferred onto the substrate following a wet transfer technique[134]. Our NWs are CVD grown Germanium (Ge) NWs sonicated lightly in methanol and deposited onto the substrate[135]. The transmitted light was collected using another oil immersion lens with a larger collecting SA (73°) at the back of the sample. In order to produce a map of the absorption values,

the intensity was recorded as a function of the focused laser spot position, which was controlled by custom-built laser scanning optics. A series of such images, normalized to the total laser power, was taken with different SAs. We use this to investigate the depolarization effect in the absorption measurements. In typical measurements, another photo detector was installed as a reference to monitor the intensity of the laser before the objective lens.

6.1.4 Depolarization Effect in Absorption Measurements of Two-dimensional Nanostructures (Graphene)

Single-layer graphene, a one-atom-thick film, provides an excellent example of two-dimensional (2D) nanostructures as mentioned in chapter one. Its absorption of light is strictly limited to light with polarization parallel to the graphene surface with uniform absorption efficiency (~2.3%) over broad infrared and visible wavelengths[69]. In contrast, graphene does not absorb light polarized perpendicular to its surface[51].

Two representative absorption images for a graphene sample are shown in figure 6.3a. A uniform background signal is subtracted from both images. These images are taken for two different SAs. For a 24° semiaperture angle (NA = 0.6), the (area averaged) absorption of light for graphene is measured 2.16 ± 0.07%, close to the well known 2.3% [69, 136]; however, for 67° (NA = 1.35), it is only 1.76 ± 0.06%. In both cases, the intensity of the focused laser (approximately 80 kW/cm^2) is well below the saturation intensity[137]. This behavior is consistent with the depolarization effect. At a small SA of 24°, the total intensity has little contribution from the normal polarization component (figure 6.2b bottom,

$|E_z|^2$), while at a large SA of 67°, the normal component's global maximum intensity is almost 20% that of $|E_x|^2$ (figure 6.2b top). As all dipole transitions are constrained within the π bands of graphene at this wavelength,[51] any normal component of the light will not be absorbed, and thus increases (decreases) the total transmission (absorption) of light. Therefore, as we increase the semiaperture angle of the illumination, the $|E_z|^2$ component increases, decreasing the measured absorption. Indeed, our data is fully consistent with this expected behavior (figure 6.3b). Furthermore, our data is in excellent agreement with our theoretical calculation (solid line in figure 6.3b). We obtained our theoretical fit by assuming 2.2% absorption in the tangential polarization direction and zero absorption in the normal direction.

Our results shown in figure 6.3 clearly demonstrate that graphene's optical absorption requires correction (as much as 20%) at large semiaperture angle illumination and that the decrease in the apparent optical absorption is proportional to the amount of depolarization component (in this case $|E_z|^2$). It also experimentally confirms the predicted magnitude of $|E_z|^2$, which has never been done before.

6.1.5 Depolarization Effect in Absorption Measurements of One-dimensional Nanostructures (Nanowire)

Semiconducting nanowires (NWs) as well as SWNTs are expected to show behaviors of one-dimensional (1D) structures. Light is most strongly absorbed when its polarization is along the longitudinal (axial) direction of NWs or SWNTs, which is often quantified by the absorption anisotropy ratio, δ =

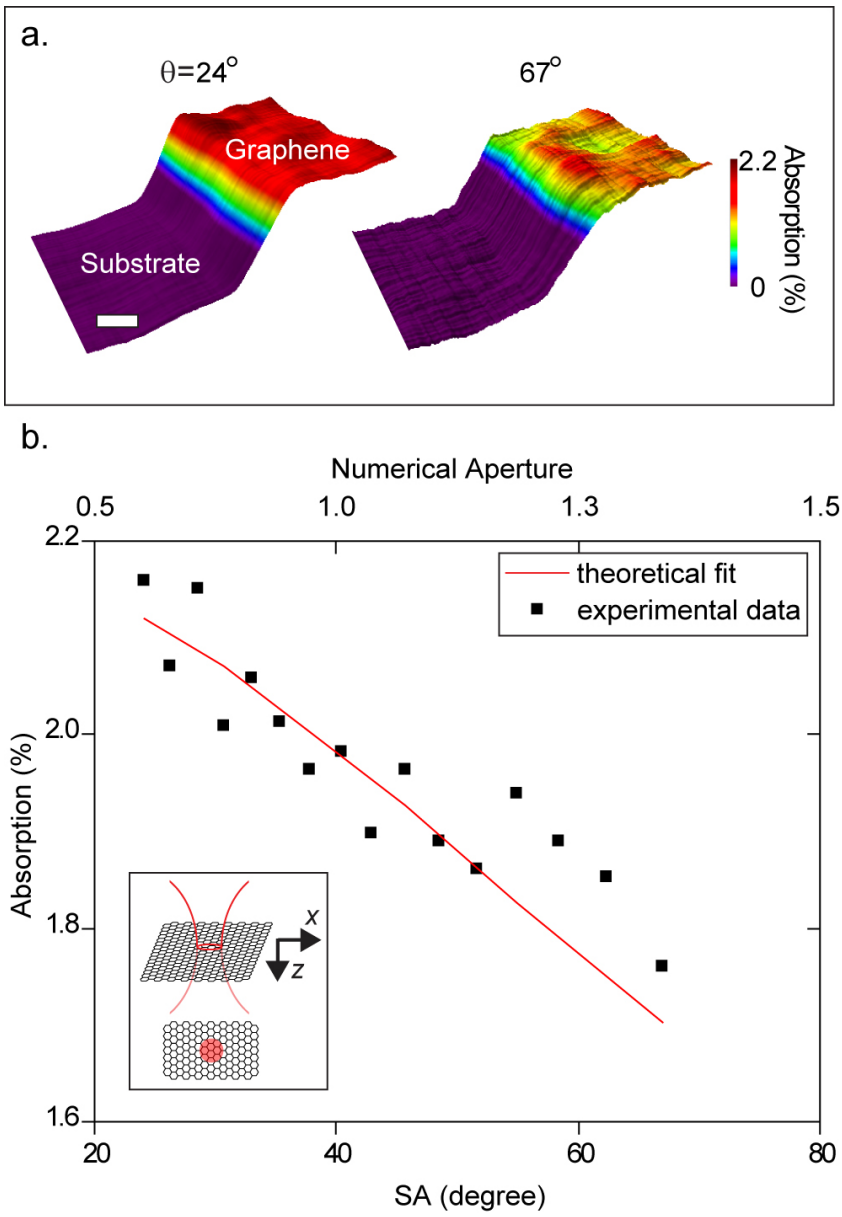

Figure 6.3: **The Experimentally Measured Absorption in Graphene Depends on Semiaperture Illumination Angle.** - (a) Absorption of light at the same area of the sample for two different semiaperture angles. The absorbance of the substrate was set to zero following uniform background correction. Scale bar, 5 μm. (b) Experimentally measured (black squares) and theoretical curve (red line) of absorption of graphene as a function of semiaperture angle. The theoretical curve takes into account the depolarization effect at the focal plane obtaining the fitted tangential absorption of light to be 2.2% for graphene. Inset: Laser beam diameter is smaller than the area of the graphene sheet, which is assumed in the calculation.

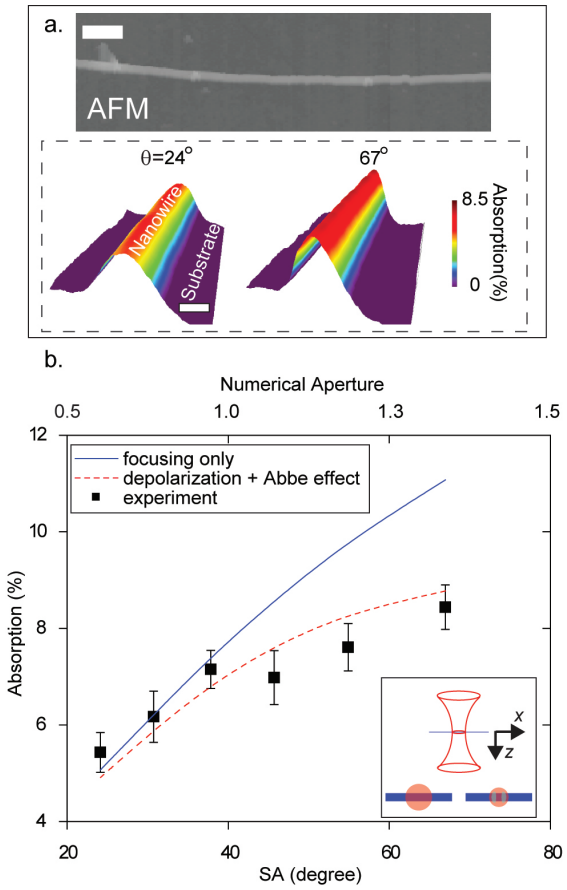

Figure 6.4: **Dependence of Measured Absorption Versus Semiaperture Angle of Illumination, for Ge Nanowires.** - (a) Upper: AFM image of a representative Ge nanowire (d ~ 65nm). Scale bar, 1 μm. Lower: Measured absorption of light of the same nanowire for two different semiaperture angles. Scale bar, 0.5 μm. (b) Experimentally measured (black squares) and calculated (blue and red curves) absorption for various semiaperture angles of illumination. The calculation represented by the blue curve includes only the Abbe diffraction effect in the absence of depolarization. The red curve, however, includes the depolarization effects. Both calculations for this nanowire use $Q_{\|} = 85\%$ in the portion of the nanowire being illuminated. The latter uses $\delta = 70\%$. Inset: Schematic illustrating that the nanowire diameter is smaller than the beam diameter. Smaller semiaperture angles lead to larger laser spot diameters (left) and vice versa (right), with the z component (shaded area) only being significant in the latter.

$(Q_{\parallel} - Q_{\perp})/(Q_{\parallel} + Q_{\perp})$, where $Q_{\parallel}$ ($Q_{\perp}$) is the absorption efficiency for light having longitudinal (perpendicular) polarization. For NWs, the absorption efficiencies are defined as the ratio of the absorption cross section to the physical cross section[138]. In figure 6.4, we explore the depolarization effect in 1D linear structures. GeNWs are chosen as they are an ideal material for this study. First, GeNWs have large absorption cross sections because Ge has a direct band gap, producing a better signal-to-noise ratio in our measurement, as compared to other indirect band gap materials (such as Si). In addition, their polarization anisotropy was shown to be strongly diameter-dependent, increasing from 50% to 98% as the diameter changed from 70 nm to 20 nm[139].

First, both optical microscopy and AFM are used to locate and characterize the GeNWs. An example AFM image is shown in figure 6.4a (upper) for a GeNW with diameter ~ 65nm. In figure 6.4a (lower), after aligning the light polarization (before focusing) to the NW's axis, we compare the absorption of the NW at two different SAs, as in graphene case. The data at 67° shows a higher and narrower absorption peak compared to the case of 24°. This behavior is expected. As the semiaperture angle increases, the focused spot size becomes smaller (the Abbe diffraction effect) and allows more light to be localized around the NWs (figure 6.4b, inset), especially when the NW diameter is smaller than the beam spot. In figure 6.4b, we plot the peak absorption values measured while varying the SAs of illumination. They monotonically increase for larger SAs closely following the prediction of the Abbe effect (blue curve). However, at large SAs, the depolarization effect introduces a significant amount of field with polarization along z direction and thus lowers the absorption.

In order to obtain the theoretical fits for absorption with and without the

depolarization effect for NWs, we assume the effective diameter of this NW to be 60 nm after considering the native oxide of GeNWs[140]. The anisotropic ratio, δ, is predicted to be 70% for this diameter[139]. We further divide the focused laser beam spot into two regions. One region is the overlapping area between the NW and laser spot. In this region, the field intensity of each polarization is denoted as I_{NW}^{x}, I_{NW}^{y} and I_{NW}^{z} with x being along the longitudinal direction of the NW. Similarly, for the region excluding the overlapping region, the intensity of each polarization is denoted as I_{E}^{x}, I_{E}^{y} and I_{E}^{z}. The experimentally measured absorption is expressed as $(Q_{\parallel}, Q_{\perp}, Q_{\perp})\cdot(I_{NW}^{x}, I_{NW}^{y}, I_{NW}^{z})/I_{total}$, where $I_{total} = (I_{NW}^{x} + I_{NW}^{y} + I_{NW}^{z}) + (I_{E}^{x} + I_{E}^{y} + I_{E}^{z})$ and $Q_{\parallel}$ and $Q_{\perp}$ are defined previously as the absorption efficiency for different polarizations. We obtained our theoretical fit assuming $Q_{\parallel} = 85\%$ (red curve). This value is consistent with respect to the cylindrical NW geometry calculation combined with the previously measured absorption efficiency for the assumed diameter[135, 139].

6.2 Spatial Modulation Confocal Absorption Microscopy

Absorption cross section is fundamentally and practically important, as mentioned in the previous section. Furthermore, the absolute value of the absorption cross section provides accurate fundamental information on the optical processes of materials. For bulk materials of known thicknesses, this measurement can be performed using the Beer's law by comparing the initial and final intensity of the collimated light beam shining through the materials. However, absorption cross section measurements for nanostructures are inherently difficult, due to the size differences between the diffraction limit of light (equation 6.1) and nanostructures. The diffraction limited size of a focused laser spot is

typically several hundreds of nanometers, yet the nanostructures have sizes as small as a few tenths of a nanometer. This size difference introduces a large background in the noise, as compared to the weak absorption signal, despite the utilization of confocal microscopy. By using innovative techniques to subtract the illumination background, it is still possible to measure the absolute value of absorption cross section of nanostructures and/or single molecules [141, 142]. In this chapter, in addition to measuring the absolute value of the absorption cross section of SWNTs directly using a spatial modulation method, we also extract this value on and off SWNTs' resonance. The oscillator strengths of different optical transitions for SWNTs may be measured this way.

6.2.1 Spatial Modulation of Laser for Absorption Imaging

A promising method for subtracting the illumination background is the use of a spatial modulation technique. This technique has been previously used in literature [142, 143]. By modulating the focused laser beam around a SWNT with frequency ω (figure 6.5), the detected intensity of the light beam (reflection and/or transmission mode) has a sinusoidal profile in time domain (figure 6.6 top panel). This can be understood as follows. First, the intensity of a focusing laser beam spot is single mode with Gaussian profile G. Second, the beam spot is spatially modulated at amplitude A, with the SWNT placed x_o away from the beam center and the SWNT having an absorption cross section width δ_{abs}. To the first order approximation, the intensity of the laser beam, which is detected in time domain, has two extrema, $\delta_{abs} \cdot G(x_o + A/2)$ and $\delta_{abs} \cdot G(x_o - A/2)$, for the sinusoidal profile. After lock-in amplification, the signal in the frequency domain has a functional form of the derivative of the Gaussian, with argument

of x, which is the displacement between the beam center and average position of the SWNT (figure 6.6 bottom panel).

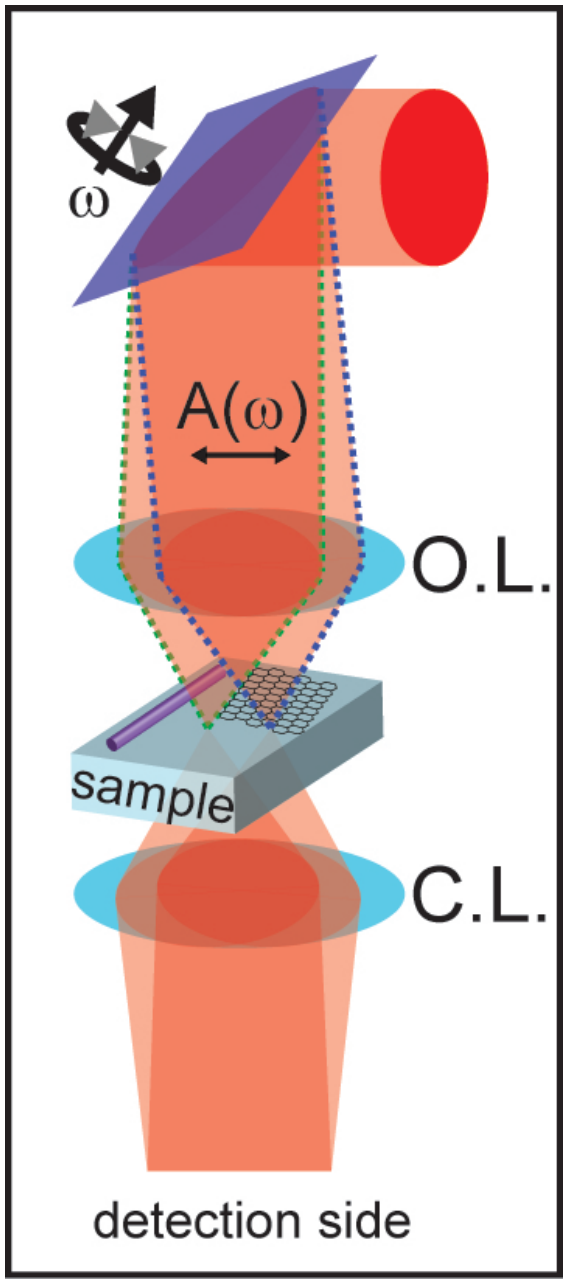

Figure 6.5: **Experimental Setup** - Spatial modulation is controlled by a mirror with a modulating frequency ω with amplitude $A(\omega)$. The detection mode is transmission. Both objective and collection lenses are oil-based with the collection lens having a larger NA.

To obtain spatial modulation, we use a piezo mirror (Thorlabs, ASM003)

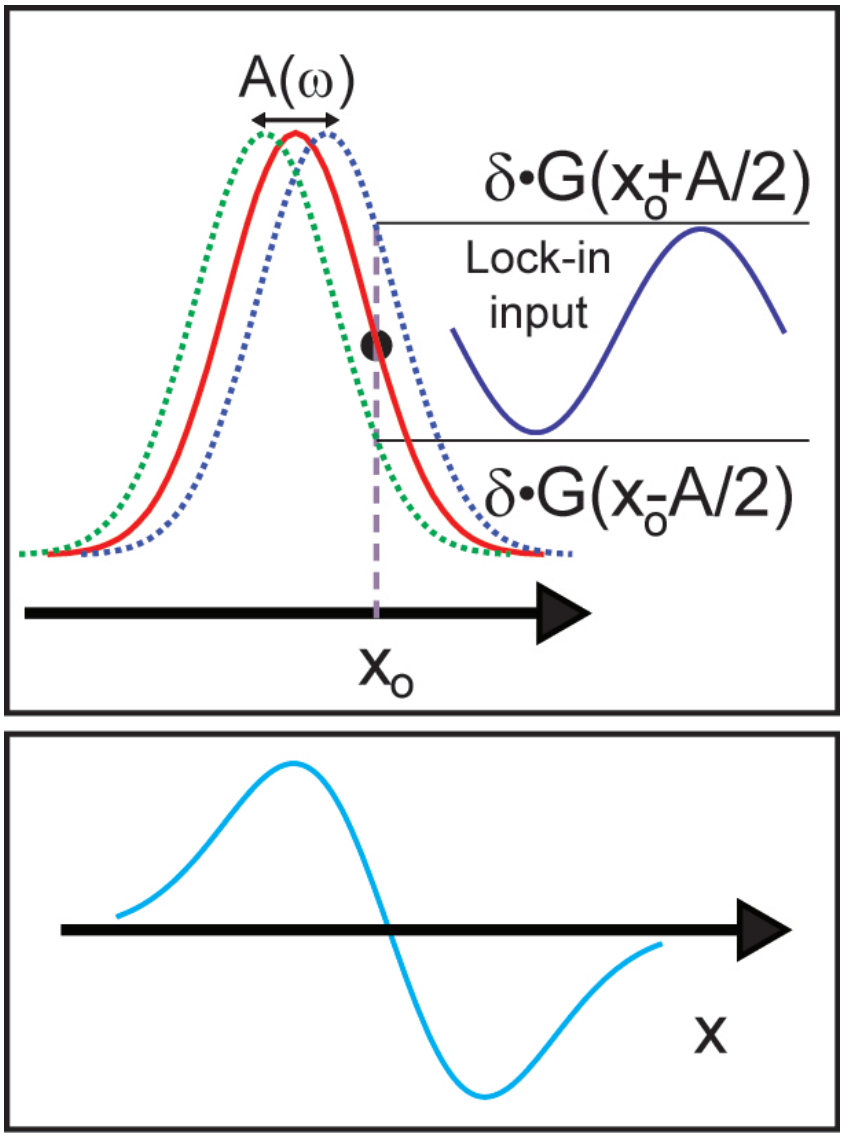

Figure 6.6: **Modulation Signal** - In the time domain, the signal is detected a the photo detector, as the focused Gaussian beam is being modulated around a SWNT placed at x_o (top). The functional form of the signal after lock-in amplification, with argument of x being the displacement between the beam center and average position of the SWNT (bottom).

modulating at frequency 2 KHz. The modulation amplitude is calibrated as follows. First, by capturing the time averaged image of the modulated beam spot using a CCD camera, we obtain the width of the beam spot after fitting it to a 2D Gaussian. Second, from the measured width, we use Matlab to simulate the modulation amplitude as shown in figure 6.7. The calculation code is provided in the Appendix. This allows us to relate the modulation amplitude (A) and the width of the modulated beam width. In the actual experiment, we have the modulation amplitude $A = 86nm$. Furthermore, two laser lines are used in this experiment, 785 nm and 632 nm.

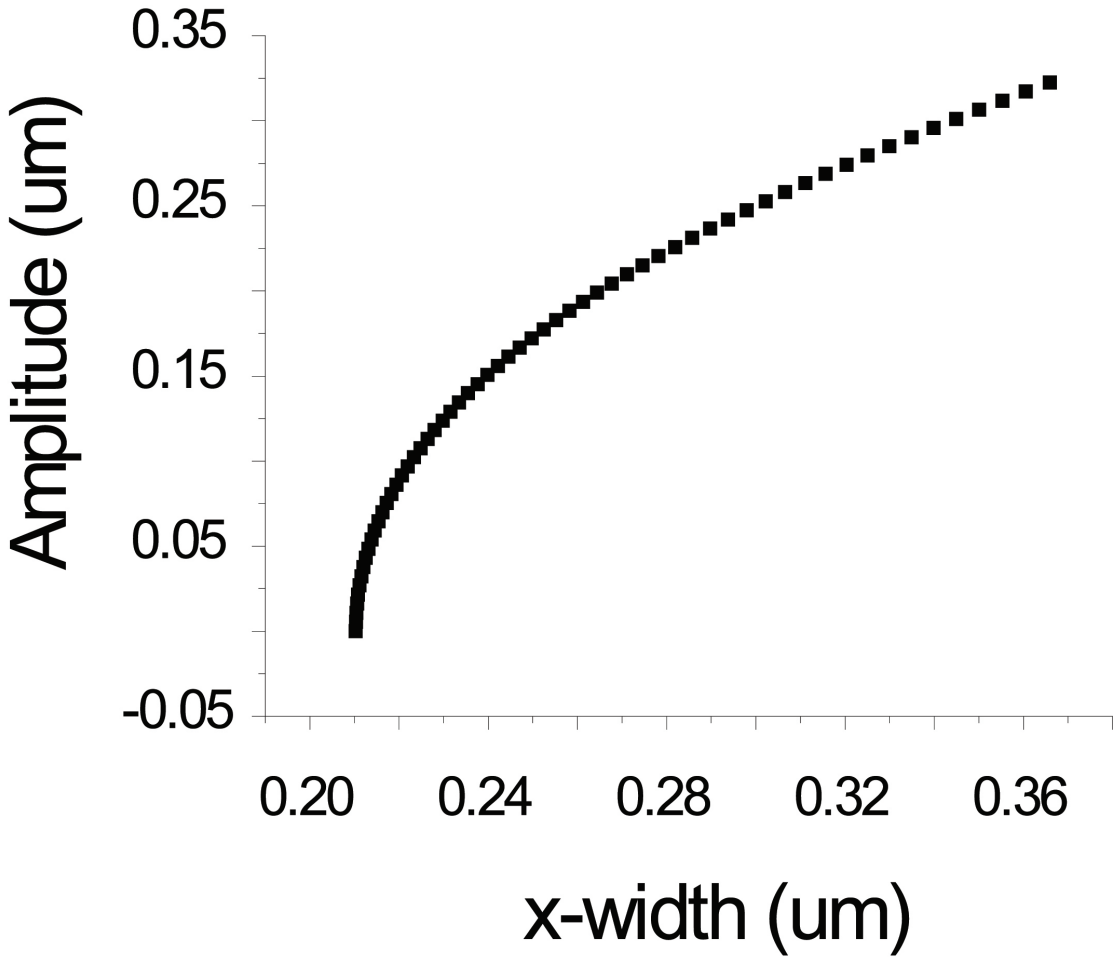

Figure 6.7: **Numerical Simulation** - Calculation for the relation between the modulation amplitude A and the width of the modulated beam width

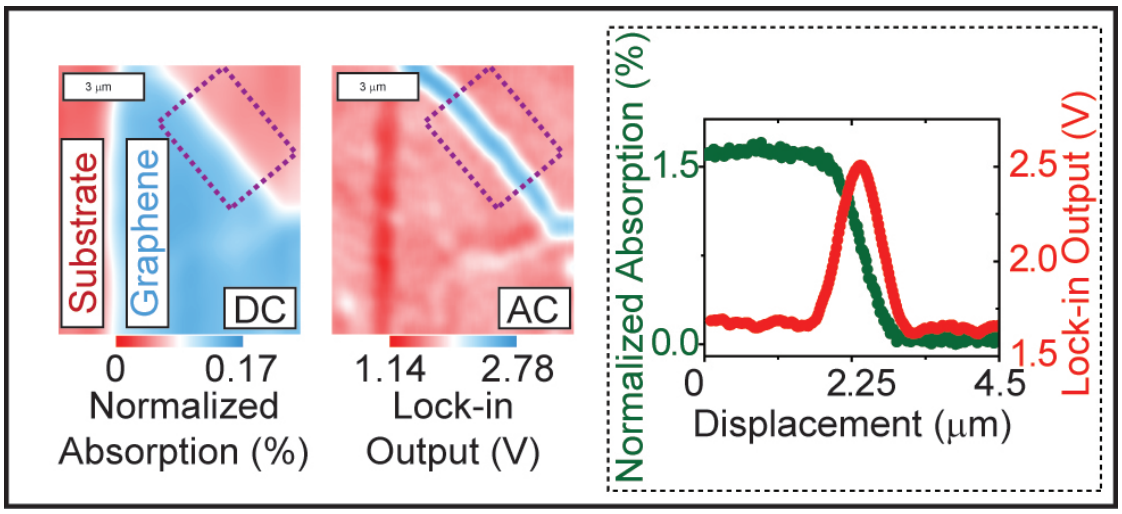

Figure 6.8: **Correction from Depolarization** - Graphene is used to measure the correction from the depolarization effect: We used the raster scanning method to obtain the absorption image of graphene (DC). The raster scanning method, combined with concurrent spatial modulation, is also shown here (AC). Both the normalized absorption and lock-in output are presented on the right.

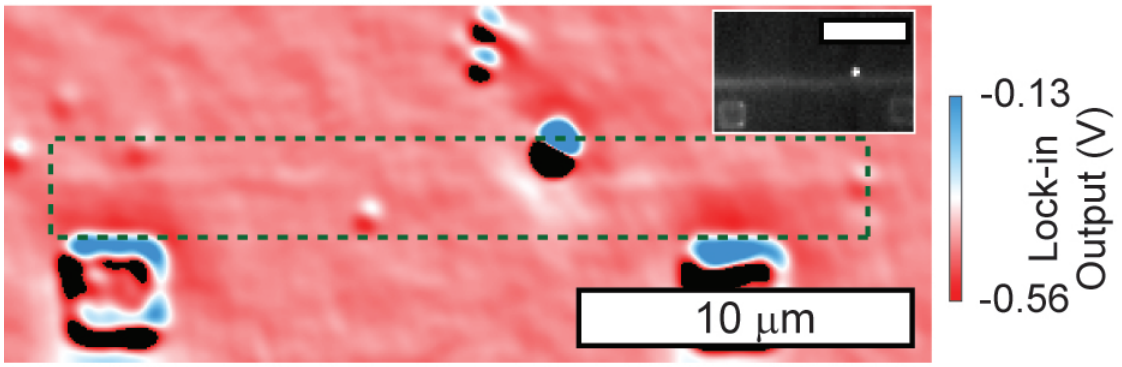

Figure 6.9: **Absorption Imaging of a SWNT** - An image of SWNT on a quartz substrate was captured by using the spatial modulation method in transmission mode

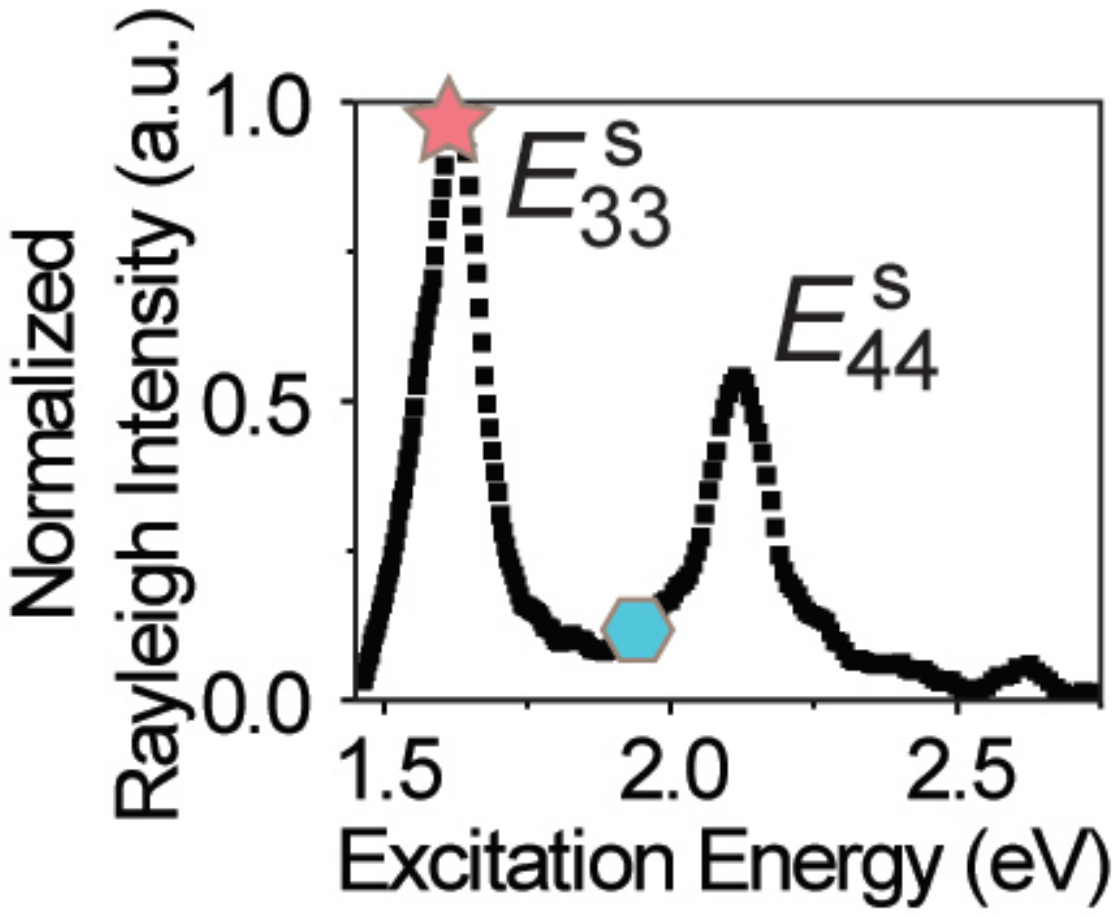

Figure 6.10: **Rayleigh Spectrum for the SWNT of Interest** - Rayleigh spectrum measured by on-chip wide-field setup

6.2.2 Absorption Calibration Using Graphene

As mentioned previously, the polarized laser intensity will be partitioned into different polarization directions due to a high numerical aperture objective lens. In this experiment, we use a 60X objective lens with 1.3 NA. To calibrate the proper absorption cross section for the SWNTs, we use graphene's absorption as a calibrator, since we know that graphene's absorption is 2.3% with polarization in the tangential direction. We use both DC (non-modulation) and AC (with modulation) to obtain the absorption of graphene. Comparing the absorption between 2.3% and measured absorption 1.5%, this gives us a 1.5 ratio correction

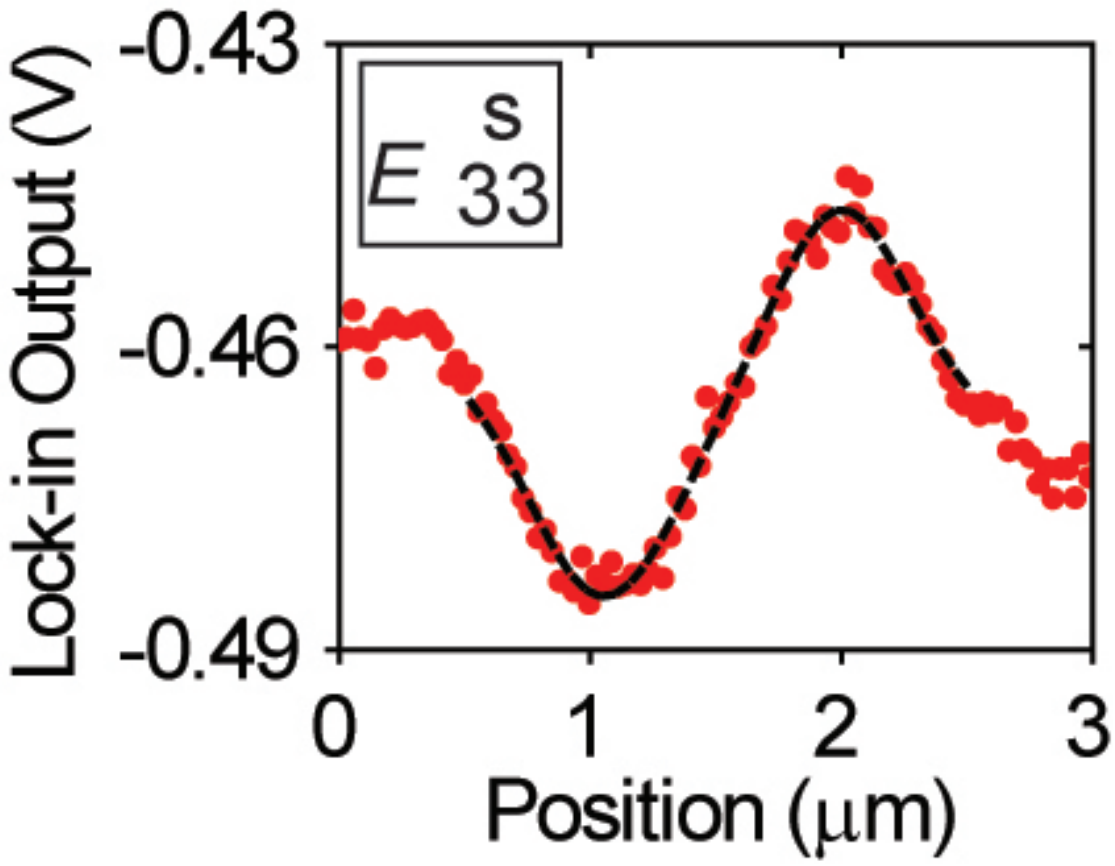

Figure 6.11: **Line Cut Across the SWNT Image** - Extracting the absorption cross section from data after averaging the vertical cuts from figure 6.9.

for our calibration (figure 6.8).

6.2.3 Absorption Cross Section of SWNT

To measure the absorption cross section of SWNT, we used Rayleigh spectroscopy and microscopy to find a SWNT. The Rayleigh spectrum for this SWNT is shown in figure 6.10, with diameter $d_{NT} = 1.9nm$. Two of the laser lines were employed to measure the absorption image of this SWNT. At 632 nm, as indicated by the blue dot, the signal of the SWNT is around the noise level. At 785 nm (red star), we can image the absorption of this SWNT as shown in figure

6.9. At this excitation energy, the SWNT is on E_{33}^{S} resonance. The location of this SWNT is also confirmed by using EFM measurement. As we take the averaged vertical cuts over the nanotube image, we obtain data as shown in figure 6.11. This allows us to extract the absorption cross section width to be $0.53 \times d_{NT}$, with the consideration of the depolarization effect. This value is consistent with previous reports [50, 142].

CHAPTER 7

SUMMARY AND FUTURE WORK

7.1 Summary

Two optical measurement platforms are developed to image SWNTs. The first one, wide-field on-chip Rayleigh spectroscopy and microscopy, utilizes wavelength dependent Rayleigh scattering mechanisms to obtain the chirality of SWNTs. This also allowed us to observe various interesting and new behaviors, such as long range optical coupling and uniform optical conductivity on resonance. The second technique, by using high numerical aperture oil immersion objective lenses, demonstrates the possibility of accurate quantitative absorption measurements for individual structures on the nanometer scale.

In the first two chapters, we discussed the importance of optical imaging and probing techniques for the single-walled carbon nanotube, briefly reviewed the physical properties of SWNTs, and mentioned the experimental methods for studying optical transition in SWNTs.

In chapter three, we presented some of the theory for optical transitions in SWNTs. We also discussed the excitonic effects.

In chapter four, we presentd the growth and fabrication techniques for SWNTs and Rayleigh spectroscopy and imaging techniques. Details of selecting quartz wafers, preparing for the substrate prior to the SWNT growth, and the growth steps were discussed. Furthermore, we also mentioned how to prepare ultra clean samples for on-chip Rayleigh measurement. We then described the experimental setup and methods for resolving and imaging the chirality and

heterojunctions of SWNTs.

In chapter five, we described the Rayleigh scattering pattern from individual SWNTs, which indicates SWNTs are behaving like optical wires. We then presented uniform optical conductivity and its origin from excitonic effect. Lastly, we demonstrated the possibility of optical coupling between two SWNTs and described a qualitative model to explain this phenomenon.

In chapter six, we discussed how to measure the absorption cross section of individual SWNTs. Theoretically and experimentally, we investigated the depolarization effect measured using high numerical aperture objective lenses for absorption measurements. This gives us a correction of the absorption measurement of individual SWNTs. Lastly, we describe the spatial modulation confocal absorption measurements of individual SWNTs. This allows us to measure the absolute absorption cross section of SWNTs.

7.2 Future Work

The long rang optical coupling between two SWNTs is not well understood. Although we presented a qualitative model by assuming the effective optical conductivity of SWNTs is 1000 times larger than the calculation from the current theoretical model, the physical origin behind the energy transfer mechanism is not shown. Experimental confirmation on the energy transfer for such long distance between two SWNTs, is needed, using absorption, or Raman measurement.

CHAPTER 8

APPENDIX

.1 Appendix I: Mathematica Codes for Extracting the Scattering Cross Section from Scattering Intensity

```
Calculating (# photon)/Area (Excitation)
*USER INPUTTED VALUES*
(*LaserPower[\[Mu]W], xLaser and yLaser [pixel], \[Lambda]
    [nm]*)
\[Lambda] = 744;
LaserPower = 378;
xLaser = 312;
yLaser = 637;
Xgauss = 741.73;
Ygauss = -544.53;
XWgauss = 154.72;
YWgauss = 721.62;
cGauss = 0.22703;
Defining 2D Gaussian and Power = Integral over 2D Gaussian
TwoDimGauss[A_, x0_, Wx_, y0_, Wy_, c_] =
  A Exp[(-1/(
      2 (1 - c^2))) (((x - x0)/Wx)^2 + ((y - y0)/Wy)^2 -
         ((
        2*c (x - x0) (y - y0))/(Wx*Wy)))];
LaserP[A_, x0_, Wx_, y0_, Wy_, c_] =
```

```
  Integrate[A Exp[(-1/(
       2 (1 - c^2))) (((x - x0)/Wx)^2 + ((y - y0)/Wy)^2 -
          ((
         2*c (x - x0) (y - y0))/(
         Wx*Wy)))], {x, -\[Infinity], \[Infinity]}, {y,
            -\[Infinity], \
\[Infinity]}];
Solving for Amplitude of 2D Gaussian when measured power
   is 366 \[Mu]W
NOTE!:  By [pixel], i mean pixel LENGTH
AmpExpr = A;
Amp = Flatten[
  Solve[LaserP[A, Xgauss , XWgauss, Ygauss , YWgauss,
     cGauss] == LaserPower,
   A]]
{A -> 0.000553284}
Amplitude = AmpExpr /. Amp
0.000553284
Determine value of 2 D Gaussian evaluated at point (x,y)
   of CNT Image
Evaluating for the coordinates (x,y), we obtain the
   magnitude of the Gaussian in units[\[Mu]W/\[Mu]m^2]:
TwoDimGaussValueXY = (TwoDimGauss[Amplitude \[Mu]J/(sec
   pixel^2), Xgauss ,
      XWgauss, Ygauss , YWgauss, cGauss])*(pixel/(.161 \[
         Mu]m))^2 /.
```

```
   x -> xLaser /. y -> yLaser
(0.0000299632 \[Mu]J)/(sec \[Mu]m^2)
Converting power/area to (# photon)/area
Excitation =
 TwoDimGaussValueXY*1 J/(10^6 \[Mu]J)*1/((1240/\[Lambda])
    eV)*(1 eV)/(
  1.60217*10^-19 J)*photon
(1.1221*10^8 photon)/(sec \[Mu]m^2)
CNT Detection
*USER INPUTTED VALUES (Gaussian Fit in Pixels)*
amplitude = 383.63;
xcenter = 43.259;
width = 1.4462;
CE = .051807;
ExpTime = 15;
Define 1D Gaussian Fit Values from Igor (in pixels, please
   )
Detection = (Integrate[
       A Exp[-((x - x0)/w)^2], {x, -\[Infinity], \[
          Infinity]}] /.
      A -> amplitude /. x0 -> xcenter /. w -> width) (
         count/row) ((1 row)/(
   0.161 \[Mu]m))*(2 photon)/count*1/CE*1/(ExpTime sec)
(15719.6 photon)/(sec \[Mu]m)
Scattering Length
L = Detection/Excitation *(1 meter)/(10^6 \[Mu]m)
```

1.40091*10^-10 meter

.2 Appendix II: Depolarization Matlab Codes

The depolarization effect is calculated in Matlab Codes:

```
% Calculating the electric field components (Ex, Ey and Ez
    ) with initial
% polarization along x, equations are following Richards
    and Wolf (1959)
% Electromagnetic diffraction in optical systems. II
    Structure of the image
% field in an aplanatic system. For calculation on
    nanowire, I set
% d=35*10^(9) for the diameter and integrate the
    overlapping area of the
% focus laser beam and nanowire. For graphene, I integrate
     the whole beam
% area intensity.
%
% Initial Condition of the experiment:
% Refractive index, n=1.467
% Wavelength,       785 nm
home
clear all
close all
tic
```

```
n=1.467;
NA=1.35;
alpha=asin(NA/n);
k=2*pi/(785*10^(-9));
% define the area of the nanowire (only for nanowire
    calculation)
d=35*10^(-9);
% Beginning point
%%for large scale or graphene calculation
% Inix=-2*10^(-6);
% Iniy=Inix;
% for small scale of nanowire calculation and wire along x
     direction
Inix=-1.5*10^(-6);
Iniy=-1.5*10^(-6);
% End Points
%for large scale or graphene calculation
Endx=-Inix;
Endy=Endx;
%% for small scale or nanowire calculation
% Endy=-Iniy;
% Endx=-Inix;
% Number of Steps for numerical calculation
xstep=500;
ystep=500;
% Step size
```

```
StepSizeX=(Endx-Inix)/(xstep-1);
StepSizeY=(Endy-Iniy)/(ystep-1);
% On the focus plane thp=pi/2
thp=pi/2;
% setup the vectors direction for each variable
xp=linspace(Inix, Endx, xstep);
yp=linspace(Iniy, Endy, ystep);
% Initialize the 2D functions
I0=zeros(max(size(xp)), max(size(yp)));
I1=zeros(size(I0));
I2=zeros(size(I0));
Ex=zeros(size(I0));
IEx=zeros(size(I0));
Ey=zeros(size(I0));
IEy=zeros(size(I0));
Ez=zeros(size(I0));
IEz=zeros(size(I0));
% generate a mesh in 2D
[Xp, Yp]=meshgrid(xp, yp);
% generating the I0, I1, I2, Ex, Ey, Ez and their
   intensity 2D-matrix
for n=1:1:max(size(xp)) % x
    for p=1:1:max(size(yp)) % y
        % calculate the corresponding rp and th
        [phip, rp]=cart2pol(xp(n),yp(p));
        % Numerically Integrate of B0 to give I0
```

```
            I0(n, p) = quadl(@(th)B0(th,k,rp,thp),0,alpha);
            % Numerically Integrate of B1 to give I1
            I1(n, p) = quadl(@(th)B1(th,k,rp,thp),0,alpha);
            % Numerically Integrate of B2 to give I2
            I2(n, p) = quadl(@(th)B2(th,k,rp,thp),0,alpha);
            % The electric field vector components
            Ex(n, p) = -1i*( I0(n,p) + I2(n,p) * cos( 2*(phip)
                ) );
            Ey(n, p) = -1i* I2(n,p) * sin(2* (phip) );
            Ez(n, p) = -2* I1(n,p) * cos( phip );
            % The corresponding Intensity of each field vector
                components
            IEx(n, p)= Ex(n,p).*(Ex(n,p))';
            IEy(n, p)= Ey(n,p).*(Ey(n,p))';
            IEz(n, p)= Ez(n,p).*(Ez(n,p))';
        end
    end
    % plot each components' modulus square
    % x component
    figure;
    [c,h]=contourf(Xp',Yp',IEx,100);
    set(h,'LineStyle','none');
    %clabel(c,h);
    colormap('gray')
    colorbar
    axis image
```

```
title('Intensity x component')
xlabel('x axis (m)')
ylabel('y axis (m)')
% y component
figure;
[c,h]=contourf(Xp',Yp',IEy,100);
set(h,'LineStyle','none');
%clabel(c,h);
colormap('gray')
colorbar
axis image
title('Intensity y component')
xlabel('x axis (m)')
ylabel('y axis (m)')
% z component
figure;
[c,h]=contourf(Xp',Yp',IEz,100);
set(h,'LineStyle','none');
%clabel(c,h);
colormap('gray')
colorbar
axis image
title('Intensity z component')
xlabel('x axis (m)')
ylabel('y axis (m)')
% Following is for graphene calculation
```

```
SumIEx=sum(sum(IEx*StepSizeX*StepSizeY,1),2);
SumIEy=sum(sum(IEy*StepSizeX*StepSizeY,1),2);
SumIEz=sum(sum(IEz*StepSizeX*StepSizeY,1),2);
AverageTime=toc/60
% follow http://sccn.ucsd.edu/eeglab/printfig.html to
    print out the figure
% print -depsc2 -adobecset -painter filename.eps
```

The three subfunctions are listed below. B0:

```
function y=B0(th,k,r,thp)
y=(cos(th)).^(1/2).*sin(th).*(1+cos(th)).*besselj(0,k.*r.*
    sin(th).*...
        sin(thp)).*cos(k.*r.*cos(th).*cos(thp))+...
        i*(cos(th)).^(1/2).*sin(th).*(1+cos(th)).*besselj(0,k
            .*r.*sin(th).*...
        sin(thp)).*sin(k.*r.*cos(th).*cos(thp));
```

B1:

```
function y=B1(th,k,r,thp)
y=(cos(th)).^(1/2).*((sin(th)).^2).*besselj(1,k.*r.*sin(th
    ).*...
        sin(thp)).*cos(k.*r.*cos(th).*cos(thp))+...
        i*(cos(th)).^(1/2).*((sin(th)).^2).*besselj(1,k.*r.*
            sin(th).*...
        sin(thp)).*sin(k.*r.*cos(th).*cos(thp));
```

B2:

```
function y=B2(th,k,r,thp)
y=(cos(th)).^(1/2).*sin(th).*(1-cos(th)).*besselj(2,k.*r.*
    sin(th).*...
       sin(thp)).*cos(k.*r.*cos(th).*cos(thp))+...
       i*(cos(th)).^(1/2).*sin(th).*(1-cos(th)).*besselj(2,k
          .*r.*sin(th).*...
       sin(thp)).*sin(k.*r.*cos(th).*cos(thp));
```

Also, the calculation for nanowire is also listed below.

```
close all
% Following is for Nanowire calculation
% sum over IEx, IEy and IEz.
% I set the stepsize about 50 times smaller than the
    diameter of the
% nanowire in this case.
d=60*10^(-9); %nm
% use index=find(abs(x)<=d)
index=find(abs(yp)<=d/2);
% this code extract x in (-inf, inf) and y in (-d/2, d/2)
ExtIExWire=IEx(:, min(index):max(index));
% Plot to check if the extractin makes sense
XpWire=Xp(min(index):max(index),:);
YpWire=Yp(min(index):max(index),:);
figure;
[c,h]=contourf(XpWire',YpWire',ExtIExWire,100);
set(h,'LineStyle','none');
```

```
colormap('gray')
colorbar
axis image
title('Intensity x component where the Nanowire Sees')
xlabel('x axis (m)')
ylabel('y axis (m)')
ExtIEyWire=IEy(:, min(index):max(index));
% Plot to check if the extractin makes sense
XpWire=Xp(min(index):max(index),:);
YpWire=Yp(min(index):max(index),:);
figure;
[c,h]=contourf(XpWire',YpWire',ExtIEyWire,100);
set(h,'LineStyle','none');
colormap('gray')
colorbar
axis image
title('Intensity y component where the Nanowire Sees')
xlabel('x axis (m)')
ylabel('y axis (m)')
ExtIEzWire=IEz(:, min(index):max(index));
% Plot to check if the extractin makes sense
XpWire=Xp(min(index):max(index),:);
YpWire=Yp(min(index):max(index),:);
figure;
[c,h]=contourf(XpWire',YpWire',ExtIEzWire,100);
set(h,'LineStyle','none');
```

```
colormap('gray')
colorbar
axis image
title('Intensity z component where the Nanowire Sees')
xlabel('x axis (m)')
ylabel('y axis (m)')
% Integrate over the nanowire range
SumIExWire=sum(sum(ExtIExWire*StepSizeX*StepSizeY,1),2);
SumIEyWire=sum(sum(ExtIEyWire*StepSizeX*StepSizeY,1),2);
SumIEzWire=sum(sum(ExtIEzWire*StepSizeX*StepSizeY,1),2);
% Integrate over the whole entire beam spot
SumIEx=sum(sum(IEx*StepSizeX*StepSizeY,1),2);
SumIEy=sum(sum(IEy*StepSizeX*StepSizeY,1),2);
SumIEz=sum(sum(IEz*StepSizeX*StepSizeY,1),2);
```

.3 Appendix III: Absorption Cross Section Mathematica Codes

The following is the Mathematica codes to calculate the absorption cross section of a SWNT from confocal spatial modulation experiment.

```
785 nm measurement
cor = -0.11579;
yw = 2.1119*6.45/60;
xw = 1.957*6.45/60 ;
G[x_, y_, A_] =
```

```
  A*Exp[-1/(2*(1 - cor^2))*(((x - 0)/xw)^2 + ((y - 0)/yw)
     ^2 -
       2*cor*x*y/(xw*yw))];
(*from the intensity measurement in the unit of W*)
Intensity = 11.6*10^(-3)*0.9^3;
sol = Solve[
  Integrate[G[x, y,
     A], {x, -\[Infinity], \[Infinity]}, {y, -\[Infinity],
         \[Infinity]}] ==
   Intensity, A]
{{A -> 0.0283698}}
A = 0.0283697560468069;
PhotoDetectorCurrentToPower = 0.505;
PhotoDetectorGain = 1.51 *(10^3);
Factors = PhotoDetectorCurrentToPower*PhotoDetectorGain
762.55
a = -0.00315;
b = 0.07083;
Amplitude = 0.086;
xmin = 1.05;
V2 = 0.48;
xmax = 2.02;
V1 = 0.44;
x = -(xmax - xmin)/2;
\[Delta] = -(V2 - V1)*10^(-3)/(b*Factors*
     Integrate[(G[x - Amplitude/2, y, A] -
```

```
        G[x + Amplitude/2, y,
         A]), {y, -\[Infinity], \[Infinity]}])*10^(3) (*
            unit=nm*)
0.687769
dNT = 1.9;
x = \[Delta]/dNT
0.361984
```

That is to say we have $\Delta=0.361984\times_{d,NT}$.

.4 Appendix E: Matlab Code for Modulation Amplitude

The following is Matlab code for modulation amplitude simulation:

```
clear all
% Assumption:
%1) the fitted beam is a Gaussian and the extract width is
     from a 2D
%gaussian
%2) normalization is from dividing the maximum
f = 2*10^(3);      %(*unit=KHz, linear frequency 2KHz*)
w = 2*pi*f;        %(*unit=Hz, angular frequency*)
cor = -0.11579;    %(*unitless, ellips shape of the 2D
    gaussian*)
xw = 1.957;        %(*unit=pix, width of the 2D gaussian in
    x direction*)
```

```
yw = 2.1119;        %(*unit=pix, width of the 2D gaussian in
    y direction*)
A = 3177;           %(*area under the gaussian*)
y=0;                %(*setting the y position to tbe zero for
     the gaussian*)
x=[];               %(*unit=pix, x position of the beam
    intensity, along x,
                    %the beam is gaussian*)
T=(1/32)*(1/f);     %(*Numerical Integration time to the for
    loop*)
T0=1000*T;          %(*Numerical Integration final time, set
    1000 loops*)
A0=[];              %(*Amplitude of the spacial modulation*)
N=[];               %(*beam intensity as a function of x and
    time (t)*)
t=[];               %(*temperal domain of the spacial
    modulation*)
J=[];               %(*sum of the integration over t*)
S=[];               %(*Normalized Integral, if A0 is zero, it
     should be a
                    %Gaussian*)
I=[];               %(*Index where the FWHM is happening*)
FW=[];              %(*Full width half max of the beam shape
    *)
Sigma=[];           %(*the x-width of the beam fitted in Igor
     2D gaussian*)
```

```
for A0=0:0.05:3;            % varying the amplitude
    x=-5:0.001:5;
    J=zeros(size(x));
    for t=0:T:T0;            % time integration of the
       gaussian
        N=A*exp(-1/(2*(1 - cor^2))*(((x-A0*sin(w*t))/xw)
           .^2));
        J=[J;N];
        J=sum(J);
    end
    S=J/max(J);
    I=find(S>0.5);
    FW=[FW,(x(max(I))-x(min(I)))/2];
end
A0=0:0.05:3;                % make sure the change this if
   the first for
                            %loop sis changing
Sigma=FW./(sqrt(2*(log(2))*(1-cor^2))); %this is the x-
   width of 2D
                                        %gaussian in Igor
plot(Sigma,A0,'o')
xlabel('Width (pixel)')
ylabel('Amplitude (pixel)')
Sigma=Sigma';
A0=A0';
save sigma.txt Sigma -ASCII
```

```
save amplitude.txt A0 -ASCII
```

.5 Appendix F: AFM Diameter Measurement

In the AFM SWNT diameter measurement, we use Asylum MFP 3D. After obtaining the SWNTs' locations corresponding to the Rayleighh image, we measure their diameters. The measurement protocol is follow:

1 Tune the tip at -5%, 1 V with 12dB.

2 Set setpoint at 800mV and lower the head to 70, the middle range.

3 Retune the tip, and scan the tube at 730 mV setpoint with 1 um by 1um 1 Hz scan.

.6 Appendix G: Relationship between Dielectric Function, Optical Conductivity, and Absorption Coefficients

Assuming an electric field, $E(z,\omega)$, is being applied onto a medium with dielectric coefficient ϵ_o and conductivity σ, we have the following relations:

1. current in time domain: $\mathbf{j}(z,t)$=Re[$\mathbf{j}(z,\omega)e^{-i\omega t}$]
2. current in frequency domain: $\mathbf{j}(z,\omega) = \sigma(\omega)E(z,\omega)$
3. displacement field: $D(z,\omega) = \epsilon_o(\omega)E(z,\omega)$

Then complex dielectric function ϵ is written as:

$$\epsilon(\omega) = \epsilon_o(\omega) + 4\pi i \frac{\sigma(\omega)}{\omega}.$$

As Ashcroft and Mermin point out, in optical frequency (AC) the distinction between ϵ_o and σ is blurred [67]. The complex refractive index is written as

$$N = \sqrt{\epsilon},$$

with

$$n = Re(N),$$

and

$$k = Im(N).$$

Assuming normal incident (Fresnel equations), the reflectivity R and absorption coefficient α can be expressed as:

$$R = \left|\frac{1-N}{1+N}\right|^2 = \frac{(1-n)^2 + k^2}{(1+n)^2 + k^2}, \tag{1}$$

$$\alpha = \frac{2\omega}{c}k. \tag{2}$$

The absorption cross section is obtained with the carrier density, as mentioned previously. From the Drude Theory of metals, the DC conductivity is defined as $\sigma_o = \frac{ne^2\tau}{m}$, with τ being the relaxation time and n being the number of electrons per unit volume, the real and imaginary parts of the conductivity are written:

$$Re(\sigma) = \frac{\sigma_o}{1 + \omega^2\tau^2}$$

and

$$Im(\sigma) = \frac{\sigma_o \omega\tau}{1 + \omega^2\tau^2}.$$

The final dielectric function is written as:

$$\epsilon = (\epsilon_o - \frac{4\pi\sigma_o\tau}{1 + \omega^2\tau^2}) + \frac{4\pi\sigma_o i}{\omega(1 + \omega^2\tau^2)}.$$

BIBLIOGRAPHY

[1] J. M. Ziman. *Principles of the Theory of Solids*. Cambridge University Press, 1972.

[2] K. I. Bolotin, F. Ghahari, Michael D. Shulman, H. L. Stormer, and P. Kim. *Nature*, 462, 2009.

[3] R. Laughlin. *Phys. Rev. B*, 23, 1981.

[4] A. Tzalenchuk, S. Lara-Avila, A. Kalaboukhov, S. Paolillo, M. Syvjrvi, R. Yakimova, O. Kazakova, T. J. B. M. Janssen, V. Fal'ko, and S. Kubatkin. *Nat. Nanotechnol.*, 5, 2010.

[5] K. S. Novoselov, Z. Jiang, Y. Zhang, S. V. Morozov, H. L. Stormer, U. Zeitler, J. C. Maan, G. S. Boebinger, P. Kim, and A. K. Geim. *Science*, 315, 2007.

[6] D.C. Tsui, H.L. Stormer, and A.C. Gossard. *Phys. Rev. Lett.*, 48, 1982.

[7] H.L. Stormer. *Rev. Mod. Phys.*, 71, 1982.

[8] M. Bockrath, D. H. Cobden, Jia Lu, A. G. Rinzler, R. E. Smalley, L. Balents, and P. L. McEuen. *Nature*, 397, 1999.

[9] J. M. Luttinger. *J. Math. Phys.*, 4, 1963.

[10] H. W. Kroto, J. R. Heath, S. C. O'Brien, R. F. Curl, and R. E. Smalley. *Nature*, 318, 1985.

[11] A. Jorio, G. Dresselhaus, and M. S. Dresselhaus. *Carbon Nanotubes: Advanced Topics in the Synthesis, Structure, Properties and Applications*. Springer-Verlag, Berlin, Heidelberg, 2008.

[12] S. Iijima. Synthesis of carbon nanotubes. *Nature*, 354:56, 1991.

[13] S. Reich, C. Thomsen, and J. Maultzsch. *Carbon Nanotubes: Basic Concepts and Physical Properties*. Wiley VCH Verlag GmbH & Co. kGaA, Weinheim, 2004.

[14] A. Hartschuh, H. N. Pedrosa, J. Peterson, L. Huang, P. Anger, H. Qian, A. J. Meixner, M. Steiner, L. Novotny, and T. D. Krauss. *Single Carbon Nanotube Optical Spectroscopy*. Wiley VCH Verlag GmbH & Co. kGaA, Weinheim, 1999.

[15] M. S. Dresselhaus, G. Dresselhaus, J. C. Charlier, and E. Hernandez. *Phil. Trans. R. Soc. Lond. A*, 362, 2004.

[16] L. X. Zheng, M. J. O'Connell, S. K. Doorn, X. Z. Liao, Y. H. Zhao, E. A. Akhadov, M. A. Hoffbauer, B. J. Roop, Q. X. Jia, R. C. Dye, D. E. Peterson, S. M. Huang, J. Liu, and Y. T. Zhu. *Nat. Mater.*, 3, 2004.

[17] P. Avouris, J. Chen, M. Freitag, V. Perebeinos, and J.C. Tsang. *Phys. Stat. Sol. B*, 243, 2004.

[18] P. Avouris. *Acc. Chem. Res.*, 35, 2002.

[19] M. Bockrath, D. H. Cobden, P. L. McEuen, N. G. Chopra, A. Zettl, A. Thess, and R. E. Smalley. *Science*, 275, 1997.

[20] D. A. Muller. *Nature Materials*, 4, 2005.

[21] R. Weissleder. *Nat Biotechnol*, 19, 2001.

[22] J. Frangioni. *Curr Opin Chem Biol*, 7, 2009.

[23] Z. Liu, S. Tabakman, K. Welsher, and H. Dai. *Nano Res*, 2:85, 2009.

[24] A. M. Smith, M. C. Mancini, and S. Nie. *Nat Biotechnol*, 4, 2009.

[25] O. E. Semonin, J. M. Luther, S. Choi, H. Chen, J. Gao, A. J. Nozik, and M. C. Beard. *Science*, 334:1530, 2011.

[26] N. M. Gabor, Z. Zhong, K. Bosnick, J. Park, and Paul L. McEuen. *Science*, 325:1367, 2009.

[27] G. Binnig and H. Rohrer. *IBM Journal of Research and Development*, 30:4, 1986.

[28] G.K. Binnig, C.F. Quate, and Ch. Gerber. *Phys. Rev. Lett.*, 56:930, 1986.

[29] K. M. Lang, D. A. Hite, R. W. Simmonds, R. McDermott, D. P. Pappas, and John M. Martinis. *Review of Scientific Instruments*, 75:2726, 2004.

[30] E. Ruska. *Nobel Lectures, Physics 1981-1990*, 1986.

[31] M. Knoll and J. Kgler. *Nature*, 184:1823, 1959.

[32] J. W. G. Wildo, L. C. Venema, A. G. Rinzler, R. E. Smalley, and C. Dekker. *Nature*, 391:59, 1998.

[33] T. W. Odom, J. Huang, P. Kim, and C. M. Lieber. *Nature*, 391:62, 1998.

[34] C. M. Lieber. *Solid State Comm.*, 107, 1998.

[35] C. M. Lieber J. T. Hu, T. W. Odom. *Accts. Chem. Res.*, 32, 1999.

[36] C. L. Kane and E. J. Mele. *Phys. Rev. Lett.*, 78, 1997.

[37] V. H. Crespi, M. L. Cohen, and A. Rubio. *Phys. Rev. Lett.*, 79, 1997.

[38] J. M. Zuo, I. Vartanyants, M. Gao, R. Zhang, and L. A. Nagahara. *Science*, 300:1419, 2003.

[39] C. Fantini, A. Jorio, M. Souza, M. S. Strano, M. S. Dresselhaus, and M. A. Pimenta. *Phys. Rev. Lett.*, 93, 2004.

[40] M. S. Dresselhaus, G. Dresselhaus, R. Saito, and A. Jorio. *Physics Reports*, 409, 2005.

[41] F. Wang, G Dukovic, L. Brus, and T. Heinz. *Science*, 308:838, 2005.

[42] M. Y. Sfeir, T. Beetz, F. Wang, L. Huang, X. M. H. Huang, M. Huang, J. Hone, S. O'Brien, J. A. Misewich, T. F. Heinz, L. Wu, Y. Zhu, and L. E. Brus. *Science*, 312:554, 2006.

[43] M.Y. Sfeir, F. Wang, L. Huang, C. Chuang, J. Hone, S.P. O'Brien andT. F. Heinz, and L.E. Brus. *Science*, 306:1540, 2004.

[44] S M. Bachilo, M. S. Strano, C. Kittrell, R. H. Hauge, R. E. Smalley, and R. B. Weisman. *Science*, 298:2361, 2002.

[45] M. J. O'Connell, S. M. Bachilo, C. B. Huffman, V. C. Moore, M. S. Strano, E. H. Haroz, K. L. Rialon, P. J. Boul, W. H. Noon, C. Kittrell, J. Ma, R. H. Hauge, R. B. Weisman, and R. E. Smalley. *Science*, 297:593, 2002.

[46] S. Berciaud, L. Cognet, P. Poulin, R. B. Weisman, and B. Lounis. *Nano Lett.*, 7:1203, 2007.

[47] A. Kukovecz, Ch. Kramberger, V. Georgakilas, M. Prato, and H. Kuzmany. *Eur. Phys. J. B*, 28:223, 2002.

[48] A. Jorio, R. Saito, J. H. Hafner, C. M. Lieber, M. Hunter, T. McClure, G. Dresselhaus, and M. S. Dresselhaus. *M. Phys. Rev. Lett.*, 86:1118, 2001.

[49] S. Berciaud, C. Voisin, H. Yan, B. Chandra, R. Caldwell, Y. Shan, L. E. Brus, J. Hone, and Tony F. Heinz. *Phys. Rev. B*, 81, 2010.

[50] S. Berciaud, L. Cognet, and B. Lounis. *Phys. Rev. Lett.*, 101, 2010.

[51] R. Saito and H. Kataura. Optical properties and raman spectroscopy of carbon nanotubes. In M. S. Dresselhaus, G. Dresselhaus, and P. Avouris, editors, *Carbon Nanotubes*, volume 80 of *Topics in Applied Physics*, page 213. Springer Berlin / Heidelberg, New York, 2001.

[52] M. Fox. Optical properties of solids. 2001.

[53] K. S. Novoselov, A. K. Geim, S. V. Morozov, D. Jiang, Y. Zhang, S. V. Dubonos, I. V. Grigorieva, and A. A. Firsov. *Science*, 306:666, 2004.

[54] X. Li, W Cai, J. An, S. Kim, J. Nah, D. Yang, R. Piner, A. Velamakanni, I. Jung, E. Tutuc, S. K. Banerjee, L. Colombo, and R. S. Ruoff. *Science*, 324:1312, 2009.

[55] T. A. Edison. Us patent 470, 925, March 1892.

[56] P. Schutzenberger and L. Schutzenberger. *Compt. Rend*, 111, 1890.

[57] C. H. Pelabon. *Compt. Rend*, 137, 1905.

[58] M. Endo. PhD thesis, Nagoya University, Japan, 1978.

[59] M. Endo. PhD thesis, University of Orleans, Orleans, France, 1975.

[60] D. S. Bethune, C. H. Kiang, M. S. de Vries, G. Gorman, R. Savoy, J. Vazques, and R. Beyers. *Nature*, 363, 1993.

[61] A. Thess, R. Lee, P. Nikolaev, J. Robert, C. Xu, Y. H. Lee, S. G. Kim, A. G. Rinzler, D. T. Cobert, G. E. Scueria, D. Tomanek, J. E. Fischer, and R. E. Smalley. *Science*, 273, 1996.

[62] T. W. Ebbesen and P. M. Ajayan. *Nature*, 358, 1992.

[63] A. Oberlin, M. Endo, and T. Koyama. *Cryst. Growth*, 32, 1976.

[64] A. Jorio, M. A. Pimenta, A. G. Souza Filho, R. Saito, G. Dresselhaus, and M. S. Dresselhaus. *New J. Phys.*, 5, 2003.

[65] U. Fano. *Phys. Rev.*, 124, 1961.

[66] J. J. Sakurai. Modern quantum mechanics. 1993.

[67] N. W. Ashcroft and N. D. Mermin. Solid state physics. 1976.

[68] R. C. Hilborn. *Am. J. Phys.*, 50, 1982.

[69] K. F. Mak, J. Shan, and T. F. Heinz. *Phys. Rev. Lett.*, 106, 2011.

[70] J. I. Pankove. Processes in semiconductors. 1971.

[71] R Saito, G. Dresselhaus, and M. S. Dresselhaus. Physical properties of carbon nanotubes. 1998.

[72] M. Damnjanovie, I. Milosevic, T. Vukovic, and R. Sredanovic. *J. Phys. A*, 32:4097, 1999.

[73] M. Damnjanovie. *Phys. Lett. A*, 94:337, 1983.

[74] M. Damnjanovie, I. Boiovic, and N. Bozovic. *J. Phys. A: Math. Gen*, 17:747, 1984.

[75] M. Damnjanovic, T. Vukovic, and I. Milokvic. *J. Phys. A: Math. Gen*, 33:6561, 2000.

[76] S. Reich, C. Thomsen, and J. Maultzsch. Carbon nanotubes. 2004.

[77] A. Gruneis, R. Saito, J. Jiang, Ge.G. Samsonidze, M.A. Pimenta, A. Jorio, A.G. Souza Filho, G. Dresselhaus, and M.S. Dresselhaus. Chemical physics lett. 387:301, 2004.

[78] M. F. Islam, D. E. Milkie, C. L. Kane, A. G. Yodh, and J. M. Kikkawa. *Phys. Rev. Lett.*, 93:37404, 2004.

[79] M. S. Dresselhaus, G. Dresselhaus, and P.C. Eklund. *Science of Fullerenes and Carbon Nanotubes*. Academic, San Diego, 2003.

[80] M. S. Dresselhaus, G. Dresselhaus, R. Saito, and A. Jorio. *Annual Review of Physical Chemistry*, 58:719, 2007.

[81] C.L. Kane and E.J. Mele. *Phys. Rev. Lett.*, 90, 2003.

[82] C.L. Kane and E.J. Mele. *Phys. Rev. Lett.*, 93, 2004.

[83] E.J. Mele and C.L. Kane. *Solid State Communication*, 135, 2005.

[84] J. Lefebvre, Y. Homma, and P. Finnie. *Phys. Rev. Lett.*, 90, 2003.

[85] A. Hagen and T. Hertel. *Nano Lett.*, 3, 2003.

[86] N. Hamada, S. Sawada, and A. Oshiyama. *Phys. Rev. Lett.*, 68, 1992.

[87] J.W. Mintmire, B. I. Dunlap, and C.T.White. *Phys. Rev. Lett.*, 68, 1992.

[88] R. Saito, M. Fujita, G. Dresselhaus, and M. S. Dresselhaus. *Appl. Phys. Lett.*, 60, 1992.

[89] R. Saito, G. Dresselhaus, and M.S. Dresselhaus. *Phys. Rev. B*, 61, 2000.

[90] T. Ando. *J. Phys. Soc. Jpn*, 66:1066, 1997.

[91] J. Maultzsch, R. Pomraenke, S. Reich, E. Chang, D. Prezzi, A. Ruini, E. Molinari, M. S. Strano, C. Thomsen, and C. Lienau. *Phys. Rev. B*, 72, 2005.

[92] R. W. Boyd. *Nanolinear Optics.* Academic Press, New York, 2003.

[93] G. D. Mahan. *Phys. Rev.*, 170, 1968.

[94] H. Zhao and S. Mazumdar. *Phys. Rev. Lett.*, 93, 2004.

[95] J. M. Kinder. PhD thesis, University of Pennsylvania, Philadelphia, US, 2008.

[96] J. Xiao, S. Dunham, P. Liu, Y. Zhang, C. Kocabas, L. Moh, Y. Huang, K. Hwang, C. Lu, W. Huang, and J. A. Rogers. *Nano Lett.*, 9:4311, 2009.

[97] C. Kocabas, S. J. Kang, T. Ozel, M. Shim, and J. Rogers. *J. Phys. Chem. C*, 111:17879, 2007.

[98] H. J. W. Strutt. *Philosophical Magazine*, 41:447, 1871.

[99] M. Quinten. *Optical Properties of Nanoparticle Systems: Mie and Beyond*. Wiley, 2011.

[100] D.Y. Joh, L. H. Herman, S. Ju, J. Kinder, M. A. Segal, J. N. Johnson, G. K. L. Chan, and J. Park. *Nano Lett.*, 11:1, 2011.

[101] M. S. Strano, S. K. Doorn, E. H. Haroz, C. Kittrell, R. H. Hauge, and R. E. Smalley. *Nano Lett.*, 3:1091, 2003.

[102] B. Chandra, J. Bhattacharjee, M. Purewal, Y. Son, Y. Wu, M. Huang, H. Yan, T. F. Heinz, P. Kim, J. B. Neaton, and J. Hone. *Nano Lett.*, 9:1544, 2009.

[103] G. Y. Slepyan, M. V. Shuba, S. A. Maksimenko, and A. Lakhtakia. *Phys. Rev. B*, 73, 2006.

[104] G. Y. Slepyan, S. A. Maksimenko, A. Lakhtakia, O. Yevtushenko, and A. V. Gusakov. *Phys. Rev. B*, 60, 1999.

[105] P. J. Burke, S. D. Li, and Z. Yu. *IEEE Trans. Nanotechnol.*, 5, 2006.

[106] J. Hao and G. W. Hanson. *IEEE Trans. Nanotechnol.*, 55, 2006.

[107] K. Kempa et al. *Adv. Mater.*, 19, 2007.

[108] E. Cubukcu et al. *Proc. Natl Acad. Sci. USA*, 106, 2009.

[109] Y. Wang et al. *Appl. Phys. Lett.*, 85, 2004.

[110] G. W. Hanson. *IEEE Trans. Nanotechnol.*, 53, 2005.

[111] T.A. Abbott and D.J. Griffiths. *Am. J. Phys.*, 53:1203, 1985.

[112] V. Perebeinos, J. Tersoff, and P. Avouris. *Phys. Rev. Lett.*, 92, 2004.

[113] C. D. Spataru, S. Ismail-Beigi, L. X. Benedict, and S. G. Louie. *Appl. Phys. A*, 78, 2004.

[114] J.M. Kinder, G.K.L. Chan, and J. Park. *Phys. Rev. B*, 84, 2011.

[115] S. Berciaud, L. Cognet, and B. Lounis. *Phys. Rev. Lett.*, 101:2008, 2005.

[116] J. D. Jackson. *Classical Electrodynamics*. Wiley, third edition, 1998.

[117] G. D. Scholes. *Annu. Rev. Phys. Chem.*, 54:57, 2003.

[118] P. H. Tan, A. G. Rozhin, T. Hasan, P. Hu, V. Scardaci, W. I. Milne, and A. C. Ferrari. *Phys. Rev. Lett.*, 99, 2007.

[119] S. Ju, W. P. Kopcha, and F. Papadimitrakopoulos. *Science*, 323:1319, 2009.

[120] F. Wang, M. Y. Sfeir, L. Huang, X. M. H. Huang, Y. Wu, J. Kim, J. Hone, S. OBrien, L. E. Brus, and T. F. Heinz. *Phys. Rev. Lett.*, 96, 2006.

[121] M. D. Kelzenberg, D. B. Turner-Evans, B. M. Kayes, M. A. Filler, M. C. Putnam, N. S. Lewis, and H. A. Atwater. *Nano Lett.*, 8:710, 2008.

[122] Y. Ahn, J. Dunning, and J. Park. *Nano Lett.*, 5:1367, 2005.

[123] N. G. Kalugin, L. Jing, W. Bao, L. Wickey, C. D. Barga, M. Ovezmyradov, E. A. Shaner, and C. N. Lau. *Appl. Phys. Lett.*, 99, 2011.

[124] M. H. Huang, S. Mao, H. Feick, H. Q. Yan, Y. Y. Wu, H. Kind, E. Weber, R. Russo, and P. D. Yang. *Science*, 292:1897, 2001.

[125] C. J. Kim, H. S. Lee, Y. J. Cho, K. Kang, and M. H. Jo. *Nano Lett.*, 10:2043, 2010.

[126] K. Okamoto, I. Niki, A. Shvartser, Y. Narukawa, T. Mukai, and A. Scherer. *Nat. Mater.*, 3:601, 2004.

[127] P. Bharadwaj, B. Deutsch, and L. Novotny. *Adv. Opt. Photon.*, 1:438, 2009.

[128] L. Vivien, P. Lancon, D. Riehl, F. Hache, and E. Anglaret. *Carbon*, 40:1789, 2002.

[129] D. Y. Joh, J. Kinder, L. H. Herman, S. Ju, M. A. Segal, J. N. Johnson, G. K. L. Chan, and J Park. *Nat. Nanotechnol.*, 6:51, 2011.

[130] L. H. Herman, C. J. Kim, Z Wang, M. H. Jo, and J. Park. *Applied Physics Letters*, 101, 2012.

[131] B. Richards and E. Wolf. *Proc. R. Soc. London, Ser. A*, 253:358, 1959.

[132] B. Sick, B. Hecht, U. P. Wild, and L. Novotny. *J Microsc (Oxf)*, 202:365, 2001.

[133] K. Bahlmann and S. W. Hell. *Appl. Phys. Lett.*, 77:612, 2000.

[134] J. W. Suk, A. Kitt, C. W. Magnuson, Y. Hao, S. Ahmed, J. An, A. K. Swan, B. B. Goldberg, and R. S. Ruoff. *ACS Nano*, 5:6916, 2011.

[135] C. J. Kim, H. S. Lee, Y. J. Cho, J. E. Yang, R. R. Lee, J. K. Lee, and M. H. Jo. *Adv. Mater.*, 23:1025, 2011.

[136] J. M. Dawlaty, S. Shivaraman, J. Strait, P. George, M. Chandrashekhar, F. Rana, M. G. Spencer, D. Veksler, and Y. Q. Chen. *Appl. Phys. Lett.*, 93:3, 2008.

[137] Q. L. Bao, H. Zhang, Y. Wang, Z. H. Ni, Y. L. Yan, Z. X. Shen, K. P. Loh, and D. Y. Tang. *Adv. Funct. Mater.*, 19:3077, 2009.

[138] C. F. Bohren and D. R. Huffman. *Absorption and Scattering of Light by Small Particles*. Wiley, 2004.

[139] L. Y. Cao, J. S. White, J. S. Park, J. A. Schuller, B. M. Clemens, and M. L. Brongersma. *Nat. Mater.*, 8:643, 2009.

[140] J. H. Jung, H. S. Yoon, Y. L. Kim, M. S. Song, Y. Kim, Z. G. Chen, J. Zou, D. Y. Choi, J. H. Kang, H. J. Joyce, Q. A. Gao, H. H. Tan, and C. Jagadish. *Nanotechnology*, 21:9, 2010.

[141] M. Celebrano, P. Kukura, A. Renn, and V. Sandoghdar. *Nature Photonics*, 5:95, 2011.

[142] D. Christofilos, J.-C. Blancon, J. Arvanitidis, A. San Miguel, A. Ayari, N. Del Fatti, and F. Valle. *J. Phys. Chem. Lett.*, 3:1176, 2012.

[143] F. Wang, D. J. Cho, B. Kessler, J. Deslippe, P. J. Schuck, S. G. Louie, A. Zettl, T. F. Heinz, and Y. R. Shen. *PRL*, 99, 2007.